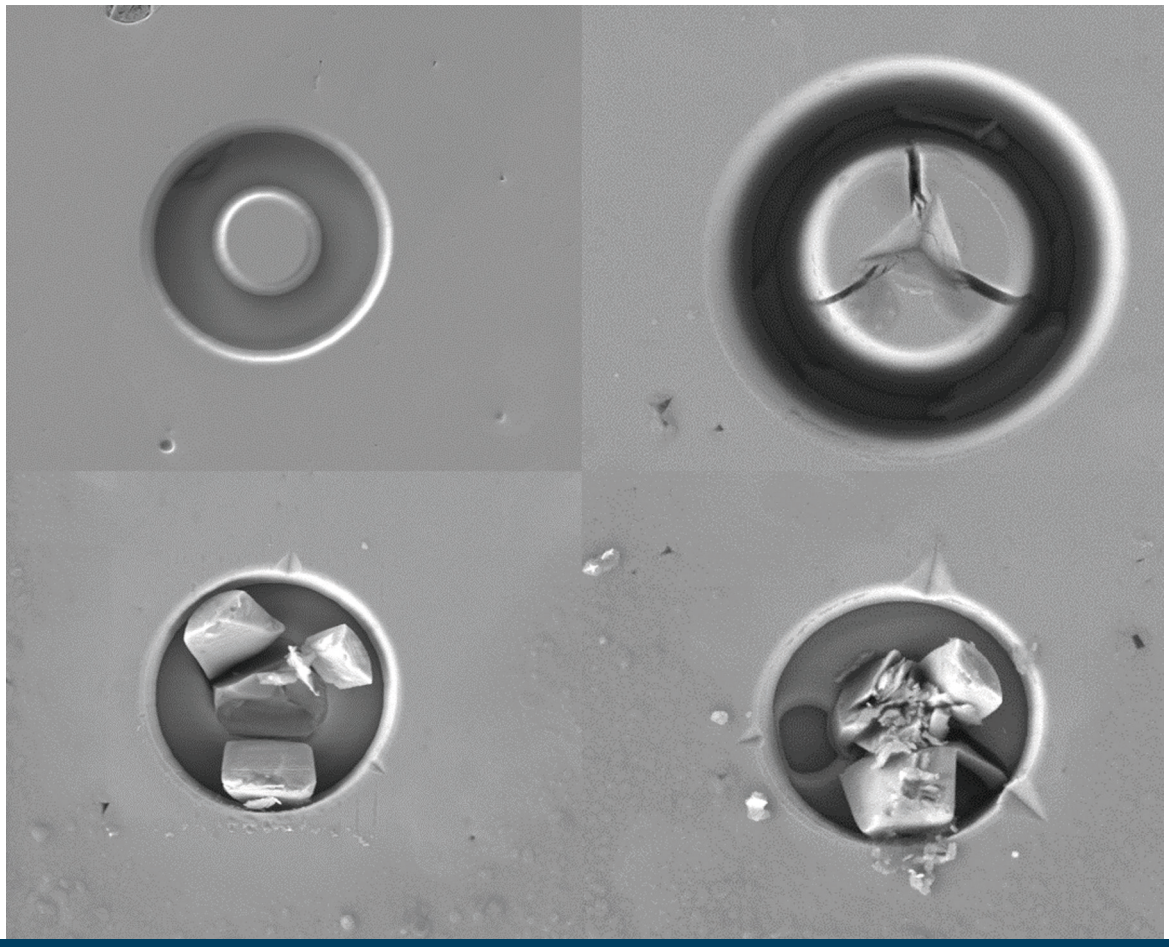

Micromechanical Characterization of Ceramic Solid Electrolytes for Electrochemical Storage Devices

Juliane Franciele Nonemacher

Energie & Umwelt / Energy & Environment
Band / Volume 490
ISBN 978-3-95806-461-4

Mitglied der Helmholtz-Gemeinschaft

JÜLICH
Forschungszentrum

Schriften des Forschungszentrums Jülich
Reihe Energie & Umwelt / Energy & Environment Band / Volume 490

Forschungszentrum Jülich GmbH
Institut für Energie- und Klimaforschung
Werkstoffstruktur und -eigenschaften (IEK-2)

Micromechanical Characterization of Ceramic Solid Electrolytes for Electrochemical Storage Devices

Juliane Franciele Nonemacher

Schriften des Forschungszentrums Jülich
Reihe Energie & Umwelt / Energy & Environment Band / Volume 490

ISSN 1866-1793 ISBN 978-3-95806-461-4

Bibliografische Information der Deutschen Nationalbibliothek.
Die Deutsche Nationalbibliothek verzeichnet diese Publikation in der Deutschen Nationalbibliografie; detaillierte Bibliografische Daten sind im Internet über http://dnb.d-nb.de abrufbar.

Herausgeber und Vertrieb:	Forschungszentrum Jülich GmbH Zentralbibliothek, Verlag 52425 Jülich Tel.: +49 2461 61-5368 Fax: +49 2461 61-6103 zb-publikation@fz-juelich.de www.fz-juelich.de/zb
Umschlaggestaltung:	Grafische Medien, Forschungszentrum Jülich GmbH
Druck:	Grafische Medien, Forschungszentrum Jülich GmbH
Copyright:	Forschungszentrum Jülich 2020

Schriften des Forschungszentrums Jülich
Reihe Energie & Umwelt / Energy & Environment, Band / Volume 490

D 82 (Diss. RWTH Aachen University, 2019)

ISSN 1866-1793
ISBN 978-3-95806-461-4

Vollständig frei verfügbar über das Publikationsportal des Forschungszentrums Jülich (JuSER) unter www.fz-juelich.de/zb/openaccess.

This is an Open Access publication distributed under the terms of the Creative Commons Attribution License 4.0, which permits unrestricted use, distribution, and reproduction in any medium, provided the original work is properly cited.

Abstract

The use of solid electrolytes in solid-state batteries offers safer operation, higher performance in terms of energy storage, as well as high thermal and chemical stability. Furthermore, solid electrolytes are expected to possess enhanced ionic conductivity and mechanical stability that warrants a safer separation of cathode and anode, and hence, potentially permits them to withstand long-term cycling operation. However, mechanical boundary conditions and operation as electrolyte under cyclic loading might still induce micro-cracks, dendrite growth, structural and mechanical failure that ultimately will terminate the battery life. Therefore, the mechanical reliability of solid electrolytes is important to warrant long-term reliability of solid state batteries. In this thesis, aiming at a characterization of reliability and life-time relevant aspects, the mechanical properties of $Li_7La_3Zr_2O_{12}$ for the application as solid electrolyte are studied on a micro-scale and the correlation to the materials microstructural characteristics. Mechanical investigations are based on indentation testing, yielding elastic modulus hardness and fracture toughness, where the use of an advanced micro-pillar testing methodology permitted to gain insight into the fracture properties of individual grains. The results emphasis the importance of the materials microstructure as well as the used testing loads, which illustrate effects related to the local apparent plasticity, and for larger loads localized pores. Overall, combining nano- and micro-indentation testing yields elastic modulus, hardness and fracture toughness with respect to materials intrinsic properties and global properties, where the use of standard Vickers indentation and the novel micro-pillar splitting test permit assessment of the fracture toughness of individual grains and effects related to grain boundaries and pores.

Kurzfassung

Die Verwendung von Festkörperbatterie erlaubt einen sicheren Betrieb, besseres Betriebsverhalten hinsichtlich Energiespeicherung, als auch höhere thermische und chemische Stabilität. Außerdem kann für Festkörperbatterie-Elektrolyte eine bessere ionische Leitfähigkeit und mechanische Stabilität erwartet werden, welches eine sichere Abtrennung von Kathode und Anode gewährleistet und damit potenziell einen langzeitzyklischen Betrieb erlaubt. Jedoch können mechanische Randbedingungen und Betrieb des Elektrolyten unter zyklischer Belastung zu Mikrorissen, Dendrit-Wachstum, sowie strukturellem und mechanischem Versagen führen, welches ultimativ die Batterie-Lebensdauer begrenzt. Die mechanische Zuverlässigkeit des Festkörperelektrolyten ist daher für die Langzeit-Zuverlässigkeit der Festkörperbatterie wichtig. Die vorliegende Promotionsschrift präsentiert eine Studie der mechanischen Eigenschaften von $Li_7La_3Zr_2O_{12}$ für die Anwendung als Festkörperelektrolyt auf Mikroskala und eine Korrelation mit den mikrostrukturellen Charakteristika des Materials. Mechanische Untersuchungen basieren auf dem Härteeindruckstest, wobei eine fortschrittliche Mikrosäulen-Test-Methodologie einen Einblick in die Risszähigkeit einzelner Körner erlaubt. Die Resultate betonen die Wichtigkeit sowohl der Material-Mikrostruktur als auch der Test-Belastung, welches Effekte der lokal offensichtlichen Plastizität veranschaulicht, für höhere Belastungen den lokalisierter Poren. Insgesamt ergibt die Kombination von Nano- und Mikro-Härteeindringtests elastischen Modul, Härte und Risszähigkeit hinsichtlich der intrinsischen Materialeigenschaften und der globalen Eigenschaften, wobei die Verwendung von Standard Vickers-Härteeindringtests und des fortschrittlichen Mikrosäulen Spalttests eine Abschätzung von Risszähigkeit von Korn und Effekten im Zusammenhang mit Korngrenzen und Poren erlaubt.

Contents

Abstract i

Kurzfassung iii

Contents v

List of Tables ix

List of Figures xi

1. Introduction 1

2. Literature Review 3

2.1. Batteries 3

2.1.1. Conventional and solid-state batteries 3

2.1.2. Solid-state electrolytes 7

2.1.3. Properties of solid-state electrolytes (physical, chemical and mechanical properties) 8

2.2. Mechanical characteristics 14

2.2.1. Elastic behavior (elastic modulus) 14

2.2.2. Plastic behavior (hardness) 16

2.2.3. Fracture properties (fracture toughness) 16

2.2.3.1. Vickers indentation fracture 17

2.2.3.2. Micro-pillar Indentation Splitting test 19

2.2.4. Mechanical considerations of solid-state electrolytes 21

2.2.4.1. Dendrite suppression 23

2.2.4.2. Mechanical properties of $Li_7La_3Zr_3O_{12}$ (LLZO) 26

3. Experimental 31

3.1. Materials synthesis 31

3.1.1. Cold pressed 31

3.1.2. Hot pressed 33
3.2. Microstructural characterization 34
3.2.1. X-Ray diffractometry 34
3.2.2. Inductively coupled plasma optical emission spectrometry 35
3.2.3. Electrochemical impedance spectroscopy 35
3.2.4. Metallographic preparation 36
3.2.5. Scanning electron microscope and electron backscatter diffraction 36
3.2.6. Focused ion beam 36
3.3. Mechanical characterization 37
3.3.1. Depth-sensitive indentation test 37
3.3.2. Indenation fracture toughness 38
3.3.3. Micro-pillar splitting test 39
4. Results and discussion 44
4.1. Substitution effect of $Li_7La_3Zr_2O_{12}$ 45
4.1.1. Conductivity, phase composition and microstructure 45
4.1.2. Mechanical testing results 50
4.1.3. Conclusions and outlook 55
4.1.4. Porosity effect 57
4.1.5. Moisture associated degradation 78
4.2. Fracture toughness Al-substituted $Li_7La_3Zr_2O_{12}$ (Al:LLZO) by utilizing micro-pillar indentation splitting test 81
4.2.1. Conductivity, phase composition and microstructure 81
4.2.2. Mechanical testing results 83
4.2.3. Conclusions and outlook 92
4.3. Hot pressed LLZO 94

4.3.1. Conductivity, phase composition and microstructure 94
4.3.2. Mechanical testing results 97
4.3.2.1. Vickers indentation toughness 99
4.3.2.2. Micro-pillar splitting test 102
5. Conclusions and Outlook 110
6. References 113
Appendix 125
Publications & Conferences 128
Acknowledgements 130

List of Tables

Table 2.1- Mechanical properties of ceramic solid electrolyte materials (adapted from [100])... 12
Table 2.2- Equations to calculate K_{IC} values from indentation tests. 18
Table 2.3 - Mechanical properties of garnet-structured LLZO solid electrolytes. 27
Table 3.1- Substitution, sintering conditions and relative density of investigated materials. 32
Table 3.2- List of samples and associated features. 32
Table 3.3 - Description of hot pressed specimens. 34
Table 3.4- Summary of tested samples by micro-pillar splitting test. 40
Table 4.1- Substitution, sintering conditions, relative density, total Li-ion conductivity and composition 46
Table 4.2- Lattice parameters and portion of tetragonal phase obtained from Rietveld refinement. 49
Table 4.3- Effect of Al and Ta doping on porosity, phase content, elastic modulus and hardness. 51
Table 4.4- Microstructure, grain size and porosity of Al-substituted LLZO sintered for different dwell times. 57
Table 4.5 – Mechanical properties of Al-substituted LLZ material, extracted from CMC mode at the low load range (materials properties) and high load range (effective properties). 61
Table 4.6- Elastic modulus, hardness and maximum penetration depth of 20Al:LLZO obtained for Vickers indentation at 1 N. 62
Table 4.7- Summary of average crack length, *l*/*a* ratio and K_{IC} of 20Al-subsituted LLZO..... 64
Table 4.8 –Microstructure, grain size and porosity of 40% Ta-substituted LLZO sintered for different dwell times. 66
Table 4.9- Elastic modulus and hardness of LLZ material, extracted from the low load range of CMC. 70
Table 4.10- Elastic modulus, hardness and penetration depth of 40Ta:LLZ obtained for Vickers indentation at 1 N. 72
Table 4.11- Summary of 40Ta:LLZ specimens, average crack length, *l*/*a* ratio and K_{IC}. 75
Table 4.12- Summary of composition, structure, relative density and conductivity. 82

Table 4.13- Comparison of mechanical properties, hardness, Young's modulus and fracture toughness..... 84
Table 4.14 - Summary of micro-pillar indentation splitting test results. 91
Table 4.15 – Summary of specimen, density, grain size and conductivity..... 95
Table 4.16 - Mechanical properties of HP-Al:LLZO at 500 nm depth. 98
Table 4.17- Vickers indentation toughness results for HP-Al:LLZO specimens. 101
Table 4.18- Summary of micro-pillar indentation splitting test results for sample HP-Al:LLZO-LG, $\beta \approx 0.27$. 104
Table 4.19- Summary of micro-pillar indentation splitting test results for sample HP-Al:LLZO-SG, $\beta \approx 0.27$. 107

List of Figures

Figure 2.1- Schematic illustration of traditional lithium-ion battery [9]. 4
Figure 2.2- Schematic representation of a lithium based solid-state battery [8]. 6
Figure 2.3- Schematic atomic structure of a LLZO cell a) Al-doped and b) Ta-doped [13]..... 11
Figure 2.4- Schematic representation of a) main parameters describing the indentation process b) typical indentation load–displacement curve, where P_{max} is the max. indentation load, h_{max} the indenter displacement at peak load, h_f the final depth of the contact impression after unloading and S the initial unloading stiffness [105]. 15
Figure 2.5- Schematic of Palmqvist cracks and median-radial cracks [114]..... 17
Figure 2.6-SEM micrographs of pillar on ceramic samples and the representative load-displacement curves: a) and b) silicon single crystal; c) and d) CrN (adapted from [127])..... 19
Figure 2.7- Dendrite failure reported in different SSE materials a) Ga-doped LLZO; b) Al-doped LLZO; c) LiPON-Li interface [135]. 23
Figure 2.8- Schematic illustration of Li penetration in liquid and solid-state electrolytes, where red arrows represent metallic growth into the bulk of the separator and blue arrows show electric field lines [40]. 25
Figure 2.9- Schematic model of Li filament into a solid electrolyte, arrows at the rounded end represents the applied pressure and along the sides show shear traction due to friction [139]. ... 25
Figure 2.10- Measured elastic modulus of Al- and Ta-doped LLZO and respective fracture surfaces a) Al-doped and b)Ta-doped material [13]. 28
Figure 2.11- Crack propagation trajectories for LLZO with a) 85% relative density and b) 98% relative density [156]. 29
Figure 3.1- a) Typical load- and depth-time profile of LLZ and b) indentation load versus indentation depth..... 38
Figure 3.2 SEM topographies: a) specimen surface and the selected areas for micro-pillar testing. B) micro-pillar on single grain of Al-doped LLZO. 40
Figure 3.3- SEM topography of hot pressed LLZO- larger grains HP-Al:LLZO-LG a) specimen surface and the selected areas for micro-pillar testing with 10 and 5 µm diameter, b) typical micro-pillar of 10 µm diameter, c) and d) micro-pillar of 5 µm diameter. 41

Figure 3.4- SEM topography of hot pressed LLZO- small grains HP-Al:LLZO-SG a) specimen surface and the selected areas for micro-pillar testing with 10 and 5 µm diameter, b) typical micro-pillar of 10 µm diameter, c) and d) micro-pillar of 5 µm diameter. 42
Figure 3.5- Scanned surface of HP-Al:LLZO-SG before testing a) plan view; b) 3D view of micro-pillar. 43
Figure 4.1- Total Li-ion conductivity for all samples at room temperature as a function of density. Inset: representative Nyquist plot for 40Ta:LLZ at room temperature from 7 MHz to 36 Hz. 47
Figure 4.2- XRD patterns of pure LLZ, 60Ta and 36Al doped LLZ. 48
Figure 4.3 - SEM micrographs of a) un-substituted LLZ sintered in argon at 1150 °C for 10 h b) 60Ta:LLZ sintered in argon at 1150 °C for 10 h c) 20Al:LLZ sintered in argon at 1150 °C for 10 h and d) 20Al:LLZ sintered in air at 1200 °C for 20 h. 50
Figure 4.4 - (a) E_{mat} for 36Al- and 20Al-LLZ Al dopant and a data point for 28Al-LLZ from literature[13] (open square). (b) E_{mat} for 60Ta- 40Ta- and 20Ta-LLZ sintered in Ar for 10 h and a data point for 50Ta-LLZ from literature [13] (open square). Value for un-substituted LLZ is shown for comparison as dashed line. 52
Figure 4.5- SEM micrographs of indentation marks at 500 mN on 20Al:LLZ. 53
Figure 4.6- Effective mechanical properties (determined using high loads) plotted as function of porosity (a) effective elastic modulus (E_{eff}) (b) effective hardness (H_{eff}). 54
Figure 4.7- XRD pattern of 20Al:LLZ-2h. 59
Figure 4.8 - Mechanical properties of 20Al:LLZO-2h as function of depth displacement a) single results of elastic modulus b) single results of hardness c) average of E and H as function of penetration depth. 60
Figure 4.9 - Influence of porosity on mechanical properties of 20Al:LLZ sintered for different dwell times. 62
Figure 4.10- SEM micrographs of typical indentation marks at 1 N in a) 20Al:LLZO-20h; b) 20Al:LLZO-2h; c) 20Al:LLZO-40h. 63
Figure 4.11- SEM images of indented cross-sections of a) and b) 20Al:LLZ-2h lower and higher magnification and c) and d) 20Al:LLZ-40h lower and higher magnification. 64
Figure 4.12- SEM micrographs of typical indentation marks at 1 N in 20Al:LLZO-40h. 65
Figure 4.13- XRD spectra of LLZ:Ta-16h after sintering. 67
Figure 4.14- Compositional mappings of 40Ta:LLZ-16h for Zr, O, La, Al and Ta. 68

Figure 4.15- Elastic modulus and hardness curves of function of penetration depth of a) and b) 40Ta:LLZ-4h; c) and d) 40Ta:LLZ-8h; e) and f) 40Ta:LLZ-16h..... 69
Figure 4.16- Average of elastic modulus and hardness of 15 indentations for LLZ with dwell time 4 h, 8 h and 16 h as a function of the penetration depth. 70
Figure 4.17- SEM micrographs of indented surface of 40Ta:LLZ-16h after test..... 72
Figure 4.18-Influence of porosity on mechanical properties of 40Ta:LLZ. 73
Figure 4.19- SEM micrographs of indentation marks of 40Ta:LLZ-16h on pores, load of 1N: a) b) and c) indentations highly affected by pores; d) e) and f) indentations marks on denser areas. . 74
Figure 4.20- SEM micrographs of indented cross-section of 40Ta:LLZO-16h. 75
Figure 4.21- Cracks on 40Ta:LLZ-16h, indentation load of 1 N a) affected by local chemical composition, b) not affected by chemical composition. 76
Figure 4.22- EDX mappings of the previous indentation affected by two indentations presented in previous figure. 76
Figure 4.23- Cracks paths after Vickers indentation at 1 N of 40Ta:LLZ-16h. 77
Figure 4.24- Microscopy images of 40Ta:LLZO a) and b) optical images of surface before and after testing in air, respectively; c) and d) higher magnification SEM micrographs of Berkovich imprint at 100 mN, immediately transferred to SEM after mechanical testing. 78
Figure 4.25- SEM micrographs of Vickers indentation imprints at 10 N on 20Al:LLZO a) immediately after testing; b) and c) after 2 weeks exposed in ambient atmosphere, low and high magnification, respectively. 80
Figure 4.26- XRD pattern of specimen Al:LLZO. The cubic and tetragonal LLZO structures were identified with respect to the ICDD JCPDS card number 99-000-0032 and 99-000-0020, respectively. 82
Figure 4.27 - SEM topographies: (a) specimen surface and the selected areas for micro-pillar testing, and (b) micro-pillar. 83
Figure 4.28- (a) Young's modulus (*E*) and (b) hardness (*H*) obtained from 9 individual CMC tests, and (c) the average *E* and *H* values as a function of the indentation depth. 84
Figure 4.29- SEM micrographs after indentation imprints after applying loads of (a) 1 N, (b) 3 N and (c) 5 N, respectively. 85
Figure 4.30- SEM micrographs of sample morphology after applying VIF test (a) selected crack for investigation: P_1 is the end of the imprinted, P_2 indicates 0 μm from the imprinted tip and red

arrow indicate the direction of the FIB cutting (b-c) the extended cracks obtained from several SEM-FIB cross sectional, where the position P1 and P2 were located at the beginning and the end of the extended cracks. The crack depth vs. distance from the FIB cuts are plotted in (d), and the dash circle indicates the location of one large pore (radius ~ 2 µm). 87
Figure 4.31- (a) Load-displacement curves of micro-pillar indentation splitting tests and some corresponding SEM-FIB images for (b), (c) front and side view of pillar A and (d), (e) front and side view of pillar B. It is worth notice that a blister-like surface morphology was only observed after further FIB milling for topological observation in (c, e). A featureless surface morphology was observed in (b, d) during and immediately after indentation..... 90
Figure 4.32- (a) SEM micrograph and EDX composition analyses at different location around pillar C, (b) location 1, (c) location 2, (d) location 3 and (e) location 4. 92
Figure 4.33- SEM micrographs of precursor powders a) and b) conventional solid-state synthesis (SS) and b) solution-assisted solid-state synthesis (SASSR)..... 95
Figure 4.34 – SEM micrographs of hot-pressed Al-doped LLZO pellets a) Conventional solid-state synthesis HP-Al:LLZO-LG and b) Solution-assisted solid-state synthesis HP-Al:LLZO-SG..... 96
Figure 4.35 – a) XRD patterns of HP:LLZO; b) Nyquist plot at 25 °C for HP-Al:LLZO-LG and HP-Al:LLZO-SG 97
Figure 4.36 -Hardness and elastic modulus as function of penetration depth for a) HP-Al:LLZO-LG b) HP-Al:LLZO-SG c) HP-Al free:LLZO-LG d) HP-Al free:LLZO-SG. 98
Figure 4.37- SEM micrographs of Vickers indentation imprints after loading to 0.5 N, 1 N and 3 N a) HP-Al:LLZO-LG b) HP-Al:LLZO-SG c) HP-Al free:LLZO-LG d) HP-Al free:LLZO-SG. 100
Figure 4.38- Crack deflection along the grain boundary sample HP-Al:LLZO-SG indentation load 1 N..... 101
Figure 4.39- SEM micrographs of 1 N indentation highlighting crack deflection and crack bridging mechanisms in sample HP-Al free:LLZO-LG..... 102
Figure 4.40- Load-displacement curves of micro-pillar indentation splitting tests and SEM front view of pillars after testing in sample HP-Al:LLZO-LG, a) load-displacement curves of pillar with ~10 µm diameter; b) SEM micrographs of pillars A to I after testing; c) load-displacement curves of pillar with ~5 µm diameter; d) SEM micrographs of pillars F to J after testing. 103

Figure 4.41- SEM micrographs of cross-sectional FIB cut of pillar H (~ 5 µm diameter) after indentation splitting. 105
Figure 4.42- Load-displacement curves of micro-pillar indentation splitting tests and SEM front view of pillars after testing in sample HP-Al:LLZO-SG a) load-displacement curves of pillar with ~10 µm diameter; b) SEM micrographs of pillars 1 to 5 after testing; c) load-displacement curves of pillar with ~5 µm diameter; d) SEM micrographs of pillars 6 to 10 after testing. 106
Figure 4.43- EDX of pillar 9 (5 µm diameter) after testing sample HP-Al:LLZO-SG. 107
Figure 4.44 –SEM micrographs of cross-sectional FIB cut on HP-Al:LLZO-SG of a) pillar 5 (~10 µm diameter) b) pillar 9 (~5 µm diameter). 109

1. Introduction

The limited availability of fossil fuels along with an increasing concern about the environmental pollution, associated with CO_2 emission, has raised the need to develop sustainable energy sources. Renewable energy sources like wind power and solar energy are intermittent, the hydraulic power and the former ones have seasonal variations, therefore requiring that energy is stored to balance fluctuations. In order to make renewable energy more feasible, advanced energy storages system have to be developed. Recently, batteries indicated to be a good alternative and economically viable [1-3]. In addition, the increasing demand for zero emission vehicles, portable electronic devices, stationary and non-stationary energy storage systems, has boosted the scientific and technological interest in batteries [4-6].

A battery is composed mainly of anode, cathode and electrolyte. Oxidation and reduction reactions take place at the electrodes, and the electrolyte controls the ionic flux between electrodes. Currently conventional batteries are based on organic solvents as liquid electrolytes [7], due to their very high ionic conductivity; however, they suffer from a serious drawback related to their flammability and leakages [8, 9]. All-solid-state batteries (ASSBs), such as Na-ion batteries, Lithium-Sulphur (Li-S), Lithium ion batteries (LIBs) could satisfy the requirements, since solid state electrolytes are expected to offer a high ionic conductivity along with a low electronic conductivity and, in addition, higher thermal and chemical stability [10]. A large number of inorganic oxides and non-oxide fast ion conductors have already been investigated for the use in solid state batteries, i.e. NASICON materials, garnet structured type, LIPON type and perovskite types [11, 12].

Although there is a large number of studies that focus on characterization and improvement of microstructure and conductivity of solid state electrolytes, there are only few investigations on mechanical behavior, especially for garnet structured [13-15]. However, aiming towards a long-term reliable operation, an important aspect is the characterization of these materials with respect to mechanical limits under operation relevant conditions. Mechanical boundary conditions and operation as an electrolyte might induce micro-cracks, structural and mechanical failure that will terminate the battery life, especially materials with brittle nature and limited mechanical stability can significantly compromise the operation relevant safety of solid state batteries. Therefore,

studying relevant mechanical properties of solid electrolytes is important to warrant long-term reliability of solid state batteries.

Hence, the focus of this thesis is to characterize mechanical aspects of a novel garnet solid electrolyte $Li_7La_3Zr_3O_{12}$ (LLZO), determining elastic modulus, hardness and fracture toughness, and established a correlation of results with microstructural features, such as grain size, phases and dopants as well as grain boundaries and pores. Mechanical properties are evaluated using a macroscopically non-destructive indentation test, on nano- and micro-scale. An advanced experimental approach is implemented based on the indentation testing, implementing the continuous multi-cycling test that is compared with standard indentation mode results. In addition, a novel pillar indentation splitting test is implemented for measuring the fracture toughness of the individual ceramics grains, permitting insight into the effect of grain and grain boundary.

More specifically, the results concentrate on three aspect that are considered in three separate sub-chapters in the results, i.e. the effect of doping on the mechanical and electrical properties in order to find an optimum composition, second, optimization of the characterization methodology to assess the fracture toughness via combination of indentation testing and micro-pillar, third, determination of the properties for a dense composition to assess differences with respect to the first section in order to clarify the aspects related to porosity and grain size and compositional variation.

2. Literature Review

In the following chapter current storage systems and solid-state batteries are reviewed. Mechanical characteristics, with focus on elastic, apparent plastic and fracture properties, in particular local mechanical testing such as indentation and the novel micro-pillar splitting test are outlined. In addition, mechanical considerations for operation different solid electrolytes and their mechanical properties are revised, and garnet structure materials mechanical properties are presented.

2.1. Batteries

2.1.1. Conventional and solid-state batteries

Electrical energy storage systems in the form of batteries are widely used in portable electronic equipment such as cell phones, laptops, medical applications and a power source for transportation, either in electric vehicles or aerospace application, in addition to energy supply systems for national electric grid and smart grids [16, 17]. Thus to realize their full potential, the development of safe and high energy density batteries lithium battery technology has been the focus of studies to overcome challenging scientific and technological issues [18-20].

Conventional batteries consist of several electrochemical cells connected in series or parallel to provide the required voltage and capacity. Each cell is composed by an anode (negative electrode) and cathode (positive electrode), separated by an electrolyte solution containing dissociated salts, which enables ions transfer between two electrodes, see Figure 2.1. In its most common structure it contains a graphite anode, a lithium metal oxide cathode (e.g. $LiMO_2$, $LiCoO_2$) and a mixed organic solvent (ethylene carbonate-dimethyl carbonate EC-DMC) and a porous separator [9, 21].

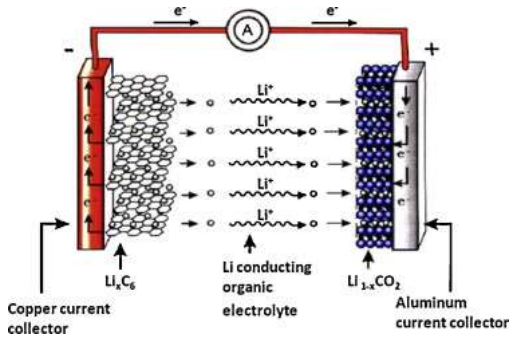

Figure 2.1- Schematic illustration of traditional lithium-ion battery [9].

During charging lithium is oxidized at the anode and lithium ions are released from the carbon along with electrons, giving the follow reaction [22, 23]:

$$Li_6 \rightarrow x \cdot Li^+ + x \cdot e^- + C_6$$

Lithium-ions are absorbed by lithium dioxide at the cathode and the electrode is reduced and receives electrons:

$$Li_{1-x}CoO_2 + x \cdot Li^+ + x \cdot e^- \rightarrow LiCoO_2$$

Therefore the overall reaction is:

$$C_6 + LiCoO_2 \leftrightarrow Li_xC_6 + Li_{1-x}CoO_2$$

The rapid insertion and removal of lithium from anode to cathode structures can lead to significant stresses and strains in battery electrodes [24-26]. A recent investigation revealed that stress scales are proportional to lithiation/delithiation rate and dramatic changes in electrochemical stiffness due to formation of different graphite-lithium intercalation compounds during cycling [27]. For example for $LiNiFeF_6$ used as cathode the lattice parameter (and weight fraction) changes, causing an anisotropic lattice expansion, increasing the unit cell volume by 6% and yielding a reduction in lattice parameter ratio of ~4% [28].

For the negative electrode, anode materials such as graphite show a volume expansion of 10% [29], silicon and tin high capacity anodes have a much larger volume change of up to 300% [30,

31]. This lithiation-induced stresses causes cell degradation, loss of connectivity to the current collector, furthermore, stresses and delamination at the cell level are generated and can reduce the necessary good electrical contact among the components [24] and capacity fade after cycling [32].

Regarding liquid electrolytes, which are organic solvents supported by a porous polymeric matrix that help transport Li-ions to/from the cathode and anode, they are highly reactive, especially when combined with lithium metal as anode [33, 34]. This results in a flammable materials combination when thermal runaway happens in the battery system [19, 35, 36]. Other common shortcomings are limited range of operation, leakages, corrosion of the electrodes and growth of the metal dendrites from the anode to cathode throughout the electrolyte leading the internal short circuiting [37, 38].

In order to eliminate the drawbacks of liquid electrolyte based systems, solid electrolytes have been proposed as suitable and safer replacements, which is the principle of solid-state batteries [8, 39]. Overall, solid-state batteries are systems that have shown to be of great interest because of potential benefits in gravimetric and volumetric energy density, operable temperature range and safety in comparison to the conventional liquid electrolyte based system [40].

Figure 2.2 is a schematic representation of a lithium based solid-state battery, where the arrows show the direction of ion movement during charging and discharging process, respectively, and some available anode, electrolyte and cathode combinations.

Similar as in the case of a liquid electrolyte battery, during the charging process Li-ions move across the solid electrolyte toward the anode, during discharge the reverse process takes place. The cathode supplies the battery with ions during the charging process, therefore it must be stable even under this condition. Common cathode materials are lithium cobalt oxide (LCO) and lithium manganese oxide ($LiMn_2O_4$). The first has a relatively high specific energy, around 150 $mAh \cdot g^{-1}$, however, is more expensive due to the necessary use of cobalt [41, 42]. The second is based on a spinel structure, which provides an easier path for lithium ions during the lithiation/delithiation process [20]. Lithium-based phosphates ($LiFePO_4$) and vanadium based oxides have also been tested, despite the high self-discharge rate and low output voltages, which result in a reduced durability [8, 20, 43].

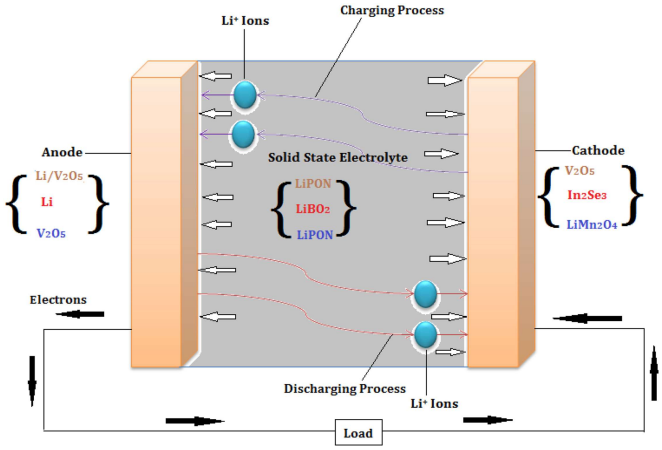

Figure 2.2- Schematic representation of a lithium based solid-state battery [8].

Also spinel lithium based oxides (LTO), carbon and graphite based materials are commonly used anode materials in solid-state batteries, however, graphite based materials cannot satisfy the requirements due to limitations associated with power energy density and safety [44, 45]. LTO is being considered as a promising anode, since it possesses a negligible volume change during charging and discharging, resulting in an excellent cycle longevity [46-48], especially compared to conventional graphite, which expands up to 10% in volume during charging, and silicon, which has volumetric expansion of up to 400% upon full lithiation [49, 50].

Despite the importance of the performance of cathode and anode materials, the solid-state battery performance highly relies on the diffusion of ions through the electrolyte. Hence, an excellent solid electrolyte material should have high ionic conductivity, low or zero electronic conductivity, wide electrochemical stability window and last, but not least, excellent mechanical properties [51, 52].

The utilization of a solid electrolyte enables the use of pure lithium metal as anode, and an increase in volumetric energy density of up to 70% can be achieved compared to a conventional anode system [53, 54]. However, safety issues have to be taken into consideration when using Li anodes. Internal short circuits caused by Li-metal plating, also called lithium dendrites can lead to a short circuit of the system [55]. Hence due to their importance, dendrites are discussed in more detail in section 2.2.4.

2.1.2. Solid-state electrolytes

In the following subsection, the state-of-the art of solid electrolyte materials and operation relevant mechanical considerations are discussed, focusing on inorganic electrolytes, especially garnet-structured.

Solid-state electrolytes (SSE), also called superfast ionic conductors, exhibit a conductivity comparable to liquid electrolytes, $>10^{-2}$ S·cm^{-1} [56]. Apart from being ion conductors, solid electrolytes also serve as separator, avoiding the direct contact of electrodes. The solid structure simplifies the assembling process, since an organic liquid electrolyte, electrolyte salt or binder is not required [56]. They can be inorganic, polymers or composites like polyethylene oxide (PEO), glasses or inorganic ceramics, with different structures such garnet, LISICON, NASICON and sulfides [57, 58].

Polymer electrolytes

The advantage of polymer electrolytes is their good processability, high safety and flexibility. They can be roughly classified as dry solid polymer electrolytes, composite polymer and polymer gels [59, 60]. The dry solid polymer is mechanical stronger, but has a lower ionic conductivity, when compared to gel, that requires a mechanical support, but typically has higher conductivities [52]. However, the disadvantages of such systems are related to the instability of electrode/electrolyte interface and narrow operation temperature range [58, 61].

Solid polymer electrolytes are based on polymer-salt complexes with no liquid component being present, which are added to provide lithium ion conductivity [62, 63]. PEO is the most common and has been used for a long time, consisting of a semi-crystalline polymer able to dissolve lithium salts, which have a melting point around 65 ºC [64]. They can be prepared by solvent casting, hot pressing extrusion and their conductivity is low at room temperature ($\sigma < 10^{-6}$ S·cm^{-1}), but increases above the melting temperature, reaching 1 mS·cm^{-1} at 80 – 90 °C, where the entire polymer is in a viscous liquid state [58]. The conduction mechanisms are the ion transport in the amorphous region, so the conductivity increases with decreasing degree of crystallization [65].

Another way to improve the ionic conductivity has been the addition of ceramic particles into the organic polymer host, such as alumina or silica, the so-called composite polymer electrolytes [66,

67]. In this context, ceramic fibbers are added in order to decrease the glass transition temperature which helps to improve the conductivity [68].

Inorganic solid electrolytes

There are several types of inorganic electrolytes that are being considered for lithium solid-state batteries, the electrolytes that are being most explored are sulfides and oxides such as perovskites, NASICON and garnet materials. A brief review of several types of inorganic solid electrolytes is presented in the following sections; physical, chemical and mechanical properties are discussed.

The operation temperature target is room temperature; however, ceramic solid electrolytes are also well suited for high-temperature applications [52], especially due to the conduction mechanism, that occurs via movement of ions along the defects, which requires an activation energy, the conductivity of these compounds increases with increasing temperature [52].

2.1.3. Properties of solid-state electrolytes (physical, chemical and mechanical properties)

Sulfides

Sulfides-types, such as Li_2S-SiS_2 and Li_2S-P_2S_5 system, are considered to be a very promising class of electrolytes and have been widely studied [69, 70]. The so-called class thio-LISICON (lithium superionic conductor) $Li_2SGeS_2P_2S_5$ was found in this system [71] and showed conductivity of 2.2×10^{-3} S·cm^{-1} at 25 °C. Recently, $Li_{10}GeP_2S_{12}$ was considered, exhibiting a Li-ion conductivity of 1.2×10^{-2} S·cm^{-1} at room temperature, the highest reported for a solid electrolyte [72]. However, the chemical stability of this class of materials is extremely low, being hydroscopic and sensitive to oxygen and the stability in contact with high voltage cathode materials is still uncertain [56, 73, 74].

Perovskite structured

Perovskite is a general term for a structural family of materials with general formula ABO_3 with alkaline rare or earth metal ion in A-sites and transition metal ions in B. A representative material of this class is $Li_{3x}La_{2/3-x}TiO_3$ (LLTO), which possess a bulk conductivity of 1×10^{-3} S·cm^{-1} at room temperature [75]. However, when in contact with lithium metal it reacts easily, the titanium

ion is reduced from Ti^{+4} to Ti^{+3} and it becomes a mixed conductor, thus, not being suitable as a solid electrolyte when in contact with lithium metal [56, 75].

NASICON

These materials have the general formula $AM_2(PO_4)_3$, with A sites occupied by Li, Na or K, and usually M sites occupied by tetra-valence ions such as Ge, Zr, or Ti [57]. The term NASICON (**Na**$^+$ **S**uper **I**onic **Con**ductor) emerged in 1976 as Na^+ fast ionic conductor with high ionic conductivity [11]. Lithium ionic conductors in NASICON structure can be prepared by mechanical milling and spark plasma sintering, within the $LiT_2(PO_4)_3$ system (LTP), the aluminum substitution (LATP) was the most effective leading to ionic conductivities in the order of 10^{-4} S cm^{-1} and a very high conductivity for nano-grains in the order of 10^{-3} $S{\cdot}cm^{-1}$ [76, 77].

Another promising system under investigation, due to its high electrochemical stability and wide electrochemical window, is $Li_{1+x}Al_xGe_{2-x}(PO_4)_3$ (LAGP), which is a glass-ceramic system with total ionic conductivity in the range of 10^{-3} $S{\cdot}cm^{-1}$ to 10^{-1} $S{\cdot}cm^{-1}$ at room temperature up to 107 ^{o}C [78]. Recently, LAGP was incorporated in a polymer as a matrix, leading to a composite with good ionic conductivity, good compatibility with the lithium electrode and high mechanical stability [79].

To conclude, NASICON-structure ionic conductors are suitable for use as solid electrolytes due to their chemical stability, wide electrochemical window and especially due to their high ionic conductivity at room temperature [56].

Garnet structured

Also garnet-structured Li-ion conductors have attracted attention as potential solid electrolytes for lithium ion batteries (LIBs) [80]. The general chemical formula of garnet metal oxides is $A_3B_2C_3O_{12}$ (A = Ca, Mg, La or rare earth; B = Fe, Al, Ga, Ge, Mn, Ni or V; C = Si, Ge, Al) and their structure consist of CO_4 tetrahedral and BO_6 octahedral positions connected via edge sharing [81].

Lithium rich or Li-stuffed garnets contain five to seven Li atoms per unit cell; this is more than can be accommodated at the tetrahedral sites, leaving excess Li, which occupies the octahedral sites. In case of the garnets $Li_5La_3M_2O_{12}$, La and M sites can be substituted by various metallic

ions leading to $Li_6La_2M_2O_{12}$ (M = Mg, Ca, Sr, Ba, Sr, Ba) and $Li_7La_3C_2O_{12}$, (C = Zr, Sn) and $Li_7La_3Ta_2O_{13}$ [82].

Particularly $Li_7La_3Zr_3O_{12}$ (LLZO) exist in two different polymorphisms cubic and tetragonal phase; the cubic phase being the most interesting due to its higher ionic conductivity (~10^{-4} S·cm^{-1} [83]) compared to the tetragonal phase (~10^{-6} S·cm^{-1} [84]). The large difference in conductivity is explained by order-disorder arrangements, since in tetragonal LLZO tetrahedral and octahedral sites are completely ordered by Li atoms and vacancies, while in cubic LLZO an intricate Li-vacancy disorder exists in those sites [84]. Therefore, dopants are expected to increase the degree of vacancy disorder within the Li sub-lattice and stabilize the cubic crystal structure, yielding enhanced hopping paths for Li^+ and an increased conductivity; potential doping elements can be Al^{+3}, Ta^{5+} or Ga^+ [11, 85-87].

LLZO can be synthetized by solid-state reaction and sol-gel techniques [81, 88]. In order to synthetize dense LLZO, high temperature processes are required, which results in lithium deficiencies, a way to overcome this problem is adding more lithium to compensate the lithium losses during the high temperature sintering process, or doping with Al or Ga, which lowers the required sintering temperature, achieving a cubic phase [86, 89]. However, a reduction in sintering temperature raises a new problem related to secondary phase precipitation, which can hinder the ionic transport in the material [11].

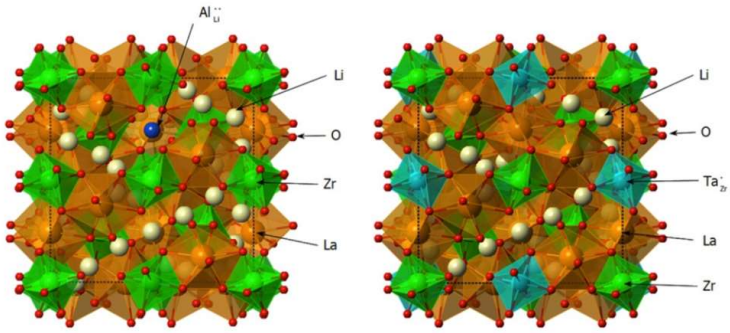

(a) $Li_{6.25}Al_{0.25}La_3Zr_2O_{12}$ (b) $Li_{6.5}La_3Zr_{1.5}Ta_{0.5}O_{12}$

Figure 2.3- Schematic atomic structure of a LLZO cell a) Al-doped and b) Ta-doped [13].

Larraz et al. [90] reported the presence of two cubic phases in non-doped LLZO, one formed at low temperature and another at high temperature, the former one appears in the range of 100 ºC to 200 ºC and is attributed to the presence of water either in the atmosphere or in the precursor materials, the second undergoes a reversible phase transition around 635 ºC when not exposed to humidity anymore. In another study, the phase transformation from tetragonal to cubic at around 150-200 ºC was associated with CO_2 absorption into the structure and the extraction process occurred around 450 ºC, resulting in a phase transformation back to tetragonal [91]. The phase stability of cubic LLZO is influenced by the Al and Li concentration, and an optimum concentration was found to 0.24 moles of Al and 6.24 moles of Li [86].
The chemical stability of cubic $Li_7La_3Zr_3O_{12}$ was investigated in various aqueous solutions and a surface morphology change occurred in HCl and LiOH solutions, leading to a significant decrease in conductivity, which was attributed to a possible Li^+/H^+ ion-exchange reaction after treatment in water [92]. Further studies noted that the ion exchange occurs also in humid environments [93, 94].

Mechanical properties of solid electrolytes

In addition to a high ionic conductivity, the solid electrolytes should exhibit adequate mechanical properties, which includes satisfying elastic, plastic and fracture properties [95]. In this chapter, give a brief review of the mechanical behavior of oxide-based electrolytes is introduced.

The elastic modulus represents the response of solid materials to a deformation in the elastic range and it is an important property for solid electrolytes. Considering the linear elasticity theory by Monroe and Newman [96] a high shear modulus (which is coupled with the elastic modulus) of electrolytes would prevent the initiation of dendrites during charging at electrode/electrolyte interface, this subject is addressed in more details in the section 2.2.4.1.

Considering the importance of the solid electrolyte within the battery and the brittle behavior of ceramics, the fracture toughness is also a crucial property for application, since it represents the ability of a material containing a crack to resist fracture [95]. In general, polycrystalline ceramics

exhibit fracture toughness values from 1 to 5 MPa·m$^{0.5}$ [97, 98], in fact, much lower values when compared to metals ~20 to 100 MPa·m$^{0.5}$ [99].

So far, the mechanical properties of solid electrolytes materials have only received limited attention and limited information on chemo-mechanical properties are available in literature [95]. Table 2.1 presents a summary of recent studies with respect to mechanical results of differently structured ceramic solid electrolytes material. Mechanical properties of garnet-structured LLZO are discussed in more details in the next subsection.

Table 2.1- Mechanical properties of ceramic solid electrolyte materials (adapted from [100]).

Structure	Compound	Processing method	Testing method	Elastic Modulus (GPa)	Fracture toughness MPa·m$^{0.5}$
NASICON LATP	$Li_{1.3}Al_{0.3}Ti_{1.7}(PO_4)_3$ [101]	-	Ring-on-ring	81–115	1.1 ± 0.3
LIPON (amorphous)	$Li_xPO_yN_z$ [102]	Film magnetron sputtered	Nanoindentation	77	-
Perovskite	$Li_{0.33}La_{0.57}TiO_3$	Solid state-hot pressed 1100 °C	Nanoindentation	186 ± 4	0.64 - 1.31
	$Li_{0.33}La_{0.57}TiO_3$ [103]	Sol gel-hot pressed 1100 °C	Nanoindentation	200 ± 3	0.89 - 1.33
Sulfide	Li_2S-P_2S_5	Hot pressed 20-190 °C/ 360 MPa	Ultrasound velocity	18-25	-
	Li_2S-P_2S_5 [104]	Cold pressed 180-360 MPa	Ultrasound velocity	14-17	-
	$Li_{10}GeP_2S_{12}$		Atomistic simulation	~38	-
	Li_2S-P_2S_5		Nanoindentation	~18	0.23 ± 0.04

Amorphous LiPON films in a thickness range from 1 to 10 µm were characterized by nanoindentation in [102], the elastic modulus was found to be 77 GPa and the hardness was 3.9 GPa. Perovskite $Li_{0.33}La_{0.57}TiO_3$ prepared using a solid state (SS) and sol-gel (SG) procedure were also characterized [103], yielding fracture toughness values of ~1 MPa·m$^{1/2}$; although fracture toughness of SG was slightly higher than SS, this effect has been attributed to enhanced crack deflection along grain boundaries. Sulfide Li_2S–P_2S_5 glassy solid electrolytes were investigated by ultrasound velocity measurement yielding moduli in the range of 18-25 GPa and those of cold-pressed pellets were about 14-17 GPa [104].

From Table 2.1 it is important to notice that LLTO has the highest elastic modulus value (~200 GPa) and sulfide based materials have the lowest values (~18 to 38 GPa). Higher elastic modulus

means that the material is less deformable. Another important aspect that needs to be considered with respect to the materials elastic behavior, ultrasound velocity test and ring-on-ring test measure the bulk polycrystalline materials properties, whereas for nano-indentation the values are localized responses, usually from single grains within the sample, hence comparison of such data requires careful consideration of the testing method. Regarding the fracture toughness, NASICON and perovskites all possess values of approximately 1 $MPa \cdot m^{0.5}$, however, sulfides showed the lowest values of ~0.23 $MPa \cdot m^{0.5}$. These values suggest that these materials are not very resistant to crack growth due to their brittle nature.

2.2. Mechanical characteristics

2.2.1. Elastic behavior (elastic modulus)

The elastic modulus *E* measures resistance of a material to elastic deformation. It is a property of the materials which depends on the bonding forces between atoms and crystal structure of a solid. This property can be determined with different methods, uniaxial and biaxial bending tests are widely used and also the non-destructive indentation method is often used. In the present work, the elastic modulus is determined using the indentation method.

Indentation

Indentation testing is an established materials characterization technique and has been used for decades to determine quantitative mechanical properties of also brittle materials to assess quasi-static and dynamical elastic modulus, hardness and fracture toughness [105, 106]. The advantage of this method is that it is fast and it is considered to be a non-destructive test since only a small specimen volume is required and deformed.

When the indenter is driven into the material during loading, elastic and plastic deformation occurs, which typically results in a hardness impression conforming to the shape of the indenter up to some contact depth. During withdrawal, only the elastic portion of the displacement is recovered. The elastic modulus is usually determined from load-displacement curve, applying the Oliver and Pharr analysis procedure [105], see Figure 2.4. The elastic modulus is calculated from the unloading curve and is characteristic for the elastic behavior of the material. Hardness is related to the plastically deformed volume and is derived from maximum load and corresponding contact depth [106].

a) b)

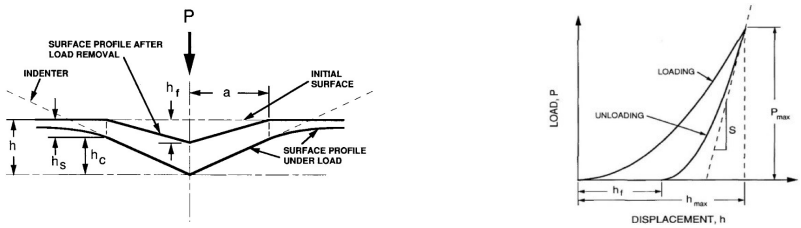

Figure 2.4- Schematic representation of a) main parameters describing the indentation process b) typical indentation load–displacement curve, where P_{max} is the max. indentation load, h_{max} the indenter displacement at peak load, h_f the final depth of the contact impression after unloading and S the initial unloading stiffness [105].

To obtain the elastic modulus the unloading part of the depth-displacement curve is utilized and the reduced modulus (E_r) is obtained, subsequently the materials elastic modulus can be calculated [105]:

$$E_r = \frac{\sqrt{\pi}}{2 \cdot \beta} \frac{S}{\sqrt{A_p}} \qquad \text{Eq. 1}$$

$$E = \frac{(1 - \nu_s^2)}{\frac{1}{E_r} - \frac{(1 - \nu_i^2)}{E_i}} \qquad \text{Eq. 2}$$

where E_r is the reduced modulus, β a indenter constant (for Vickers indenter 1.0124 and Berkovich is 1.034), and S the slope of unloading curve = dP/dh and A_p is the projected contact area determined from the contact depth and the predetermined calibration function of the indenter system. E is the indentation derived Young´s modulus of the material, ν_s is the Poisson's ratio of sample, ν_i the Poisson's ratio of indenter 0.07 and E_i the elastic modulus of diamond indenter 1141 GPa.

2.2.2. Plastic behavior (hardness)

Additionally, indentation testing permits a determination of the hardness (*H*), which is a property often used to characterize the non-elastic behavior of advanced ceramics. The hardness of a material is its resistance to the formation of a permanent surface impression by an indenter and also can be defined as being related to resistance of a material to non elastic deformation (yield), scratching and erosion [107]. The value of material´s hardness depends, in addition to its elastic modulus, on the geometry of the indenter and, overall, the microstructure.

The test consists of a shard diamond Vickers indenter driven into the material, that creates a pyramidal impression and hardness is then derived from [105]:

$$H = \frac{P_{max}}{A_p} \qquad \text{Eq. 3}$$

where P_{max} is the maximum applied load, A_p is the projection area of contact at peak load. Regarding the specimen preparation for the test, surface flatness and parallelism are important, in order to obtain correct data. An important aspect to be considered is that hardness can depend on the applied load, and a full characterization involves testing over a broad range of indentation forces, i.e. for ceramics materials, hardness often decreases with increasing load. This phenomenon is known as indentation size effect (ISE)[108].

2.2.3. Fracture properties (fracture toughness)

The fracture toughness (K_{IC}) is an important property of ceramic materials and describes the ability of a material containing a crack to resist fracture. It can be tested for example by single edge notch bending, indentation-strength-in-bending test and indentation [109]. Recently, a novel method was developed to measure fracture toughness aided by nano-indentation methods, the so-called micro-pillar splitting test, which is based on loading a Focus Ion Beam (FIB) produced micro-pillar using a sharp tip [110], therefore in this work I chose indentation and micro-pillar splitting test to obtain K_{IC} at different scales, comparing methods as well as properties of single grains and polycrystalline ceramics.

2.2.3.1. Vickers indentation fracture

Indentation testing also may be used to quantify the fracture toughness of brittle materials, in this case, the applied load should be high enough to initiate and propagate cracks from the vertices of the impression, an idea initially recognized by Palmqvist [111]. The fracture toughness determination by Vickers Indentation Fracture (VIF) technique, also called indentation fracture toughness has been widely used for evaluation of toughness on small samples [112] and requires a rather simple sample preparation, by preparing a smoothly polished and parallel surfaces without pre-cracking [113], in particular in cases where only limited material is available for testing.

The surface is indented with a Vickers pyramidal indenter and the K_{IC} calculation involves the measurement of the crack lengths at a particular applied load and, in addition, knowledge of elastic modulus and hardness. Depending on the shape and cracks lengths different calculation approaches might be used [114-116]. If the relationship of radial cracks lengths l and half-diagonal of the impression a is between $0.25 \leq l/a \leq 2.5$ the crack system can be described by a Palmqvist type shape (Figure 2.5), which typically formed in the low-load regime. In the case of median-radial cracks with well-developed crack length, typically for higher loads, the derived relationships are based on half-penny shaped crack model, the requirement is $c/a \geq 2.5$, where c is the radial crack size [117].

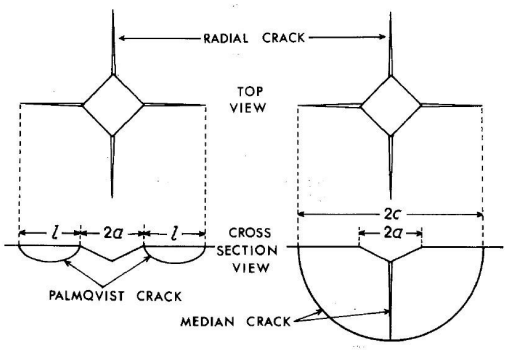

Figure 2.5- Schematic of Palmqvist cracks and median-radial cracks [114].

Different relationships have been reported in literature in order to determine fracture toughness by Vickers indentation, Table 2.2 compiles several relationships for Palmqvist and Median crack systems based on literature [118].

Table 2.2- Equations to calculate K_{IC} values from indentation tests.

Palmqvist crack system		**Equation No**
Lawn and Fuller [119]	$K_{IC} = 0.0515\frac{P}{c^{3/2}}$	**Eq. 4**
Evans and Wilshow [120]	$K_{IC} = 0.079\ \frac{P}{a^{3/2}}\log\left(4.5\ \frac{a}{c}\right)$	Eq. 5
Niihara et al [114]	$K_{IC} = 0.035\left(\frac{l}{a}\right)^{-1/2}\left(\frac{H}{E\phi}\right)^{2/5}\left(\frac{Ha^{0.5}}{\phi}\right)$	Eq. 6
Niihara [117]	$K_{IC} = 0.048\left(\frac{l}{a}\right)^{-1/2}\left(\frac{H}{E\phi}\right)^{2/5}\left(\frac{Ha^{0.5}}{\phi}\right)$	Eq. 7
Median crack system		
Lawn and Fuller [119]	$K_{IC} = 0.0726\frac{P}{c^{3/2}}$	Eq. 8
Evans and Charles [121]	$K_{IC} = 0.0752\frac{P}{c^{3/2}}$	Eq. 9
Niihara et al [122]	$K_{IC} = 0.129\left(\frac{c}{a}\right)^{-3/2}\left(\frac{H}{E\phi}\right)^{-2/5}\left(\frac{Ha^{0.5}}{\phi}\right)$	Eq. 10
Lawn et al. [123]	$K_{IC} = 0.014\left(\frac{E}{H}\right)^{1/2}\left(\frac{P}{c^{3/2}}\right)$	Eq. 11
Anstis et al. [115, 124]	$K_{IC} = 0.016\left(\frac{E}{H}\right)^{1/2}\left(\frac{P}{c^{3/2}}\right)$	Eq. 12
Tanaka [124]	$K_{IC} = 0.0725\left(\frac{P}{c^{3/2}}\right)$	Eq. 13

ϕ is the constraint factor taking a value of 3.

Since for VIF technique a crack length measurement is required, attention has to be given to accurate measurement of the length of the induced cracks. Variation in optical and electronic microscopes can cause uncertainties in K_{IC} values [113]. In addition, a complex residual stress state remains in the surface of the surrounding material, and at higher loads multiple cracks might be formed experiencing extensive lateral cracking and considerable spalling as well as crack growth during unloading that is not considered in the relationships. Hence, cracks may form and grow either during loading or unloading, and it can be the case that a transformation of Palmqvist crack system to median crack occurs [113].

It is hence important to note that, despite the complex crack system induced by indentation and the considerable residual stress, indentation fracture toughness is used here as fracture toughness measurement method in order to compare material´s behavior and relate to reference values from literature. Therefore, in the present study, different equations were selected according to the relationship *l*/*a* and *c*/*a* cited above and the crack system that best describes the crack behavior of individual specimens.

2.2.3.2. Micro-pillar Indentation Splitting test

The micro-pillar indentation splitting testing is a novel test developed by Sebastiani et al for measuring fracture toughness of thin ceramic coatings, and based on the loading of focus ion beam (FIB) milled micro-pillars by a sharp indenter [110, 125]. This technique has been successfully used to determine the fracture toughness of titanium nitride and (TiN) chromium nitride (CrN), composites and recently also for spinel materials for battery application [110, 126], see Figure 2.6.

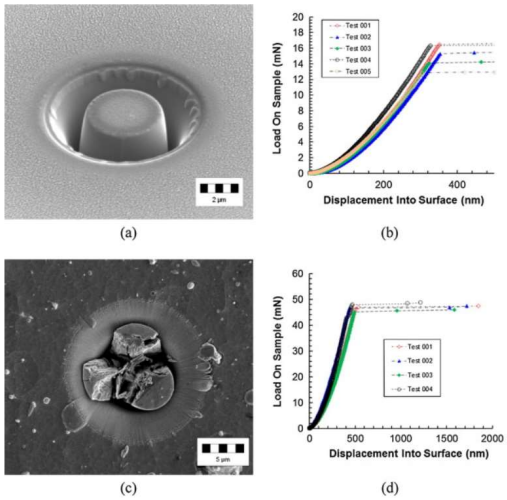

Figure 2.6-SEM micrographs of pillar on ceramic samples and the representative load-displacement curves: a) and b) silicon single crystal; c) and d) CrN (adapted from [127]).

The main advantage of this technique is that neither crack geometries nor crack sizes need to be measured, contrary to conventional indentation fracture toughness determination methodologies.

The fracture toughness is derived from the splitting fracture loads that can be determined from pop-in effects in the displacement-load curves and is then calculated using the following equation [110]:

$$K_{IC} = \beta \cdot \frac{P_c}{R^{3/2}} \qquad \text{Eq. 14}$$

where P_c is the critical load at failure, β is a dimensionless coefficient that depends on the elastic-plastic properties, and R is the pillar radius.

Primarily, β was estimated only for TiN and CrAlN-Si_3N_4 [110], however, finite element analyses was applied recently for other ceramics materials in order to investigate effects of materials compliance on this parameter [125]. As a result, the dimensionless coefficient can now be calculated on the basis of their work as $\beta \approx 0.057+0.0149\ E/H$ [110, 128], using the E and H obtained experimentally for any specific material.

This technique has several advantages compared to VIF and other micro-mechanical testing methods currently available. The design of a micro-pillar for testing is relatively simple, there is no necessity for accurate image correction, crack length measurement or for minimizing the materials residual stress [129, 130], i.e., when the aspect ratio height to diameter is greater than 1, residual stresses on the upper portion of the pillar and substrate compliance are negligible with respect to the critical load of failure [110, 125]. Even though the crack length and geometry are not required, they can be assessed after testing via FIB/SEM analyses and additional information on the crack path can be obtained.

The instability load and pillar radius needed in Eq. 14 are easily measured and fracture toughness can be derived, which highlights the feasibility of this method. In addition, since the pillar splitting can occur at shallow indentation depths and the FIB damage is considered to be surface localized and far from the position of the crack and propagation [110], the potential FIB-induced damage is commonly accepted to be less significant compared to other micro-mechanical testing methods, such as single- and double-cantilever bending, which is also the case for battery materials possessing a high ion-conductivity, which might result in larger damage induced by the Ga^+ ions [131].

It was suggested by the developers of this technique that effects of FIB machining on micro-pillars geometry are expected to less significant than for the micro-cantilever geometry, since the crack is nucleated and propagated inside the pillar far from the damaged free surface [110]. Nevertheless, such effects have to be considered for the nucleation of the initial and subcritical crack, but not for the critical load of the instability, where critical crack extension from the surface occurs [132].

Recently, Lauener et al. [132] reported a study on the influence of testing rate and positioning accuracy, furthermore, a comparison of samples produced by different methods, such as lithography, gallium FIB and Xenon FIB, as function of pillar size was established. In this work, Silicon was investigated and the technique was shown to be insensitive to loading rate, however, a significant lower toughness values was obtained in the case of off-center indenter positioning. The authors suggested that the positing accuracy should be around 20% of the pillar´s center to provide an accurate measurement. Regarding the FIB damaged, it was found that a significant increase can occur in the apparent toughness at smaller pillars sizes and the influence diminishes for pillar diameters greater than 10 μm [132].

In order to minimize the effect of the gallium FIB damage on the fracture toughness values of CrN the ion current was reduced from 100 pA to 1 pA [133]. With reduced probe current used for notching the fracture toughness values reduced close to values of pillar splitting method, without significant effect of ion damage. Another approach to diminish FIB damage can be the use larger pillars diameter or thermal annealing [132, 134]. Conclusively, this method opens up a new experimental direction for battery materials characterization aiding an understanding of the coupled electro-chemo-mechanical behavior from a viewpoint of local mechanical degradation under cyclic charging.

2.2.4. Mechanical considerations of solid-state electrolytes

Currently, most batteries are based on liquid electrolytes systems, although they offer benefits like excellent wetting electrolyte surface and high ionic conductivity, they have drawbacks such as reduced electrochemical and chemical stability, and poor safety [51]. Solid-state electrolytes (SSE) replacing liquid electrolytes could eliminate safety concerns and also endeavor new possibilities as new battery chemistries and design aspects [39, 58]. All-solid-state lithium ion batteries

(ASSLiBs) have a similar operational principle as the traditional LiBs, where lithium ions deintercale from the cathode materials and transport trough the electrolyte towards the anode.

One of the fundamental problems is the volumetric expansions and contractions due to Li-ion intercalation during charge-discharge processes, generating considerable internal stresses that affect directly the cycle life and safety [27, 56, 100]. This effect can eventually lead to a formation of micro-cracks, formation of Li-dendrites and other local structural defects at the electrode/electrolyte interface [135-137].

A proposed electro-chemo-mechanical model based on FEM simulation establishes that fracture can be prevented if the electrode-particle´s expansion is lower than 7.5% and the solid electrolyte fracture energy higher than 4 $J \cdot m^{-2}$, assuming a solid electrolyte with Young´s modulus of 15 GPa [100]. Microstructural inhomogeneities within electrode/electrolyte interface; particle misalignments and asperities are critical to enhance local tensile and shear stresses in the solid electrolyte matrix [100]. In such a case, the crack nucleation and propagation becomes more likely for tougher materials with high fracture energy, making the fracture properties of the electrolyte a limiting factor for material´s selection.

Characterizing the Young´s modulus of solid electrolytes is important for solid state batteries, in particular for stress-strain calculations. It is favorable that solid electrolytes deform elastically, in order to maintain the contact between the electrodes during change in volume during charging and discharge; therefore solid electrolytes should have an elastic modulus that is not too high. Even though solid electrolytes with low stiffness were considered to be favorable for the design of bulk-type properties [138], another study shows that solid electrolytes with Young´s modulus in the order of only 15 GPa are more prone to micro-cracking [100].

Moreover, it is expected that the solid electrolyte possess a sufficient mechanical integrity to be handled during processing and withstand clamping forces when fixed between anode and cathode [8], adequate stiffness and mechanical resistance to scratch. Accurate estimates of Young´s modulus and hardness are necessary for fracture toughness and for stress-strain calculations. Appreciation of the mechanical properties also permits the fabrication of thinner electrolyte membranes, i.e. 10-100 μm thick.

2.2.4.1. Dendrite suppression

Short circuiting events have been first reported for Na-ion conducting solid electrolytes in Na batteries and associate with stresses induced by a molten sodium metal plating that resulted in crack propagation and eventual failure [139-141]. Recently, similar issues of short circuiting events have been reported and investigated in more detail for inorganic solid electrolytes combined with a Li metal anode [142-144], see Figure 2.7. On the other hand, thin film batteries using similar systems seem to withstand dendrite formation [145, 146], however, the mechanisms are not fully understood.

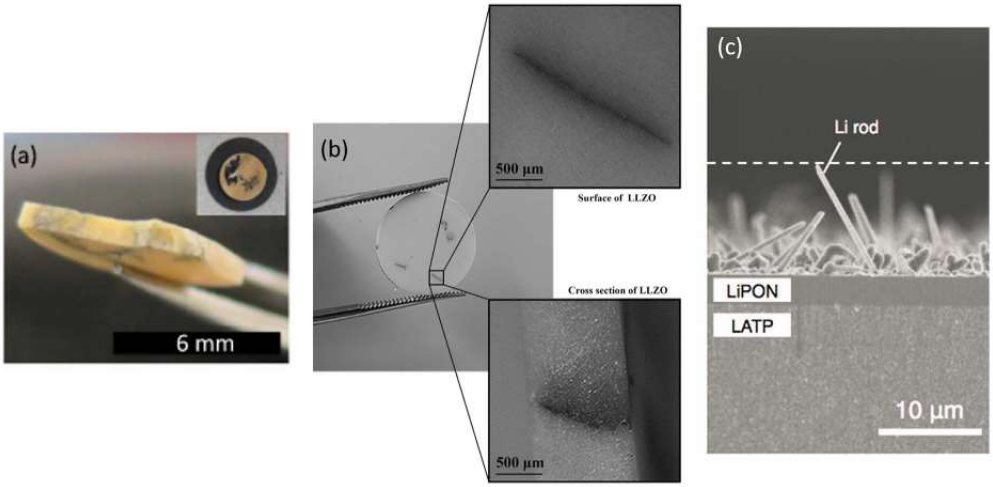

Figure 2.7- Dendrite failure reported in different SSE materials a) Ga-doped LLZO; b) Al-doped LLZO; c) LiPON-Li interface [135].

Monroe and Newman suggested a kinetic model incorporating elastic effects, where the shear modulus of the solid electrolyte should be at least more than twice that of Li metal (4.25 GPa) to avoid Li metal penetration through the electrolyte [96, 147]. In this case, solid electrolytes with minimum shear modulus of ~8.5 GPa would be expected to suppress dendrite initiation. Nevertheless, materials with sufficient stiffness to warrant suppression of dendrite initiation and propagation failed [55, 144], suggesting that this criterion alone is not a sufficient factor.

Recently, Raj and Wolfenstine proposed an analytical model based on previously derived electro-mechanical potentials at interfaces [148, 149], where they combine the interfacial stress and the electrical potential and compared it with the standard potential of lithium to evaluate the nucleation of lithium dendrites at the interface electrolyte/Li metal. According to them, the higher resistantce of grain boundaries or physical irregularities raises the local electrochemical potential of lithium, promoting the Li dendrite nucleation. Since there is no available result on literature, the model assumes a solid electrolyte with fracture stress of 100 MPa, that acts as a back stress opposing to the nucleation, fracture occurring by tensile stresses created by a defect as a pore when the electrolyte is pressed against Li-metal, the normal traction at the interface is compressive, it creates an equal tensile stress in the orthogonal direction, which can cause fracture. Assuming a concentration of current density at the lithium interface of 1 $mA \cdot cm^{-2}$, the dendrite will grow if the interfacial charge resistance is greater than 13.7 $\Omega \cdot cm^2$ [149].

It has been suggested that, minimal defect size on the surface, roughness or inhomogeneities lead to an infiltration of lithium and produces stresses, which eventually drive crack propagation, given that a critical current density is overpassed [40, 139]. Figure 2.8 shows interfacial flaws, either in liquid or solid electrolyte, that are filled with metal and the proposed failure mode that follows Griffith flaws.

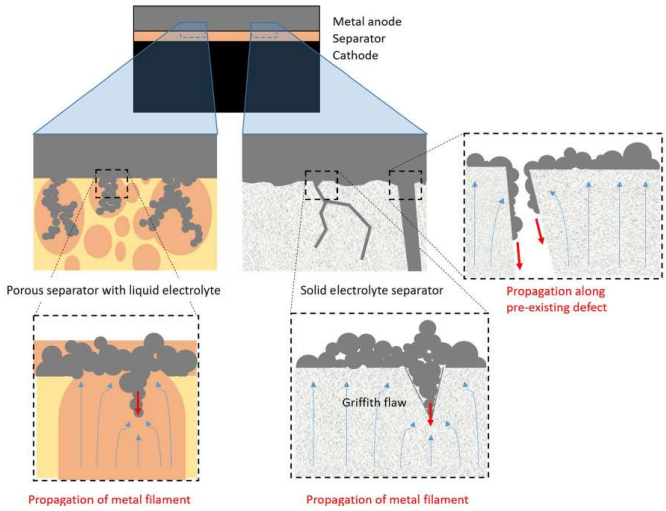

Figure 2.8- Schematic illustration of Li penetration in liquid and solid-state electrolytes, where red arrows represent metallic growth into the bulk of the separator and blue arrows show electric field lines [40].

Another mechanism of lithium metal penetration proposes that due to electric field concentration and low over potential the lithium metal first fill flows into pores and crack on the solid electrolyte surface, then mechanical stresses rise. In that case, employing a plain strain analyses a relation between stress gradient in the x-direction and shear stress is obtained [139]. In experiments, it was noted that the aspect ratio is much higher, ~300 nm, however, the geometry of the Li filament is simplified according to Figure 2.9.

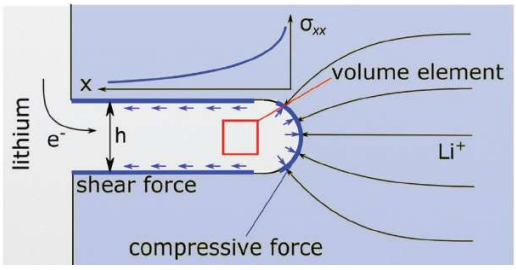

Figure 2.9- Schematic model of Li filament into a solid electrolyte, arrows at the rounded end represents the applied pressure and along the sides show shear traction due to friction [139].

This model predicts that the maximal stress will occur at the filament and decay along its length and the failure mode prevailing is Griffith-like. Considering an uniform stress inside the filament and a linear elastic fracture mechanism, the criteria for crack extension is given by [139]:

$$\sigma \geq \frac{K_{IC}}{\gamma \sqrt{\pi \alpha}} \qquad \text{Eq. 15}$$

where σ is the internal stresses, K_{IC} the fracture toughness of the solid electrolyte, γ a geometry factor of the surface crack shape being 1.12 for a half-penny shape surface crack, and α is the defect size. Considering that internal stresses are equal to the maximum hydrostatic stress, which was established previously, a correlation of a minimum over potential as function of flaw size is established. Experimental measurements and model suggest that above a critical current density of 1-5 $mA \cdot cm^{-2}$ (1 mA ~ 0.4 V) mechanical stresses due to the Li overpotential will lead to an extension of surfaces defects [139].

In summary, a critical current density and high contact resistance at the interface electrolyte/anode are key requirements to avoid formation of dendrites. Additionally, grain boundary effects, microstructure, density and interface should be considered [144, 150]. In order to address these issues, microstructural and interfacial modifications are being implemented to improve the contact between electrolyte/electrode and reduce the interfacial resistance. For instance, liquid interfacial layer or surface coating to increase wettability [55, 144, 151, 152], increasing contact area and reduce surface defects [139, 153] and removing surface contamination by $LiOH/Li_2CO_3$ [154, 155].

2.2.4.2. Mechanical properties of $Li_7La_3Zr_3O_{12}$ (LLZO)

Table 2.3 compiles the mechanical properties of LLZO collected from literature, revealing a range of values for the mechanical properties, in particular the fracture toughness that varies with relative density, grain size and testing method.

Table 2.3 - Mechanical properties of garnet-structured LLZO solid electrolytes.

Compound	Processing method	Grain size (µm)	Testing Method	Elastic Modulus (GPa)	Hardness (GPa)	Vickers K_{IC} (MPa√m)
$Li_{6.24}La_3Zr_2Al_{0.24}O_{11.98}$ [15]	Hot pressed 1000 °C/40MPa/1h Porosity = 0.03	4.5 - 5.0	Resonant ultrasound Spectroscopy	149.8 ± 0.4	6.3 ± 0.3 (V 2.9 N) 6.2 ±0.3 (V 4.9 N)	-
	Hot pressed 1000 °C/40MPa/1h Porosity = 0.06	4.5 - 5.0	Resonant ultrasound Spectroscopy	132.6 ± 0.2	6.3 ± 0.4 (V 2.9 N) 5.2 ± 0.4 (V 4.9 N)	-
$Li_{6.17}Al_{0.28}La_3Zr_2O_3$ [13]	Hot pressed 1100 °C/8KN/1h Rel. Density > 98%	5 - 50	DFT (0 K) DFT (298K) Impulse excitation Dynamic indentation	162.6 154.5 146.1 ± 0.8 150.3 ± 2.2		-
$Li_{6.5}La_3Zr_{1.5}Ta_{0.5}O_{12}$ [13]	Hot pressed 1100 °C/8KN/1h Rel. Density > 98%	1 - 10	DFT (0 K) DFT (298K) Impulse excitation Dynamic indentation	154.9 147.2 139.9 ± 2.1 153.8 ± 2.7		-
$Li_{6.19}Al_{0.27}La_3Zr_2O_{12}$ [156]	Hot pressed 1050 °C/62MPa/30min Rel. Density 85 ± 1%	2.7 ± 1.7	Nanoindentation	~ 135 GPa	4.7 ± 0.2 (V ~ 0.3 N) 8.1 ± 0.8 (B~ 125 µN)	~ 2.37 ± 0.1
	Hot pressed 1050 °C/62MPa/60min Rel. Density 95 ± 1%	3.2 ± 1.9	-	-	7.4 ± 0.4 (V ~ 0.3 N) 9.3 ± 0.5 (B ~ 125 µN)	~ 1.3
	Hot pressed 1050 °C/62MPa/90min Rel. Density 96 ± 1%	3.5 ± 1.8	-	-	~ 8.8 (V ~ 0.3N) ~ 9.1 (B~ 125 µN)	~ 1.11
	Hot pressed 1050 °C/62MPa/240min Rel. Density 98 ± 1%	3.7 ± 1.8	Nanoindentation	~ 140 GPa	~ 9.1 (V ~ 0.3N) ~ 9.1 (B~ 125 µN)	0.97 ± 0.1
$Li_{6.24}La_3Zr_2Al_{0.24}O_{11.98}$ [14]	Hot pressed 1000 °C/40MPa/1h Rel. Density 97%	~ 5	-	-	-	0.86 - 1.63

V= Vickers indenter, B= Berkovich indenter.

The first report on the mechanical properties of cubic LLZO garnet materials was published in 2012 by Ni *et al* [15], where elastic modulus (*E*), bulk modulus (*B*), shear modulus (*G*) and Poisson's ratio (*v*) were evaluated by ultrasound spectroscopy and hardness via Vickers indentation testing; values for the former four parameters were found to be ~ 150 GPa, 100 GPa, 59 GPa and 0.26, respectively. Fracture toughness values of hot pressed cubic $Li_{6.24}La_3Zr_2Al_{0.24}O_{11.98}$ with relative density of 97% have been derived by Wolfenstein et al. [14] using indentation testing; values ranged from 0.86 to 1.63 MPa√m with predominantly transgranular crack path and the crack analyses suggested that both half-penny and Palmqvist cracks were present.

Another study compared experimental elastic moduli from nanoindentation to those calculated using DFT [13]. Al-doped LLZO with composition $Li_{6.17}Al_{0.28}La_3Zr_2O_3$ and Ta-doped with composition $Li_{6.5}La_3Zr_{1.5}Ta_{0.5}O_{12}$ were investigated and the theoretical prediction indicated that Ta-doped material should have a lower elastic modulus compared to Al-doped LLZO, being in agreement with lattice constant values, since theory and experiment revealed that Al-doped material has a slightly larger lattice parameter. Small differences in measured values, shown in Figure 2.10, were attributed by authors to experimental error. The micrographs of the fractured surface reveals a grain size of specimen of 5-50 µm, and 1-10 µm for the Ta-doped specimen (Figure 2.10 a and b).

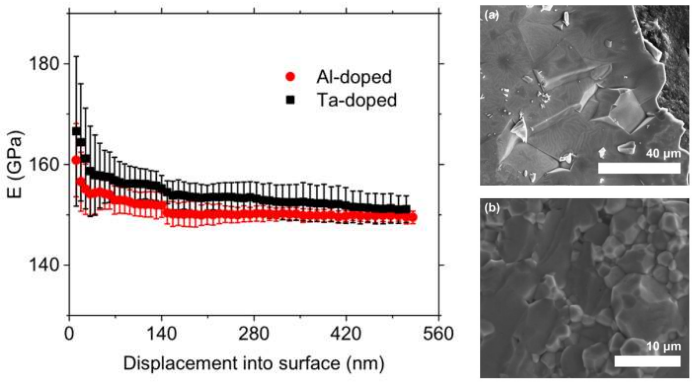

Figure 2.10- Measured elastic modulus of Al- and Ta-doped LLZO and respective fracture surfaces a) Al-doped and b)Ta-doped material [13].

Recently, it was found that the relative density has a strong effect on mechanical properties of LLZO [156]. Samples with grain sizes from 2.7-3.7 and densities of 85-98% showed a transition from intergranular to transgranular fracture mode probably related to the relative density. The crack propagation mode was associated with the crack deflection along grain boundaries that could explain an observed increased fracture toughness with decreasing relative density (see Figure 2.11). An interesting conclusion of this work is that with increased relative density the conductivity is also improved and, however, going along with a sacrifice in K_{IC}.

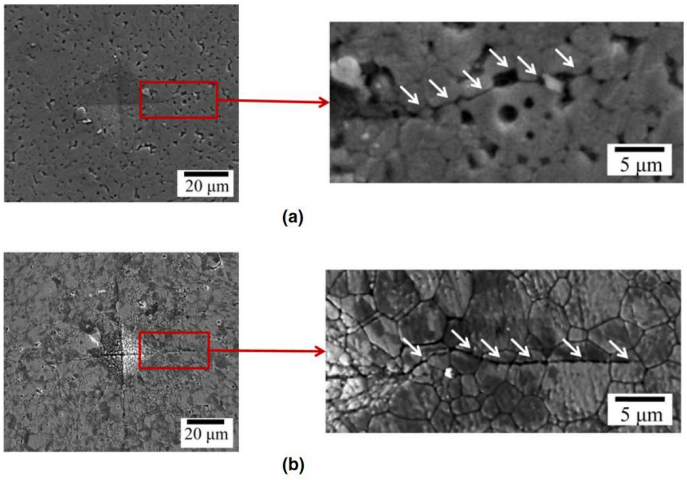

Figure 2.11- Crack propagation trajectories for LLZO with a) 85% relative density and b) 98% relative density [156].

An important aspect regarding mechanical properties is the consideration and, hence, determination of values for single crystal and polycrystalline material and understanding the influence of grain boundaries onto fracture toughness, elastic modulus and hardness. Sharafi *et al*. [157] found that hardness decreased from 9.9 to 6.8 GPa as the average grain size increased from 5 µm to 600 µm, and therefore LLZO single crystal hardness can be represented by a value of 6.8 GPa. The fracture toughness was grain sizes invariant for sizes greater than 40 µm with values of

~ 0.6 MPa·m$^{1/2}$ and a higher toughness of 0.87 ± 0.07 MPa·m$^{1/2}$ was obtained for the smallest average grain size (~5 µm), which was associated with crack deflection along grain boundaries.

To fully understand the role of grain boundaries onto the mechanical properties, especial onto fracture toughness, more studies have to be carried out. Hence, one of the aims of the current work is to investigate the effect of grain boundaries onto fracture toughness as well as an assessment of the intrinsic properties of single grains using advanced micro-mechanical testing.

3. Experimental

Within the framework of this study, $Li_7La_3Zr_2O_{12}$ samples with different dopants, porosities and microstructures were produced at IEK-1, Forschungszentrum Jülich GmbH, partially by the present author and partially by collaborating scientists. Pellets were produced via different synthesis methods and subsequently characterized with indentation tests to derive elastic, plastic behavior and fracture toughness based on indentation and micro-pillar testing. Three aspects of the $Li_7La_3Zr_2O_{12}$ are considered in three separate sub-chapters, first the effect of doping on the mechanical and electrical properties in order to find an optimum composition, and further porosity effect. Second, optimization of the characterization methodology to assess the fracture toughness via combination of indentation testing and micro-pillar, third, determination of the properties for a dense composition to assess differences with respect to the first section in order to clarify the aspects related to porosity and grain size and compositional variation.

3.1. Materials synthesis

3.1.1. Cold pressed

Unsubstituted, Al- and Ta- $Li_7La_3Zr_2O_{12}$ (LLZ)

Unsubstituted lithium lanthanum zirconate $Li_7La_3Zr_2O_{12}$ (LLZ), Al-substituted LLZ (Al-LLZ) $Li_{7-3x}Al_xLa_3Zr_2O_{12}$ ($x = 0.2, 0.36$) and Ta-substituted LLZ (Ta-LLZ) $Li_{7-y}La_3Zr_{2-y}Ta_yO_{12}$ ($y = 0.2, 0.40, 0.60$) powders were synthesized via a three step solid-state reaction in argon atmosphere. They were prepared from $LiOH \cdot H_2O$ (98%; Merck), La_2O_3 (99.9%, dried at 900 °C, 10 h; Merck), ZrO_2 (99.5%, Treibacher), Al_2O_3 (99.9%, Inframat) and Ta_2O_5 (99.5%, Inframat). The educts were mixed in stoichiometric amounts with an excess of 15% of $LiOH \cdot H_2O$ to compensate the lithium loss during the calcination processes. They were homogenized by grinding in a mortar (Retsch RM 200) for 1 h and pressed with uniaxial press into pellets of ~10 mm. A subsequent calcination at 850°C for 20 h in argon was done using graphite crucibles to avoid additional aluminum uptake. Two more cycles of grinding, pellet pressing and calcination at 1000°C for 20 h in argon were done. After calcination the LLZ pellets were transferred immediately into an argon glove box and again ground into a fine powder. The relative density was quantified from the ratio between the

specimen density via Archimedes' principle and theoretical density via JCPDS-ICDD database. Table 3.1 compiles different substitution levels, sintering conditions and relative densities of investigated materials.

Table 3.1- Substitution, sintering conditions and relative density of investigated materials.

Substitution [mol%]	Sintering Atm./Temp. [ºC] / Dwell time [h]	Relative Density [%]
Un-substituted		
LLZ	Ar/1150/10	77
Al-substituted		
20Al:LLZ	Ar/1150/10	90
20Al:LLZ	Ar/1200/20	90
20Al:LLZ	Air/1200/20	93
36Al:LLZ	Ar/1150/10	90
Ta-substituted		
20Ta:LLZ	Ar/1150/20	92
40Ta:LLZ	Ar/1150/10	91
60Ta:LLZ	Ar/1150/10	98

In order to permit a systematical investigation of effect of the porosity on the mechanical properties, the dwell time during sintering, which directly affects the porosity, was varied. The powder processing procedure and calcination steps of Ta-substituted LLZ $Li_{6.6}La_3Zr_{1.6}Ta_{0.4}O_{12}$ (40Ta:LLZ) were the same as described above. Pellets were pressed using a uniaxial pressing machine (Paul-Otto Weber) with metallic die under a force of 10 KN. The sintering was conducted at 1175°C in an Air atmosphere for different dwell times of 4, 8 and 16 hours (40Ta:LLZ-4h, 40Ta:LLZ-8h, 40Ta:LLZ-16h), respectively. The heating rate was 5 $K \cdot min^{-1}$ and the samples freely cooled to room temperature. Details can be found in Table 3.2.

Table 3.2- List of samples and associated features.

Abbr.	Sint. Atm./Temp. [ºC] / Dwell time [h]	Rel. Density [%]
40Ta:LLZ-4h	Air/1175/4	86
40Ta:LLZ-8h	Air/1175/8	90
40Ta:LLZ-16h	Air/1175/16	93

Al-$Li_7La_3Zr_2O_{12}$ (LLZ)

Similarly as described above, three steps of solid-state reactions were employed to synthesize Al-substitute $Li_7La_3Zr_2O_{12}$ (Al:LLZO) with 20 mol% of Al. A total 50 g batches of La_2O_3 (99.9%, dried at 900 °C, 10 h; Merck), ZrO_2 (99.5%, Treibacher), Al_2O_3 (99.9%, Inframat), Ta_2O_5 (99.5%, Inframat) and 15% stoichiometric excess of $LiOH{\cdot}H_2O$ (98%; Merck) to compensate the Li loss during calcination were mixed via an automatic mortar (Retch RM200) for 1 h to achieve a homogenous mixture; afterward, the mixture was uniaxially pressed into pellets. A subsequent calcination was carried out at 850 °C for 20 h, and the pellets were then immediately transferred to an argon glove box and ground to a fine powder. The grinding, pellets pressing and calcination processes were repeated for another two cycles with heating to an elevated temperature of 1000 °C for 20 h. After the calcination steps, pellets were pressed using a 13 mm die and a pressure of 150 MPa. Subsequent sintering was done at 1200 °C in air for 20 h to completely densify the specimens for mechanical properties investigation.

3.1.2. Hot pressed

Hot pressing (HP) is a high pressure shaping method, that by simultaneous application of heat and pressure induces powder compaction and sintering. In this section, dense Al-doped and Al-free $Li_{6.6}La_3Zr_{1.6}Ta_{0.4}O_{12}$ (HP-LLZ:Ta and HP-Al free:LLZO) powders were synthesized by IEK-1 via solid-state synthesis (SS) and solution-assisted solid-state synthesis (SASSR), in order to form samples with larger (LG) and small grains (SG) for intrinsic improvement of the solid electrolytes in terms of conductivity, cycle stability and mechanical properties.

Conventional solid-state synthesis (SS)

Al-free and 5 mol% Al-doped $Li_{6.6}La_3Zr_{1.6}Ta_{0.4}O_{12}$ were synthesized by conventional solid-state synthesis. The corresponding stoichiometric amounts of $LiOH.H_2O$ (with a 20 mol% excess for the compensation of lithium losses in calcining and sintering steps), lanthanum (III) oxide La_2O_3 (99.9%, dried at 900 ° C for 10 h and then hermetically sealed before the Merck, Germany), zirconium (IV) oxide ZrO_2 (99.5%, Treibacher, Germany), tantalum (V) oxide Ta_2O_5 (99.5%, Inframat Corp., USA), and 5 mol% aluminum (III) oxide Al_2O_3 (99.9%, Inframat Corp., USA) were weighed and mixed in a mortar mill (Retsch RM 200) for 30 minutes. Subsequently, the

reacted mixture was pressed into pellets and annealed in an Al_2O_3 crucible at 850 °C for 20 hours (heating and cooling rate 5 K/min). After the thermal treatment, the pellets were ground in a mortar mill for 30 minutes, pressed into pellets and calcined in an Al_2O_3 crucible at 1000 °C for 20 hours (heating and cooling rate 5 K/min). Calcined pellets were ground again and mechanically mortared. The prepared calcined powder was pre-shaped as pellet at 100 MPa and pressure densified at 50 MPa and 1150 °C for 5 hours.

Solution-assisted solid-state synthesis (SASSR)

The same compositions described before for conventional synthesis, Al-free and 5 mol% Al-doped $Li_{6.6}La_3Zr_{1.6}Ta_{0.4}O_{12}$ precursor powder was synthesized by the solution-assisted solid-state synthesis method. Lithium nitrate $LiNO_3$ (with a 20 mol% excess, 99%, anhydrous, Alfa Aeser, USA), zirconyl nitrate hexahydrate $ZrO(NO_3)_2 .6H_2O$ (99%; Sigma-Aldrich, USA) and lanthanum (III) nitrate hexahydrate $La(NO_3)_3$ x $6H_2O$ (99.9%; Alfa Aeser, USA) were dissolved in distilled water (~200 ml); Tantalum (V) ethanolate $C_{10}H_{25}O_5Ta$ (99.9%, Strem Chemicals, USA) was added dropwise to the metal salt solution slowly with stirring on a magnetic stirrer. The reaction mixture was dried and calcined at 300 °C and 400 °C to burn out the organic residues. The prepared calcined powder was pre-shaped as pellet at 100 MPa and pressure densified at 50 MPa and 1077 °C for 3 hours.

Table 3.3 - Description of hot pressed specimens.

Specimen	Synthesis method	Density (%)
HP-Al:LLZO-LG	SS	99.9
HP-Al:LLZO-SG	SASSR	99.1
HP-Al free:LLZO-LG	SS	99.8
HP-Al free:LLZO-SG	SASSR	99.5

3.2. Microstructural characterization

3.2.1. X-Ray diffractometry

The LLZO structural analysis and phase characterization was done by X-ray diffraction (XRD) with a Bruker D4 Endeavour spectrometer equipped with a 1D detector LYNXEY and a

DIFFRAC^{plus} BASIC package 2009 using Cu-K_α radiation. The synthesized LLZO powders were analyzed at room temperature in a 2θ range of 10° to 130° with a $\Delta_{2\theta} = 0.02°$ and 2 s per step. The lattice parameters were determined via Rietveld refinement using the profile analysis software TOPAS (Version 4.2, Bruker AXS GmbH, Karlsruhe Germany) and the crystal structures were extracted from the Inorganic Structure Database (ICSD, FIZ Karlsruhe, Germany). Tetragonal and cubic proportions below 10% by weight are not detectable, therefore cannot be presented, as well as small amounts of secondary phases that are below the detection limit of XRD. Cubic and tetragonal LLZO phases were identified with respect to JCPDS files no. 99-000-0032 and 99-000-0020. Porous density (1-*x*%) quantified from the ratio (*x*%) between the specimen density via Archimedes' principle and theoretical density via JCPDS database.

High temperature X-ray diffraction was used to investigate lattice parameter, phase stability and transformation during heating and cooling. The diffractometer PANalytical EMPYREAN was equipped with heating chamber Anton Paar HTK-1200N; tests were performed under vacuum (10^{-5} mbar) and in air, 2θ range of 5° to 100° with a $\Delta_{2\theta} = 0.0137°$, 0.4 and 0.8s per step and temperature range from 25 to 1000°C with heating and cooling rates of 2 K/min.

3.2.2. Inductively coupled plasma optical emission spectrometry

The sintered specimens were characterized with respect to their stoichiometry concentration via inductively coupled plasma optical emission spectrometry (ICP-OES). ICP-OES tests were conducted at IEK-1 and by Zentralinstitut für Engineering, Elektronik und Analytik (ZEA-3) (Thermo Elemental, IRIS Intrepid). LLZO powder was dissolved in HCl solution and injected through plasma, the weight percentage of each element in the sample was measured by emission spectrometer subsequent to an emission of light with certain frequency. The detection limit for ICP-OES was 0.01 wt% as characterized via testing of 26 standard elements before analysis.

3.2.3. Electrochemical impedance spectroscopy

The conductivity measurements were performed by IEK-1 (Forschungszentrum Jülich) by means of the **E**lectrochemical **I**mpedance **S**pectroscopy (EIS). An “Alpha A High Performance Frequency Analyzer” (Novocontrol Technologies, furnace included) was used to measure the conductivity of pellets from each LLZ composition between 300 K and 650 K in steps of 50 K in

a frequency range from 1 Hz to 20 MHz with an electrical field perturbation of 20 $mV \cdot mm^{-1}$. For this test, the top and bottom of the cylindrical pellets were polished with 250, 400, 800 and 1200 grid sandpapers to remove any contamination and to flatten the surface. As blocking electrodes, thin Au layers were sputtered on both sides, providing a good contact to the LLZ. Silver paste was then painted onto the Au electrodes and annealed at 600°C for 30 min to provide a stable contact to the impedance system. Impedance plots were determined by means of the electrochemical impedance spectroscopy and the conductivity was derived from Nyqvist plots. For simplicity and relevance reasons, impedance plots and conductivities only at the room temperature are reported.

3.2.4. Metallographic preparation

Before SEM and indentation testing, the specimens were embedded in an water-free epoxy resin (Buehler Epoxy 2000, solidified at room temperature for 48h), ground sequentially with silicon carbide abrasive paper from #400 to #4000 and gradually automatic polished (Buehler Minimet 1000) using cloth polishing and 3 µm and 1 µm diamond powders, respectively, in water-free oil and subsequentially, as final step, polished using 0.2 µm SiC in water-free Polyethylene Glycol (PEG) polishing suspension.

3.2.5. Scanning electron microscope and electron backscatter diffraction

The microstructures and topographies of the specimens were investigated by a field emission scanning electron microscope (SEM) (FESEM; Zeiss Merlin) on polished cross section. Just before the observation, the samples were polished to obtain a clean cross-sectional surface and remove any moisture associated degradation. The grain size was estimated using the software AnalySIS Pro based on the circular intercept segment mode of several SEM images. The orientation of single grains was obtained by electron backscatter diffraction (EBSD). For EBSD analyses, and accelerate voltage of 10 kV and step size of 2.24 µm was used to construct the EBSD map.

3.2.6. Focused ion beam

The preparation of micro-pillar for fracture toughness evaluation was performed by focused ion beam (FIB) which allows the preparation of micro-pillar with different diameter, 5 and 10 µm, and the ratio height/diameter was 1 for both cases. A FIB dual ion beam scanning electron microscope

(FIB-SEMs; Zeiss Auriga) operated at 30 kV and 2 - 16 nA was used to prepare the micro-pillars. The fundamental functionality is similar to scanning electron microscope, however, gallium ions are generated by a field emission with tungsten needle which heated up the gallium until its melting point.

3.3. Mechanical characterization

3.3.1. Depth-sensitive indentation test

Depth-sensitive indentation testing was carried out by a nano-/micro-indenter system (CSM; Anton Paar) with a Berkovich tip that was inhoused in a vacuum chamber (< 1 ppm O_2, < 1 ppm H_2O), hence, permitting the control of the atmospheric boundary conditions to prevent degradation due to moisture [158, 159]; the system possessed a high-resolution microscope (50x magnification, CF IC EPI Plan ELWD, Nikon).

Elastic modulus (*E*) and hardness (*H*) were assessed on the basis of the widely used Oliver-Pharr procedure [105]. They were recorded by applying continuous multi-cycle measurements (CMCs), where 20 cycles with increasing load were implemented with quadratic loading and unloading to 5% of the maximum load in each given cycle. CMCs were performed to permit a calculation of average mechanical properties and the standard deviation was derived at each corresponding indentation depth. Advantages and disadvantages of the CMC method are discussed in [160, 161]. The load range, acquisition rate, holding time intervals and pause time corresponded to 5 mN to 500 mN, 10.0 Hz, 2 s and 1 s, respectively. The determination of elastic modulus was based using a Poisson's ratio of 0.24 for Al:LLZO and 0.26 for Ta:LLZ [13].

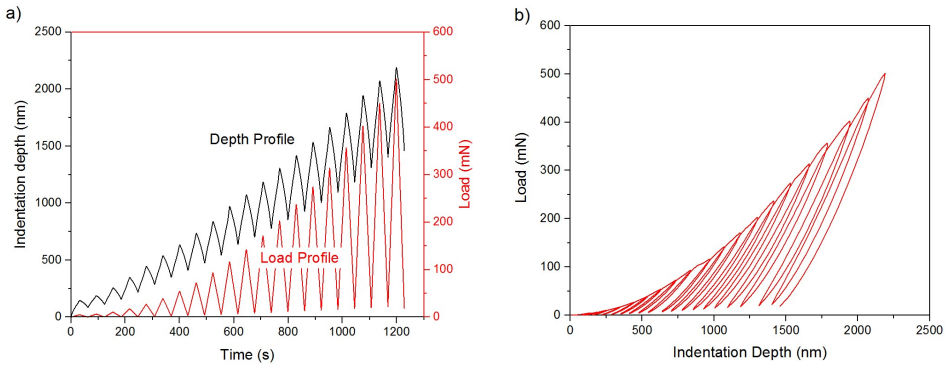

Figure 3.1- a) Typical load- and depth-time profile of LLZ and b) indentation load versus indentation depth

Complimentary standard indentation was performed with different loads and different loading rates on few selected samples. For each test a matrix of 5×4 was done with a proper distance separation between the indentions, 5 times the indentation diameter. Maximum loads of 5 mN, 100 mN, 200 mN, 300 mN, 400 mN and 500 mN were implemented, with linear loading, holding period was fixed to be 1s, loading and unloading times of 30 s were used.

For the hot-pressed samples a newly acquired nano-indenter NanoTest Xtreme (Micro Materials) was employed to measure elastic modulus and hardness. A matrix of 5×5 indentations was done load-control in continuous multi-cycling mode, minimum load was 5 mN and maximum load 50 mN, 20 cycles of loading-unloading were performed with holding time of 2s in order to focus on the effective properties only.

3.3.2. Indenation fracture toughness

Fracture toughness values were derived on the basis of the conventional Vickers indentation method (VIF) [114] to evaluate global and local fracture performance indicators, respectively. Crack lengths induced by the Vickers indentation imprint were measured immediately after the indentation process to avoid subcritical crack growth effects. Moisture associated degradation was only considered to be a minor effect due to the test under vacuum conditions (10 mbar) [158, 159]. Based on the crack length (l)-to-indent impring half-diagonal (a) ratio ($0.25 \leq l/a \leq 2.5$), as characterized from SEM images of cracks and complimentary crack shape analyses through cross-sectional images carried out by FIB, the following fracture toughness formula for Palmqvist cracks was selected for the calculation [120]:

$$K_{Ic} = 0.079 \frac{P}{a^{3/2}} log\left(4.5 \frac{a}{l+a}\right) \qquad \text{Eq. 16}$$

Up to ten indentations for loads of 1 N, 3 N and 5 N were applied to induce cracks with sufficient crack length for toughness calculation. An microindenter Fischer HC100 and a macroindenter Buehler Met 10 were used to introduce the impressions. For all samples, similar range of loads were selected based on the materials behavior during the tests. The fracture toughness equation based on Niihara approach for Palmqvist cracks was selected where apropriate for the calculation,

the equation can be found in Table 2.2.

3.3.3. Micro-pillar splitting test

The micro-pillar indentation splitting test utilizes a Berkovich indenter [125, 133] to evaluate the local fracture toughness (details see section 2.2.3.2). A FIB dual ion beam scanning electron microscope (FIB-SEMs; Zeiss Auriga) operated at 30 kV and 2 - 16 nA was used to prepare the micro-pillars, and the location and cross-sectional images of an as-prepared micro-pillars are illustrated in Fig. 1 (a) and (b), respectively. The fracture toughness was calculated using equation 14 from section 2.2.3.2 [125] and the dimensionless coefficient β was estimated from $\beta = 0.057 + 0.0149\frac{E}{H}$ [125, 128]. For Al-doped LLZO the elastic modulus to hardness ratio yielded β= 0.31 and the average pillar radius 5.1 ± 0.1 µm.

The pillar's aspect ratio (height-to-diameter) was fixed to 1 for all samples to relax any possible residual stress [110, 125]. The method was only illustrated for selected material to permit derive properties of individual grains and permit conclusions on the validity of the conventional VIF method. For Al-doped LLZO all pillars were made within an individual grain to acquire data on the intrinsic fracture toughness, avoiding effects of grain boundaries. A nano-indenter system (CSM; Anton Paar) with a Berkovich tip was used, the load-displacement curves were recorded during the load-controlled indentation (monotonously increased from 0 to 50 mN with a loading rate of 1.67 mN/sec) to permit observation of the pop-in event associated with the pillar splitting. Figure 3.2 shows SEM topographies of Al-doped LLZO.

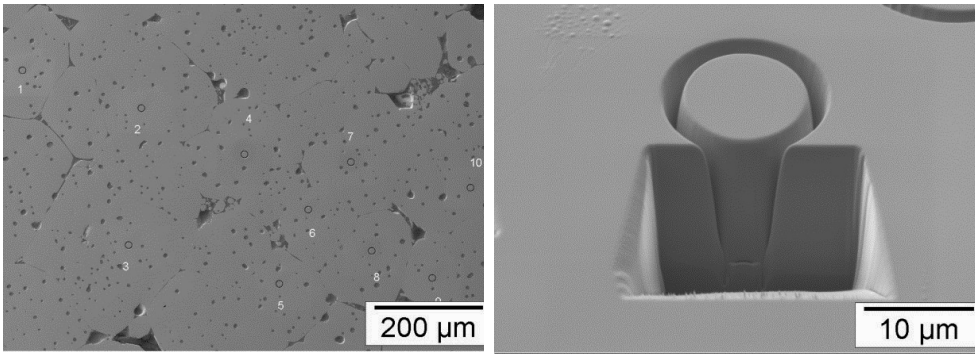

a) b)

Figure 3.2 SEM topographies: a) specimen surface and the selected areas for micro-pillar testing. B) micro-pillar on single grain of Al-doped LLZO.

For hot pressed LLZO the same FIB station and similar parameters were used to fabricate the micro-pillars on samples with small and larger grains sizes; pillar radius varied from ~2.5 to ~5.3 µm in order to investigate the size effect. Figure 3.3 and Figure 3.4 show the FIB fabricated micro-pillar on HP-Al:LLZO-LG and HP-Al:LLZO-SG, respectively. These samples were tested with the recent acquired NanoTest Xtreme (Micro Materials) which became available during the cause of the project; the loading rate of 10 mN/sec was used up to the maximum load of 50 mN for pillar with radius ~5.3 µm and 20 to 25 mN for pillar with radius ~2.5 µm. Table 3.4 compiles the tested samples and relevant features. The elastic modulus and hardness ratio yielded to $\beta = 0.27$, more details can be found in results, section 4.3.2.2.

Table 3.4- Summary of tested samples by micro-pillar splitting test.

Tested Samples	Number of pillars tested	Diameter [µm]	Description/ Grain size [µm]
Al:LLZO	5	10	Single crystal ~ 100
HP-Al:LLZO-LG	5 5	10 5	Single crystal ~ 10
HP-Al:LLZO-SG	5 5	10 5	Polycrystalline ~ 3

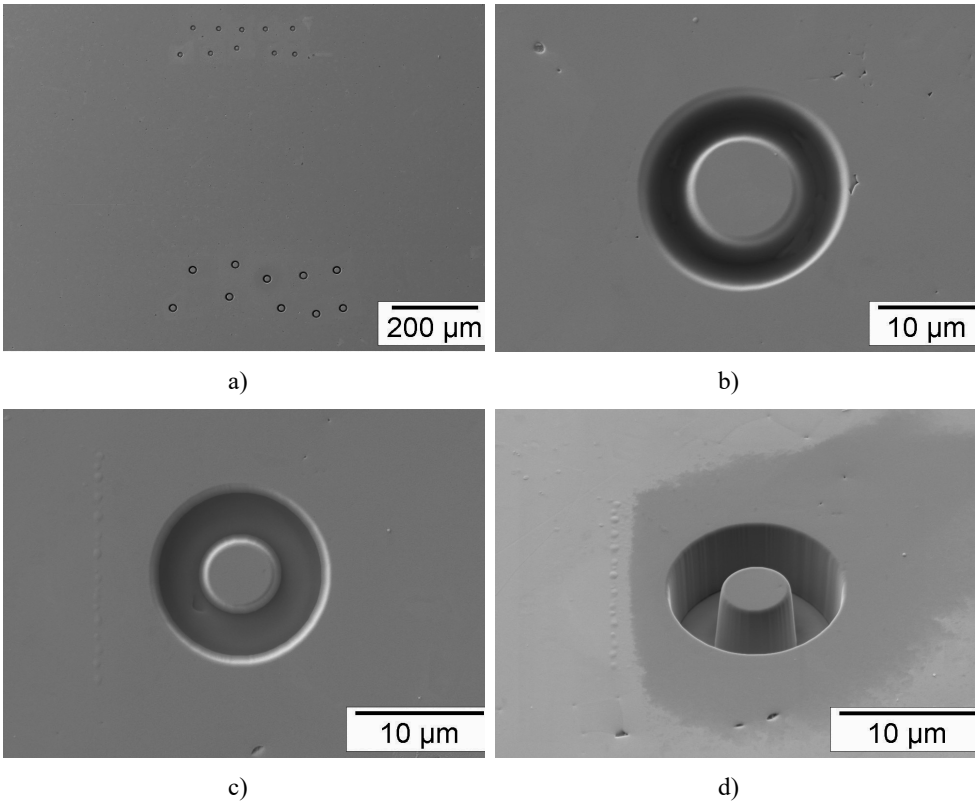

Figure 3.3- SEM topography of hot pressed LLZO- larger grains HP-Al:LLZO-LG a) specimen surface and the selected areas for micro-pillar testing with 10 and 5 µm diameter, b) typical micro-pillar of 10 µm diameter, c) and d) micro-pillar of 5 µm diameter.

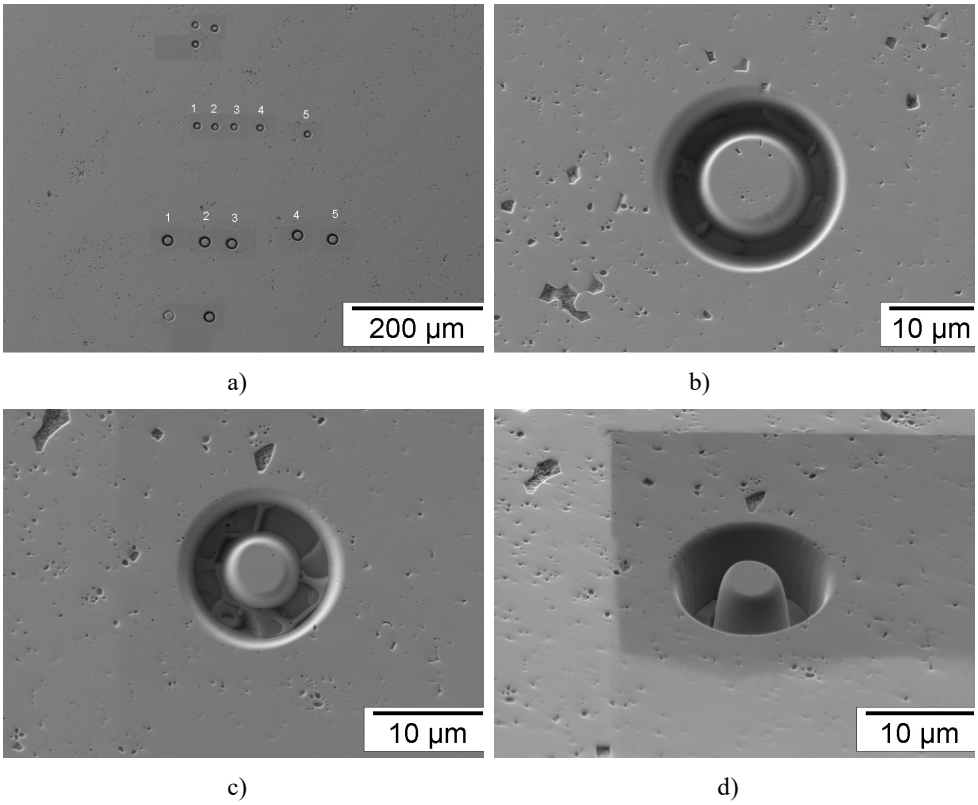

Figure 3.4- SEM topography of hot pressed LLZO- small grains HP-Al:LLZO-SG a) specimen surface and the selected areas for micro-pillar testing with 10 and 5 µm diameter, b) typical micro-pillar of 10 µm diameter, c) and d) micro-pillar of 5 µm diameter.

The new NanoTest Xtreme (Micro Materials) system allowed a more accurate positioning of the indenter above the pillars due to the 3D profiler/nano-positioning stage. The nano-positioning system was used for imaging the sample surface before and after test, and allowed indent placement with nm resolution while providing 3D imaging of the sample surface. The scanning steps used during experiment varied from 0.1 to 0.5 µm. 3D scan images can be seen in Figure 3.5.

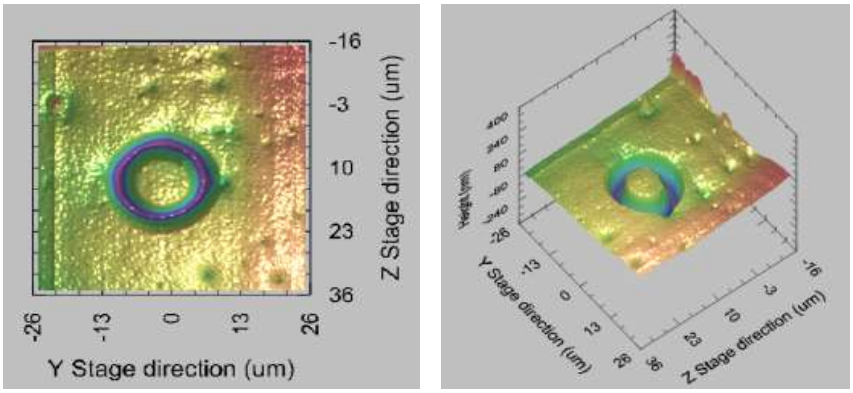

a) b)

Figure 3.5- Scanned surface of HP-Al:LLZO-SG before testing a) plan view; b) 3D view of micro-pillar.

4. Results and discussion

The results that are presented and discussed in the following concentrate on three aspects of $Li_7La_3Zr_2O_{12}$ that are considered in three separate chapters. First, results are presented on uniaxial pressed $Li_7La_3Zr_2O_{12}$ (LLZ) as investigated in its pure, tetragonal phase and its stabilized cubic phase, which is realized by substitution of different amounts of Ta and Al. The effect of substitution and sintering conditions on phase composition, microstructure, electrical properties and, as main focus, elastic modulus and hardness are investigated. Complementary mechanical characterization focused on porosity effects and moisture related degradation.

Second aspect considered in a separate chapter is the optimization of the characterization methodology to assess the fracture toughness via combination of indentation testing and micro-pillar indentation splitting test. Due to the complexity of the analysis and methodological improvement the section concentrates on one materials composition as representative example. Hence, results are presented on uniaxial pressed Al-substituted $Li_7La_3Zr_2O_{12}$ (Al:LLZO) being mechanically characterized and microstructural features are correlated. A novel method based on micro-pillar indentation splitting is applied to assess the microscopic fracture toughness within individual Al-doped LLZO grains and the outcome is compared with data derived from the conventional VIF method as measure of the macroscopic fracture toughness.

In the third part, results of hot pressed Ta-substituted $Li_7La_3Zr_2O_{12}$ Al-doped and Al-free with larger and nano-particles sizes, as synthesized via solid-state synthesis and solution-assisted solid-state synthesis, are investigated. Aim is here to clarify the aspects related to density, grain size and compositional variation. Hence, effects of doping, microstructure, surface properties and density are correlated with elastic modulus, hardness and fracture toughness, especially, the grain size dependence. Fracture toughness is investigated via the conventional VIF method and complementary, novel micro-pillar splitting test for different pillar sizes, in order to also justify and clarify potential aspects related to pillar sizes.

Overall, the aims were materials characterization and correlation with microstructural features as well as dopant amounts, which included also refinement and implementation of advanced testing methodologies and methods, which are illustrated for individual compositions. The clarification

of procedures to determine elastic modulus and hardness as well as advancement of the fracture toughness testing will obviously aid the characterization of degradation and operational related effects which, however, could not be tested during the time of the thesis since operated materials could not be made available by the project partner.

4.1. Substitution effect of $Li_7La_3Zr_2O_{12}$

In this chapter, results are presented on the investigation of garnet structured $Li_7La_3Zr_2O_{12}$ in its pure, tetragonal phase and its stabilized cubic phase which is realized by substitution of different amounts of Ta and Al. Hence, effects of substitution and sintering conditions on phase composition, microstructure, electrical properties and, as main focus, the mechanical properties are investigated. Sintering is carried out in air and argon atmosphere at temperatures of 1150 and 1200 °C. The Ta substitution ranges up to 60% and the Al substitution up to 36% to obtain fully cubic samples. The mechanical properties were assessed via depth-sensitive indentation testing and the resulting variations (e.g. microstructure and porosity) were taken into account when drawing conclusions from experimental results and derived values represent either the pure materials properties (e.g. close to single crystal values) or the effective ones, respective of microstructural effects. Preparation of the samples and conductivity measurements were carried out by partners at IEK-1 and the results presented in this chapter are already partially published in [162].

4.1.1. Conductivity, phase composition and microstructure

Table 4.1 gives a compilation of relative density, grain size, and ionic conductivity at room temperature and ICP-OES results for the different elements of the materials variations in terms of substitution tested in the current study. It is obvious that the substitution (and density) has a strong impact on the total Li-ion conductivity, with Ta outperforming most of the Al substitution based compositions and both being approx. 4 orders of magnitude better than un-substituted LLZ, which agrees well with results given in the available literature [163, 164]. Also in agreement with literature reports, the change of sintering atmosphere from air to Ar has only a minor effect on the total Li-ion conductivity [165]. However, to correctly correlate fundamental materials property to

effects of the specific processing conditions and thus the apparent quality of our samples, in addition the interrelated effect of the relative density of the samples has to be considered.

Table 4.1- Substitution, sintering conditions, relative density, total Li-ion conductivity and composition

Substitution [mol%]	Sintering Atm./Temp. [°C] / Dwell time [h]	Relative Density [%]	Li-ion Conductivity [RT] [S cm^{1}]	ICP-OES Elements				
				Li	Li	La	Zr	Al	Ta
Un-substituted									
LLZ_Ar	Ar/1150/10	77	2.23E-08	6.94	3	1.98	-	-
Al-substituted									
20Al:LLZ	Ar/1150/10	90	1.89E-04	7.42	3	1.97	0.14	-
20Al:LLZ	Ar/1200/20	90	2.21E-05	7.05	3	1.98	0.16	-
20Al:LLZ	Air/1200/20	93	2.08E-05	6.91	3	1.98	0.13	-
36Al:LLZ	Ar/1150/10	90	2.45E-04	6.58	3	1.96	0.32	-
Ta-substituted								
20Ta:LLZ	Ar/1150/20	92	2.97E-04	6.79	3	1.76	0.05	0.21
40Ta:LLZ	Ar/1150/10	91	4.73E-04	6.22	3	1.53	0.07	0.40
60Ta:LLZ	Ar/1150/10	98	6.80E-04	6.35	3	1.35	0.04	0.57

In Figure 4.1 , the total Li-ion conductivity as a function of density is plotted for un-, Al and Ta substituted LLZ and the inset of an exemplary Nyquist plot for 40Ta:LLZ obtained at room temperature is shown. Unfortunately, the contributions from bulk and grain-boundary conductivity could not be resolved with the equipment and thus only the total ionic conductivity was used for comparison of the samples. For the samples sintered at 1150 °C, a clear dependence of the total conductivity on the density can be seen (black line as guide to the eye), whereas for the ones sintered at 1200 °C, the conductivity values appear to be much lower than expected.

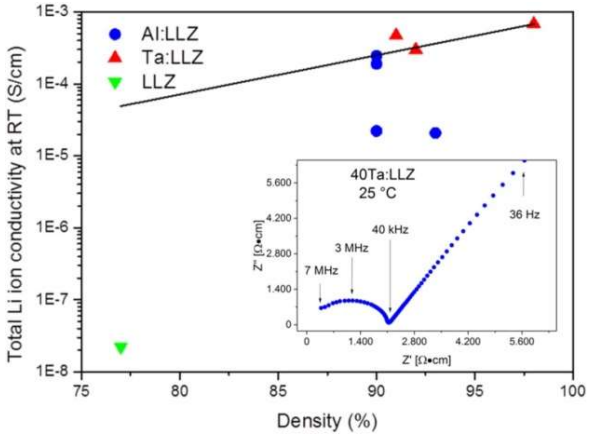

Figure 4.1- Total Li-ion conductivity for all samples at room temperature as a function of density. Inset: representative Nyquist plot for 40Ta:LLZ at room temperature from 7 MHz to 36 Hz.

Rather than a change in the cubic to tetragonal ratio, this is most likely a result of the formation of small amounts of secondary phases that are below the detection limit of XRD, since this sintering temperature is closer to the decomposition temperature. Additionally, if the 1150 °C data are extrapolated to 77% density, it is obvious that the conductivity value for the un-substituted LLZ is about three orders of magnitude lower than might be expected on the basis of these data. An explanation that found widespread acceptance in literature is the existence of a poorly conducting tetragonal phase [84, 85, 166], which appears also to be reasonable for the current un-doped material. Hence, in following the effect of the phase composition is discussed in more detail.

Figure 4.2 presents the X-ray diffraction patterns for polycrystalline LLZ, 60Ta:LLZ and 36Al:LLZ. For LLZ the patterns are consistent with a single tetragonal phase. 60Ta:LLZ 40Ta:LLZ and 20Ta:LLZ substituted that was sintered in Argon at 1150 °C for 20 h showed purely a cubic phase (see Table 4.2), whereas the other specimens (see X-ray diffraction patterns in Appendix) revealed a mixture of cubic and tetragonal phases.

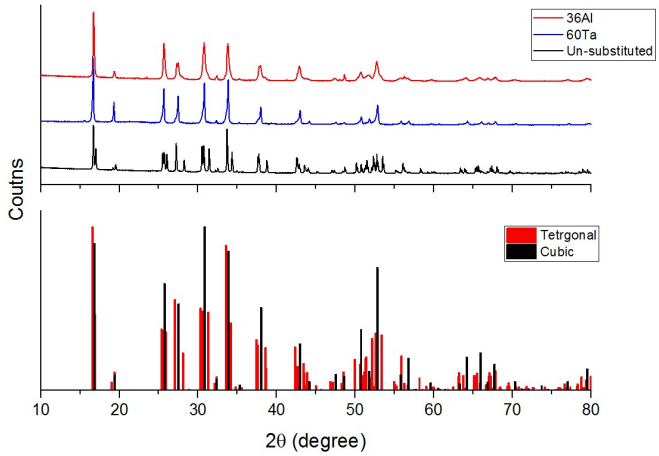

Figure 4.2- XRD patterns of pure LLZ, 60Ta and 36Al doped LLZ.

Rietveld refinement was used to obtain the respective tetragonal and cubic phase fractions, being compiled in Table 4.2, which verified the influence of the substitution and sintering conditions on the crystal structure. It can be deduced that, for Al substituted LLZ, higher sintering temperatures and using air instead of Ar, reduced the tetragonal phase amount significantly, even for the same Al concentrations. For Ta substituted LLZ an almost pure cubic phase was obtained when sintered in Ar, although some tetragonal phase was observed when sintered in air. However, this does not seem to affect the overall conductivity very much, a behavior also reported previously for Al substituted LLZ [164]. As a result, the Al substituted LLZ samples obtained here show no significant dependence on the volume fraction of tetragonal or cubic phase. Within the Al and Ta substitution, a variation of up to a factor 2 to 5 can be found, which is, however, also a result of the processing and not only due to intrinsic material properties. In summary, the substitution and processing of LLZ with the resulting correlation of, porosity and phase content to the ionic conductivity, shows that both have a strong impact and are thus of utmost importance to the final cell performance.

Table 4.2- Lattice parameters and portion of tetragonal phase obtained from Rietveld refinement.

Substitution [mol%]	Sintering Atm./Temp. [°C] / Dwell time [h]	$a_{tetragonal}$ [Å]	$c_{tetragonal}$ [Å]	Cubic [Å]	Proportion of tetragonal phase [%]
Un-substituted					
LLZ_Ar	Ar/1150/10	13.1239	12.6639		100
Al-substituted					
20Al:LLZ	Ar/1150/10	13.114	12.681		100
20Al:LLZ	Ar/1200/20	13.114	12.691	13.000	85-95
20Al:LLZ	Air/1200/20	13.093	12.716	12.970	40-60
36Al:LLZ	Ar/1150/10	13.074	12.802	12.988	45-55
Ta substituted					
20Ta:LLZ	Ar/1150/20			≈12.94	0
40Ta:LLZ	Ar/1150/40			≈12.94	0
60Ta:LLZ	Ar/1150/10			≈12.94	0

To obtain a deeper understanding of microstructural effects, which are also very important especially for the mechanical properties, Figure 4.3 shows typical cross-sections of the un-substituted LLZ as well as Ta and Al substituted LLZ samples. The microstructure of the un-substituted LLZ consists of a large open porosity and the grain size varies from 2 to 30 µm. In general, Al:LLZ samples possessed bigger grains, with sizes up to 300 µm and Ta:LLZ specimens had grains size from 4 to 30 µm, both featuring larger amounts of closed pores inside the grains. Resulting porosities are compiled in Table 4.1.

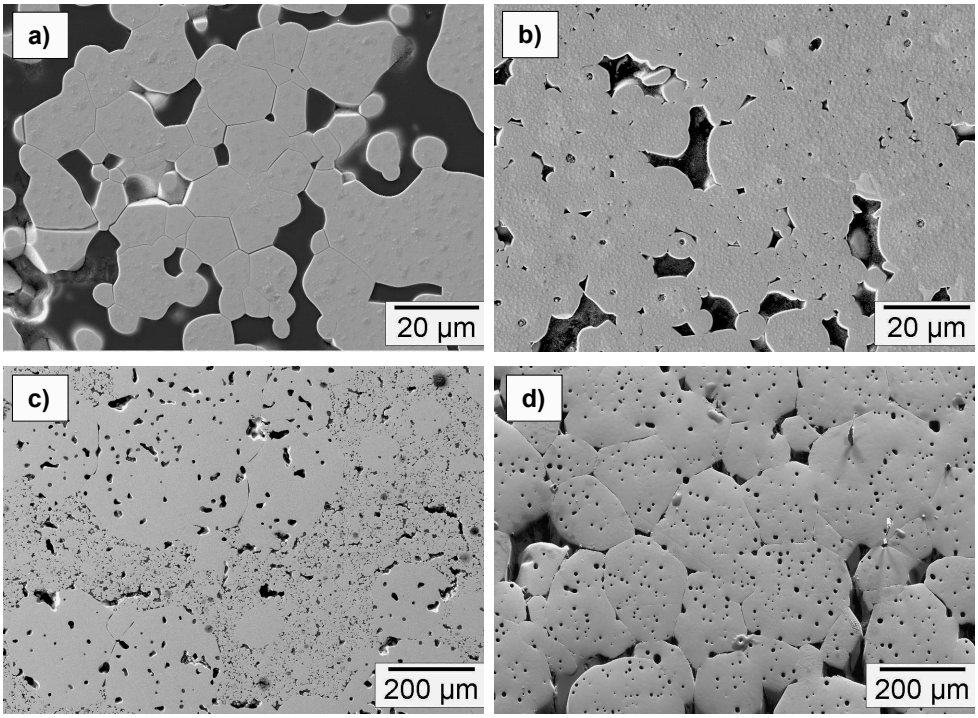

Figure 4.3 - SEM micrographs of a) un-substituted LLZ sintered in argon at 1150 °C for 10 h b) 60Ta:LLZ sintered in argon at 1150 °C for 10 h c) 20Al:LLZ sintered in argon at 1150 °C for 10 h and d) 20Al:LLZ sintered in air at 1200 °C for 20 h.

4.1.2. Mechanical testing results

The aforementioned microstructural effects play an important role in the interpretation of assessed mechanical properties of the samples. Depending on the load and associated indentation depth, the response of the specimen will be dominated either by the material (material properties subscript mat) or by microstructural features related to the porosity and imperfections (effective properties subscript eff). Derived from the average grain sizes and closed pores in the microstructures, the material´s properties of our samples were determined on the basis of a penetration depth of only a few hundred nanometers. The impression sizes of the indents in these cases are very small, thus it can be assumed that the effects of the porosity and grain size, shown in Figure 4.3, are negligible

and the obtained values are representative of the real materials properties. The respective data are presented in Table 4.3 to get insight into the effects of Al and Ta substitution.

Table 4.3- Effect of Al and Ta doping on porosity, phase content, elastic modulus and hardness.

Substitution [mol%]	Sintering Atm./Temp./ Dwell time [°C] [h]	Porosity [%]	Tetragonal Phase %	E_{mat} [GPa]	H_{mat} [GPa]	E_{eff} [GPa]	H_{eff} [GPa]
Un-substituted							
LLZ	Ar/1150/10	23	100	156 ± 9	10.1 ± 0.5	71 ± 3	2.1 ± 0.6
Al-substituted							
20Al	Ar/1150/10	10	100	161 ± 2	10.3 ± 0.3	125 ± 11	6.8 ± 1.1
20Al	Ar/1200/20	7	85-95	163 ± 4	10.3 ± 0.2	162 ± 5	7.6 ± 0.6
20Al	Air/1200/20	10	40-60	162 ± 1	9.6 ± 0.3	134 ± 16	6.4 ± 1.1
36Al	Ar/1150/10	10	45-55	142 ± 1	10.7 ± 0.1	127 ± 7	6.7 ± 1.3
Ta substituted							
20Ta	Ar/1150/20	8	0	141 ± 2	9.0 ± 0.2	117 ± 6	6.2 ± 0.9
40Ta	Ar/1150/10	9	0	124 ± 3	9.8 ± 0.4	82 ± 10	5.2 ± 1.0
60Ta	Ar/1150/10	2	0	149 ± 7	11.8 ± 0.2	97 ± 8	5.8 ± 1.2

For the Al substituted material, the materials elastic moduli of the specimens sintered at the 1200°C under either Ar or air agree very well with the data obtained for the specimen sintered at 1150°C for the same dopant level. The elastic modulus decreases for higher Al contents, however, the lower amount of cubic phase for the specimen sintered at 1200 °C under Ar is not reflected in the data. Tetragonal and cubic proportions below 10% by weight are not detectable, therefore are not presented here, as well as small amounts of secondary phases that are below the detection limit of XRD.

Figure 4.4 a) presents the elastic modulus of the material E_{mat} for the Al substituted material along with a data point from literature [13] (open square), for the sintering condition Ar, 1150°C, 10 h. The E values obtained in this work are in good agreement with values from literature for dense material 28% mol Al-LLZO, in fact, the elastic modulus measured via dynamic nano-indentation is reported to be 150.3 ± 2.2 GPa [13].

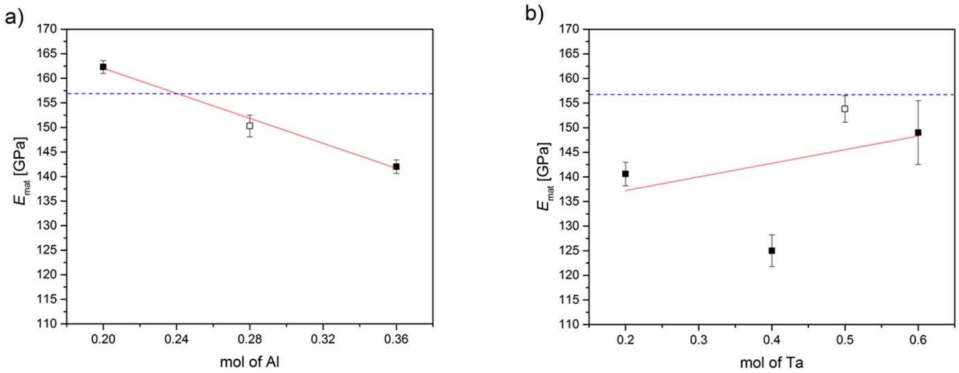

Figure 4.4 - (a) E_{mat} for 36Al- and 20Al-LLZ Al dopant and a data point for 28Al-LLZ from literature[13] (open square). (b) E_{mat} for 60Ta- 40Ta- and 20Ta-LLZ sintered in Ar for 10 h and a data point for 50Ta-LLZ from literature [13] (open square). Value for un-substituted LLZ is shown for comparison as dashed line.

Overall, for the investigated Al substitutional range, the elastic modulus of the material increases with the substitutional level. Compared to the un-substituted material (dashed line), the elastic modulus is higher for low dopant levels (20%) and lower for higher ones (28:LLZ and 36:LLZ). In general, the elastic modulus is related to the lattice parameter, i.e. a smaller lattice parameter is a result of a stronger interatomic bonding and hence higher apparent elastic modulus. In the case of Al substitution, the lattice parameter $a_{\text{tetragonal}}$ decreases, while $C_{\text{tetragonal}}$ increases with increasing substitution level, leading to an overall increase of the elastic modulus. This structural change leads to an overall increase of the elastic modulus. However, at higher substitutional levels the amount of tetragonal phase decreases, which in turn leads to a decrease of the elastic modulus due to the lower elastic modulus of the cubic phase (see Ta:LLZ results, below). The decrease due to the cubic phase is stronger than the increase due to the change of the lattice parameters of the tetragonal phase, leading to an overall decrease for 28:LLZ and 36:LLZ and, hence, absolute values below that of the un-substituted LLZ (dashed line) in Figure 4.5.

Figure 4.4 b) shows the Young's modulus (E_{mat}) as a function of the Ta substitution along with a data point from literature. Overall, the E_{mat} of Ta substituted material obtained in the current work are in good agreement with the experimental value of $E = 153.8 \pm 2.7$ GPa reported for 50 mol%

Ta:LLZ with 97% relative density, measured by dynamic nano-indentation, and also the value calculated by DFT extrapolation (298 K) $E = 147.2$ GPa [13].

In contrast to the Al:LLZ case, it can be seen that the elastic modulus tends to increase with Ta substitution, although the scatter, especially at higher substitution levels, is rather large. Compared to the un-substituted material (dashed line), the elastic modulus is lower, which is attributed to the predominant cubic phase, which is then in good agreement with the effect of a cubic phase in the case of Al substitution (see above). At higher substitutional levels the elastic modulus becomes again more similar to that of the un-substitution material, where a slight bias of the data by grain size and porosity differences cannot be ruled out.

The larger scatter of the hardness data for low loads that were applied to obtain the materials properties, is mainly related to the surface (roughness) sensitivity of this materials property (plastic zone is typically ten times smaller than elastic zone), does only permit a general support of the trends observed for the elastic modulus for the Ta substitution material. To obtain the effective values for elastic modulus and hardness, higher loads of ~ 500 mN (penetration depth of ~2000 nm) were chosen to be representative for the global behavior of the materials and investigate especially the effect of porosity. Figure 4.5 shows indentation marks on 20Al:LLZ obtained at higher loads, revealing possible moisture related degradation at the surface, which occurred during the transfer from the nano-indenter to SEM. Moisture effects are considered in more details in section 4.1.4.

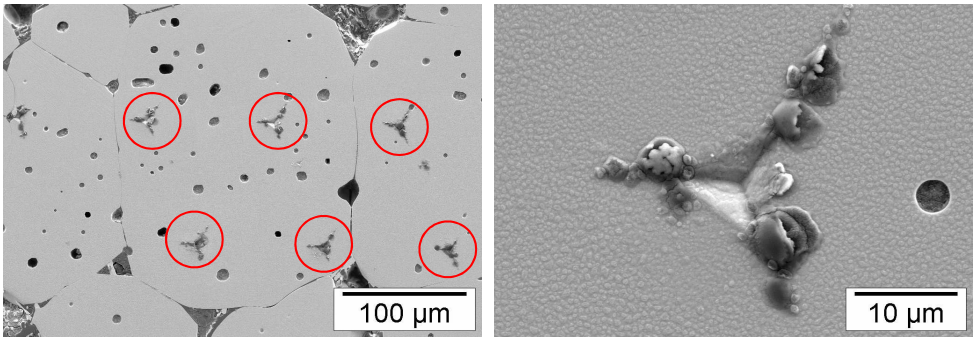

Figure 4.5- SEM micrographs of indentation marks at 500 mN on 20Al:LLZ.

The effective data are compiled in Figure 4.6 a) and b), respectively, where Ta doped and Al substituted specimens are indicated by different colors. In general, hardness and elastic modulus should decrease with increasing porosity and increasing grain size. However, contrary to initial expectations, a clear decrease of both properties with increasing porosity is not revealed, but is superimposed by the significant changes of the materials properties that was discussed above, e.g. the slightly higher E_{mat} of the of the Al:LLZ compared to the Ta:LLZ and the effect of the dopant level.

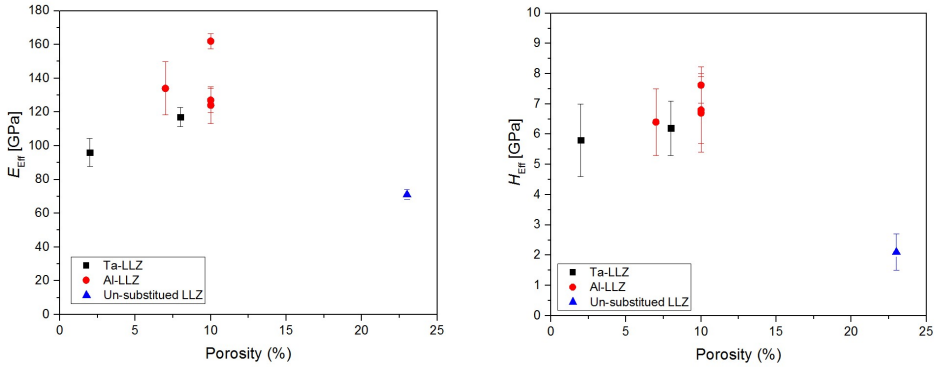

a) b)

Figure 4.6- Effective mechanical properties (determined using high loads) plotted as function of porosity (a) effective elastic modulus (E_{eff}) (b) effective hardness (H_{eff}).

Comparing only Al substituted and un-substituted material, the expected trend, a decrease with increasing porosity, becomes more apparent. However, it has to be considered that, although being a global property, this effective elastic modulus is also affected by the materials elastic modulus, hence, especially for the 36Al-LLZ the value is decreased, since this material possess as materials property a lower value than the un-substituted and the 20% Al substituted material. The 20Al substituted specimen sintered at 1200°C in Ar has a value that is higher than all other specimens indicating that, since materials properties agree with the other 20% substituted specimens, the local porosity might have been inhomogeneous for this specimen and the locally tested volume in the considered measurements was rather dense.

In case of the Ta substituted specimens no trend can be observed but all modulus values appear to be rather low for the considered porosity range, however, again it has to be considered that the effective elastic modulus is also affected by the materials elastic modulus and values for the Ta substituted material were lower than for the un-substituted material, leading then to also rather low global values for the tested porosity range.

This effects need to be considered during component manufacturing and modelling, since the deviation from the materials values is large, even for rather dense samples (92–98% of theoretical density) and global, effective elastic properties are often reflected in reduced materials fracture stress. Otherwise, this behavior (i.e. the lower global properties) might lead to unexpected component failure due to insufficient mechanical stability, especially when parts with large areas and small thickness need to be handled. Overall, the behavior observed for the elastic moduli is also reflected in the hardness values.

Finally, the dependence of the effective properties on grain size has been analyzed. LLZ consists of a large open porosity and the grain size varies from 2 to 30 µm, Al:LLZ samples possessed bigger grains, with sizes up to 300 µm and Ta:LLZ specimens had grains size from 4 to 30 µm. In general, the data appear to indicate an increase of elastic modulus and hardness with increasing grain size [167], however, for the Ta substituted material data are again biased also by the lower materials property compared to un-substituted material, as discussed above for the locally measured properties. The un-substituted LLZ on the other hand shows rather low elastic modulus and hardness values at the particular grain size, 71 ± 3 GPa and 2.1 ± 0.6 GPa, respectively, since here the porosity effect dominates (Figure 4.6) i.e. the porosity of this particular specimen is more than double of that of all doped specimens since production of more dense un-substituted material was not possible.

4.1.3. Conclusions and outlook

Garnet structured $Li_7La_3Zr_2O_{12}$ substituted in terms of different ratios of Ta and Al, sintered under various conditions, was characterized with respect to electrical properties, phase composition, microstructure and as main focus, mechanical properties.

The substitution has a high impact on the total Li-ion conductivity, with Ta generally outperforming some of the Al substitution based compositions and both being approx. 4 orders of magnitude better than un-substituted LLZ, even if effects of porosity are considered.

Rietveld refinement revealed the influence of the substitution and the sintering conditions on the crystal structure. For Al:LLZ, higher sintering temperatures and using air instead of argon reduced the amount of tetragonal phase significantly, even for the same Al concentrations, but resulted in poor total Li-ion conductivity. For Ta:LLZ, an almost pure cubic phase was obtained when sintered in argon, although some tetragonal phase was observed when sintered in air. However, this does not seem to affect the overall conductivity very much.

With respect to the mechanical properties, the elastic modulus of Al:LLZ is affected by both lattice parameter and phase ratio, leading to an increase at low and a decrease at higher substitutional levels compared to the un-substituted LLZ. For Ta:LLZ the values are always lower than for un-substituted LLZ, however, slowly approaching this value at higher dopant levels, which can again be related to lattice parameter and phase ratio.

Global, effective specimens mechanical properties obtained at higher indentation depths/loads are affected by both the properties of the material itself (including grain size effects) and the porosity. For Ta:LLZ the rather low values even for high density samples need to be kept in mind when considering component design and manufacturing, since often elastic moduli behaviors are also reflected in materials fracture strengths.

4.1.4. Porosity effect

In order to investigate the porosity effect onto the mechanical properties systematically, the most promising electrolytes were selected, particularly 40 mol% Ta-substituted LLZ, $Li_{6.6}La_3Zr_{1.6}Ta_{0.4}O_{12}$, and 20 mol% Al-substituted LLZO, $Li_{6.4}La_3Zr_{1.6}Al_{0.2}O_{12}$ and submitted to a more detailed mechanical investigation. Materials were systematically sintered for different dwell times in order to obtain samples with different apparent densities. The powders were produced by a partner from IEK-1 and the samples were pressed and sintered in IEK-1 by the present author. The following sections present microstructural and mechanical results for both materials. Since being out of the main focus here, the conductivities for these samples were not measured.

It is important to note that, even though the battery system relies on a dense electrolyte and the goal is investigate dense materials, it is crucial to understand the role of the porosity since the most common synthesis procedure, solid state reaction, normally results in some residual porosity (~10%). Optimized materials produced via hot-pressing are investigated in this work and the results are presented and discussed in a forthcoming chapter.

20Al:LLZ

Microstructure and phase composition

Table 4.4 presents the microstructure, grain size and porosity of 20Al:LLZO sintered for 2, 20 and 40 h dwell time, respectively. The choice of the sintering time was based on previous investigations of high conductive mixed phase Al-substituted LLZO [168]. In this case, the porosity measurement was carried out with software AnalysSIS using SEM images, more details can be found in the experimental section. Overall, as expected, the porosity decreased with increasing sintering time. The microstructure has a bimodal grain distribution for all sintering times, revealing areas with larger grains and areas with smaller grains with residual porosity, the average grains sizes are compiled in Table 4.4.

Table 4.4- Microstructure, grain size and porosity of Al-substituted LLZO sintered for different dwell times.

	20Al:LLZ-2h	20Al:LLZ-20h	20Al:LLZ-40h

Optical and SEM images	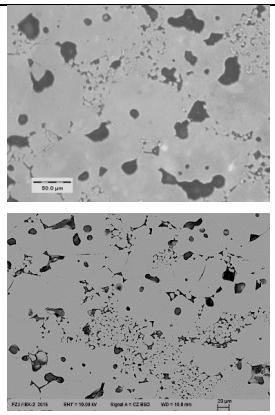	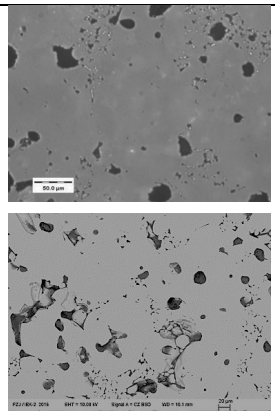	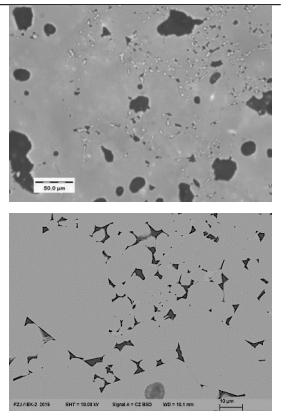
Grain size (μm)	Large grains – 56.3 Small grains 6.8	Large grains 87.2 Small grains ≤ 10	Large grains 83.2 Small grains ≤ 10
Porosity*(%)	13.8	11.2	9.7

* Uncertainty is ~ 2.5% for all samples.

Figure 4.7 shows the XRD patterns of 20Al:LLZ-2 h, the characteristic six main reflexes between 50 and 55 indicate that the samples consists of tetragonal phase. Investigation with Rietveld refinement revealed that all samples consisted of mixed tetragonal and cubic phases. Minor impurities such as $LiAlO_2$ and $La_2Li_{0.5}Al_{0.5}O_4$ were detected.

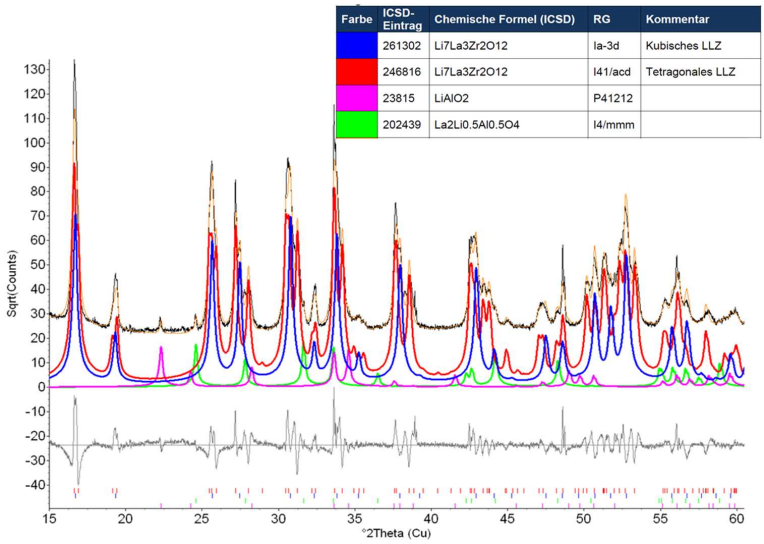

Figure 4.7- XRD pattern of 20Al:LLZ-2h.

In order to provide a better understanding and correlate the mechanical properties with grain orientation, EBSD test was carried out. However, even though the preparation was carefully performed, only one of the tests partially worked on 20Al:LLZO-2h, however, the results were inconclusive, the image is displayed in Appendix. The failure to achieve successful EBSD tests was attributed to the formation of a soft layer on the surface of all tested LLZO, which resulted in a weakening of the patterns.

Mechanical properties and fracture behavior

Mechanical properties of 20Al:LLZO were investigated using a Berkovich diamond tip indenter under continuous multi-cycling (CMC) mode to permit a rather fast assessment of the properties as function of load/depth. Figure 4.8 a) and b) illustrate the individual multi-cycle indentation test results as function of displacement, corresponding to elastic modulus and hardness. Figure 4.8 c) gives the average and standard deviation of the mechanical properties as function of displacement.

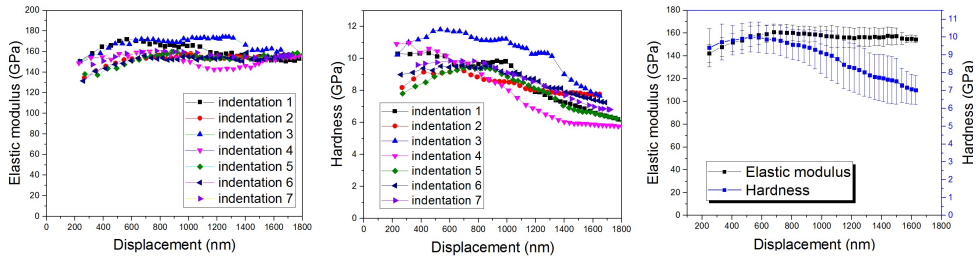

a) b) c)

Figure 4.8 - Mechanical properties of 20Al:LLZO-2h as function of depth displacement a) single results of elastic modulus b) single results of hardness c) average of *E* and *H* as function of penetration depth.

Table 4.5 compiles the mechanical properties at low load range and high load range, respectively, extracted from the average of all indentation. The elastic modulus of the material obtained from the low load range and low penetration depths (corresponding to ~ 50 mN and 300 - 600 nm) is higher than the elastic modulus of the bulk of the specimen obtained at higher penetration depths and higher load (~ 500 mN, 1600-2000 nm). Looking at the materials properties for 2 and 20 h sintering time samples, they are independent of porosity as expected, and also for 40 h considering the uncertainty. Assuming that at the maximum penetration depths the area beneath the indentation it is much larger, the values can be affected by residual porosity and grain boundaries, therefore referred here as effective properties. For effective elastic properties, for 20 and 40 h the results agree within the limits of uncertainty. For the hardness the expected trend is observed, the effective hardness decreases with increasing porosity.

Surprisingly and in contrast to expectations, the elastic modulus is rather constant for 20Al:LLZO-2h, even for larger penetration depths, revealing that the locally measured property was not affected by microstructural inhomogeneities or defects. Note, for the testing with Al-doped LLZO, the indentations were intentionally placed in dense areas (not necessarily equally spaced, as for the next material 40Ta:LLZO) and for 20Al:LLZO-2h specifically, it could be that not a representative porosity was encountered beneath the tested surface. This is the possible origin why the mechanical properties remained constant even at higher penetration depths. Such behavior was observed also for one of the Al-doped materials (20A:LLZO with 7% porosity) in the previous section, where materials properties and effective properties are the same, indicating that for an assessment of

global porosity effects testing of larger effective volumes are necessary, i.e. using for example impulse excitation, which could not be realized in the current study due to limits in materials availability and specimens' geometries.

As stated above, looking at the hardness, it reveals a decrease with increasing load, such an effect was noted also for the other samples (see Table 4.5, graphs are displayed in Appendix), where a diminution of approximately 30% is observed for the effective hardness.

Comparing the values from Table 4.5 with similar composition in the previous section, the materials properties, elastic modulus and hardness are in the same range, ~161 GPa and ~10 GPa, respectively.

Table 4.5 – Mechanical properties of Al-substituted LLZ material, extracted from CMC mode at the low load range (materials properties) and high load range (effective properties).

	Elastic modulus (GPa)	
Specimen	**Materials properties**	**Effective**
20Al:LLZO-2h	159.2 ± 8.3	155.4 ± 7.1
20Al:LLZO-20h	154.3 ± 8.5	120.6 ± 8.6
20Al:LLZO-40h	145.5 ± 7.7	113.4 ± 5.7
	Hardness (GPa)	
Specimen	**Materials properties**	**Effective**
20Al:LLZO-2h	10.1 ± 0.8	7.0 ± 0.8
20Al:LLZO-20h	9.8 ± 0.9	7.5 ± 0.9
20Al:LLZO-40h	10.5 ± 0.8	8.7 ± 0.6

To investigate the influence of porosity at higher loads (1 N in this case, due to sample size), 25 indentations where placed at determined dense areas, test with a Vickers diamond tip (Fischer) applying 1 N load, the tests were done in a glove box with nitrogen. Table 4.6 gives the results obtained for elastic modulus, hardness and the corresponding maximum penetration depth, h_m. Figure 4.10 shows the surface with indentation marks on the denser locations, as an example of effects on the material behavior, which is discussed in more details in the following.

Table 4.6- Elastic modulus, hardness and maximum penetration depth of 20Al:LLZO obtained for Vickers indentation at 1 N.

	Effective Properties at 1 N		
	E (GPa)	H (GPa)	h_m (nm)
20Al:LLZO-2h	93.1 ± 6.2	6.8 ± 0.7	~3000
20Al:LLZO-20h	103.9 ± 5.2	8.4 ± 0.7	~2750
20Al:LLZO-40h	117.0 ± 5.7	8.6 ± 0.6	~2700

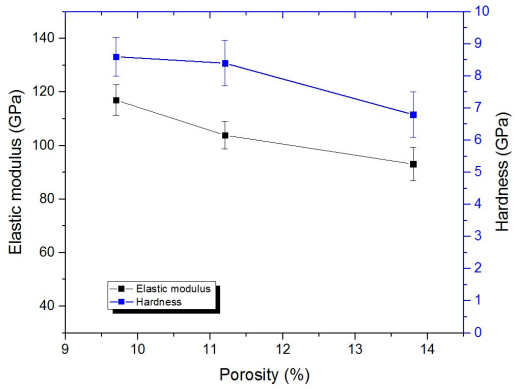

Figure 4.9 - Influence of porosity on mechanical properties of 20Al:LLZ sintered for different dwell times.

Since the indentation test was performed load-controlled, the maximum penetration depth (h_m) was different for all tested samples. As might be expected, the porosity reduces both elastic modulus and hardness, even though the material appeared to be dense in the surface, due to apparent porosity within the effectively deformed volume (ten times the plastic zone, i.e. ~1500 μm^3).

Figure 4.10 shows SEM micrographs of typical indentation marks; load of 1 N on 20Al:LLZO. To determine the fracture toughness, the materials properties E and H presented in Table 4.5 were used. The obtained results are summarized in Table 4.7 and are discussed next.

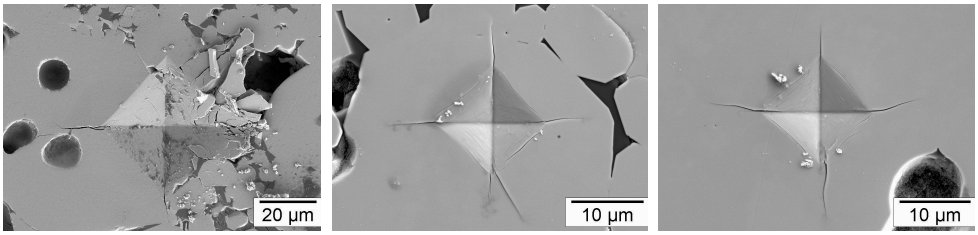

a) b) c)

Figure 4.10- SEM micrographs of typical indentation marks at 1 N in a) 20Al:LLZO-20h; b) 20Al:LLZO-2h; c) 20Al:LLZO-40h.

Even though the average crack length is ~ 9 µm for all samples (see in Table 4.7), the resultant cracks exhibited rather asymmetrical lengths and spallation in regions close to porous and smaller grain, a behavior observed especially for 20Al:LLZO-2h, probably due to its larger porosity.

In order to calculate the VIF toughness an accurate crack shape determination is necessary. A way to determine the indentation crack shape is to break up a sample after applying a line of indents and observe the area beneath the indents. Two compositions 20Al:LLZO-2h and 20Al:LLZO-40h (the most porous and the denser) were selected as example to illustrate the materials' behavior, see Figure 4.11. Concentrating on this aspect, the load was kept constant at 1 N in order to verify the K_{IC} dependence on porosity; the final K_{IC} value was based on minimum 5 indentations.

The crack growth appears to be highly influenced by aspects influencing the local stress field in the respective local microstructure, i.e. grains and porosity. It is also possible to observe a transgranular crack mode, in both small and larger grains. Furthermore, in the central region beneath the Vickers impression, which is under compression stress, the material crushed. Overall, a determination of crack shape was not possible using this method due to the microstructural complexity and hence, instead it was purely based on the criteria $0.25 \leq l/a \leq 2.5$ indicative of Palmqvist crack shape. Hence, the calculation of Vickers fracture toughness (VIF) was performed applying a load of 1 N and utilizing Equation 6 from section 2.2.3.1 for a Palmqvist crack shape [114].

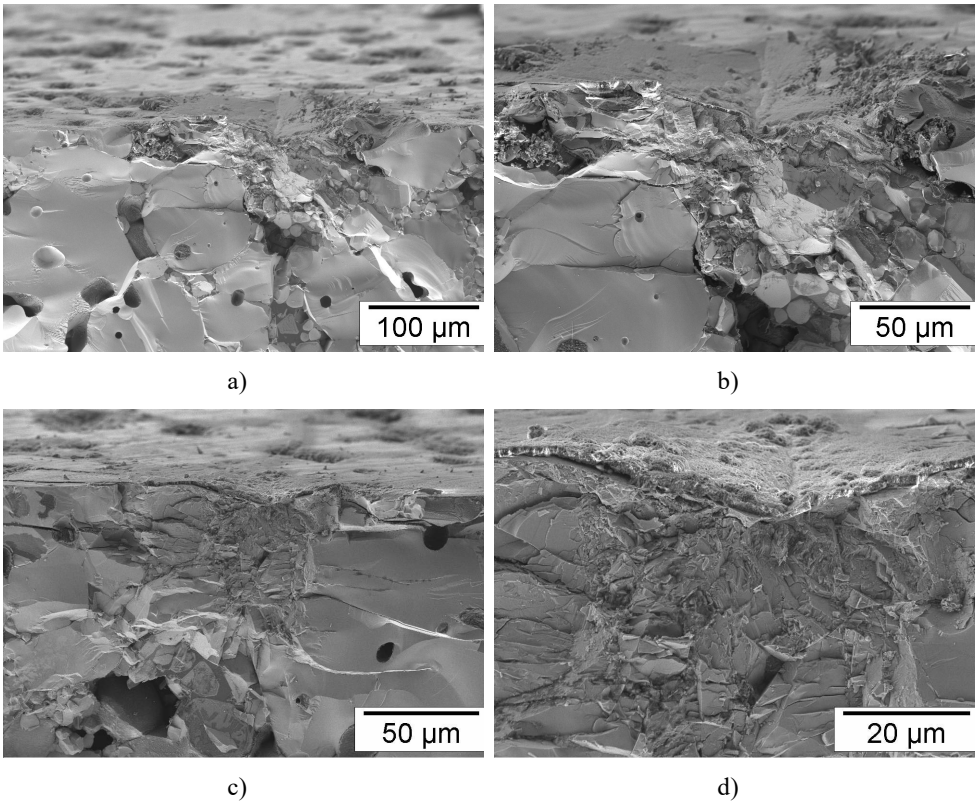

Figure 4.11- SEM images of indented cross-sections of a) and b) 20Al:LLZ-2h lower and higher magnification and c) and d) 20Al:LLZ-40h lower and higher magnification.

Table 4.7- Summary of average crack length, *l/a* ratio and K_{IC} of 20Al-subsituted LLZO.

Specimen	Average crack length *l* (µm)	*l/a*	K_{IC} (MPa·m$^{0.5}$)
20Al:LLZ-2h	9.7 ± 2.0	1.3	1.28 ± 0.10
20Al:LLZ-20h	9.0 ± 1.9	1.2	1.33 ± 0.15
20Al:LLZ-40h	9.5 ± 1.8	1.3	1.40 ± 0.10

The determination of the cracks lengths was difficult in the cases where the indentations were affected by porosity and local defects even for the denser sample (see Figure 4.12); these led to a

rather high deviation in the crack length measurement (~ 20%) and higher uncertainties in the final K_{IC}.

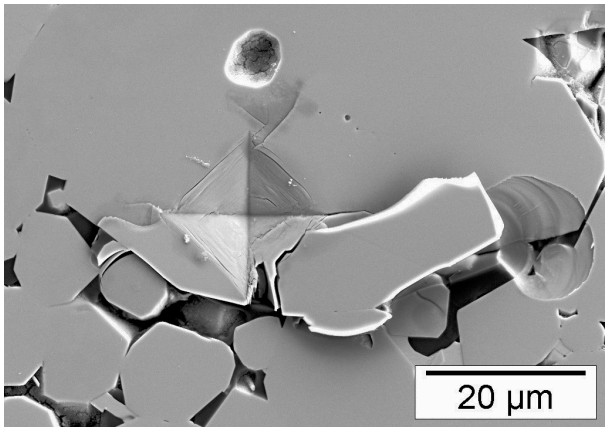

Figure 4.12- SEM micrographs of typical indentation marks at 1 N in 20Al:LLZO-40h.

An apparent porosity effect is observed; the fracture toughness increased from 1.28 to 1.40 MPa·m$^{0.5}$ with decreasing porosity (from 13.8 to 9.7%), being in contradiction to literature reports for similar material, where samples of different densities and grain sizes (85 to 98%, 2.7 to 3.7 µm) have shown an increase of fracture toughness with increasing the porosity [156]. It was suggested by these authors that crack deflection along grain boundaries can explain the increase in fracture toughness with decreasing relative density, an effect that cannot be confirmed by the current study.

40Ta:LLZO

Microstructure and phase composition

Table 4.8 presents the microstructure, grain size and porosity of 40Ta:LLZO sintered for 4, 8 and 16 h dwell time. The choice of the sintering times was based on previous investigations [144]. Porosity and grain size were measured using the same methods as in the previous section, for 20Al:LLZO. As expected the porosity decreased with increasing sintering time and the grain size remained constant within the limits of uncertainty.

Table 4.8 –Microstructure, grain size and porosity of 40% Ta-substituted LLZO sintered for different dwell times.

	40Ta:LLZ-4h	40Ta:LLZ-8h	40Ta:LLZ-16h
SEM Images	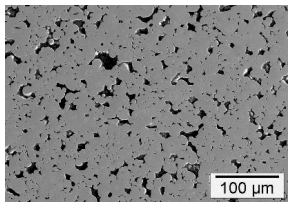 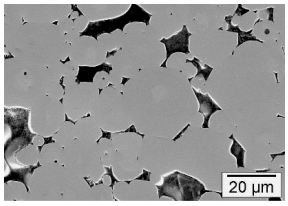	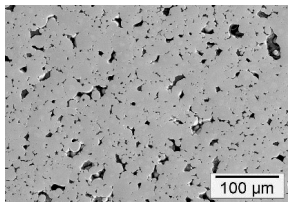 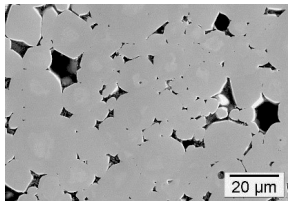	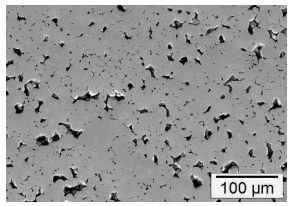 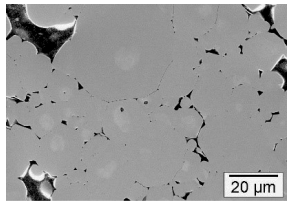
Grain size (µm)	9.2 ± 5.0	10 ± 5.0	12.8 ± 6.0
Porosity* (%)	13.8	10.2	8.7

* Uncertainty is approximately ± 1.5% for all samples.

X-ray diffraction was used to characterize the phases of samples after sintering, the XRD spectra of 40Ta:LLZ-16h is shown in Figure 4.13, XRD for other compositions are given in Appendix. The sintered materials mainly consist of cubic phase, space group Ia-3d SG, however, a weak reflex of a second phase was seen, which was identified to be perovskite lanthanum aluminate ($LaAlO_3$), reference code (01-070-4109). The lattice parameter calculated for the main phases are

a = 12.450 Å and 12.448 Å, for 40Ta:LLZ-8h and 40Ta:LLZ-16h. It is not clear if the second phase can have an effect on the mechanical properties of the material. For 40Ta:LLZ-4h pure cubic phase was identified, lattice parameter a = 12.949 Å.

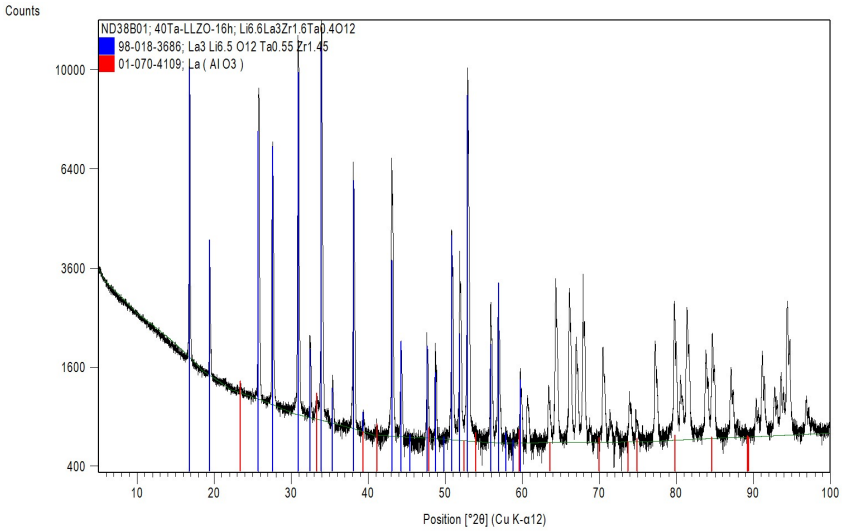

Figure 4.13- XRD spectra of LLZ:Ta-16h after sintering.

The energy dispersive X-Ray analyzes (EDX) was used to identify the elements composition of 40Ta:LLZ-16h along the grains. Figure 4.14 gives the compositional maps of the chemical elements; it is observed that zirconium, oxygen and lanthanum are well distributed within the surface. However, there is a lack of Zr and enrichment of Ta in the grains or boundaries, which can lead to differences into the properties in the grain and grains boundaries.

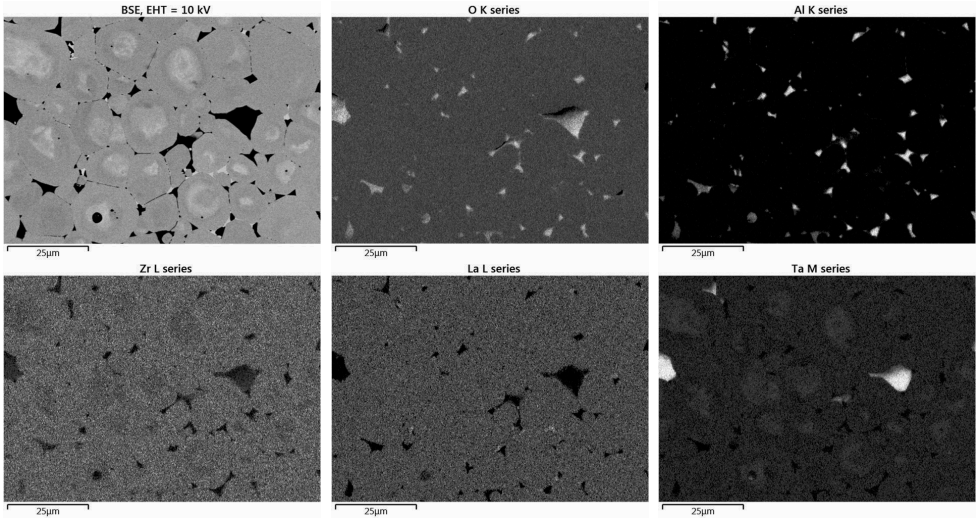

Figure 4.14- Compositional mappings of 40Ta:LLZ-16h for Zr, O, La, Al and Ta.

Mechanical properties and fracture behavior

Similar to the previous mechanical investigation of 20Al:LLZO, elastic modulus and hardness of Ta-substituted LLZO were investigated using a Berkovich diamond tip under continuous multi-cycling (CMC). Figure 4.15 illustrates the individual multi-cycle indentation test results as function of displacement, corresponding to elastic modulus and hardness. Figure 4.16 gives the average and standard deviation of the mechanical properties as function of displacement.

Elastic modulus and hardness gradually decrease as the depth increases for all measured specimens. As the load is gradually increased to 500 mN, the affected elastic and plastic zone beneath the indenter increase. When load-carrying zone increases, the effect of grain boundaries, inhomogeneity and flaws on the mechanical properties increases, which appears to decrease the properties of the material. This means also that as the indentation depth increases, the determined *E* and *H* of the sample get closer to the properties representative of the bulk (see also results for 20Al:LLZ). Therefore, again two different approaches were applied to evaluate the mechanical properties, which are explained in more detail below.

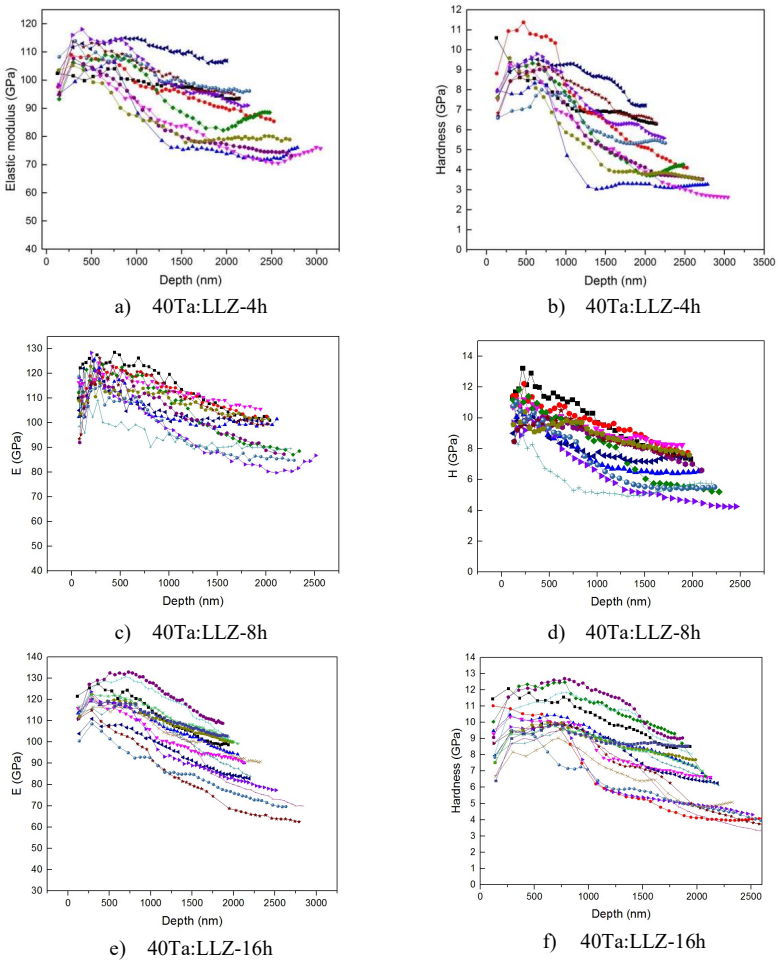

Figure 4.15- Elastic modulus and hardness curves of function of penetration depth of a) and b) 40Ta:LLZ-4h; c) and d) 40Ta:LLZ-8h; e) and f) 40Ta:LLZ-16h.

Similar to the procedure for 20Al:LLZ, at low penetration depths (300 - 500 nm) the values are considerate representative of the material; and the bulk properties (effective) of the specimen are obtained at higher penetration depths and higher load (1900-2200 nm and 500 mN), since the penetration depth is larger and flaws are included in the tested volume. Figure 4.16 presents the curves of the averages of elastic modulus and hardness for the three specimens.

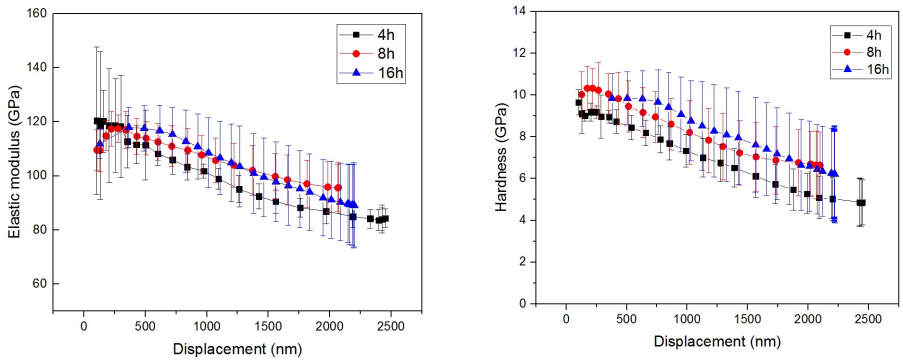

Figure 4.16- Average of elastic modulus and hardness of 15 indentations for LLZ with dwell time 4 h, 8 h and 16 h as a function of the penetration depth.

In addition, Table 4.9 compiles the mechanical properties for the low load range (5-100 mN), which represent depths of 300 to 500 nm and high load range (500 mN), which represents depths of ~2000 nm, respectively. Looking at Table 4.9, it appears that for low load ranges the materials properties are being representative of the intrinsic properties, and are independent of the porosity as expected. Comparing the values with E_{mat} from section 1.1.2, for 40Ta:LLZO (elastic modulus 124 ± 3 GPa, hardness 9.8 ± 0.4 GPa), the values are in good agreement, considering the experimental uncertainty, this is also the case for the effective properties (elastic modulus 82 ± 10 GPa, hardness 5.2 ± 1.0 GPa, porosity 9%).

Table 4.9- Elastic modulus and hardness of LLZ material, extracted from the low load range of CMC.

	Elastic modulus (GPa)	
Specimen	**Materials properties**	**Effective**
40Ta:LLZO-4h	118.5 ± 9.2	84.4 ± 4.0
40Ta:LLZO-8h	116.9 ± 6.8	95.4 ± 9.4
40Ta:LLZO-16h	117.9 ± 7.4	89.7 ± 14.0
	Hardness (GPa)	
Specimen	**Materials properties**	**Effective**
40Ta:LLZO-4h	9.2 ± 0.3	5.0 ± 1.0
40Ta:LLZO-8h	10.0 ± 0.9	6.6 ± 1.5
40Ta:LLZO-16h	9.4 ± 1.6	6.3 ± 2.2

The effective properties are lower, as expected, due to porosity effect and highly influenced by the local microstructure. Since the porosity range is limited and due to the high uncertainty, only the value for the higher porosity is clearly lower. Also the grain size is in the same range for all samples and an effect of this parameter can therefore be ruled out. In general, the elastic modulus is correlated to the interatomic distance, which implies that larger separation distance between atoms results in a lower elastic modulus. However, although the lattice parameter increases from 12.949 Å to 12.448 Å with increasing the sintering time, the intrinsic elastic modulus remains constant.

Fracture behavior

In order to analyze effects related to microstructural variations, a more detailed study was carried. The specimen 40Ta:LLZO-16h possesses different grains sizes, varying from ~2 up to ~ 45 µm in diameter, average grain size 12.8 µm, the applied load for this test was 1 N, which results in a diagonal imprinting of ~ 15 µm. Therefore, the indentations are highly affected by local microstructure, defect, pores and grain boundaries. First, the average of all measurements is shown, including the values affected by defects, porosity and denser areas. Then an analysis of indentations made in areas with apparent defects and pores is done, and at last, and analyses of the mechanical properties obtained for denser areas is presented.

To investigate the influence of porosity at higher load a matrix 5 × 5 indents was imprinted with a Vickers diamond tip (Fischer) applying a load of 1 N. The test was done in a glove box filled with nitrogen. Table 4.10 summarizes the results obtained for elastic modulus, hardness and the corresponding maximum penetration depth, h_m. Figure 4.17 shows the surface with indentation marks on 40Ta:LLZ-16h, which is discussed in more detail next.

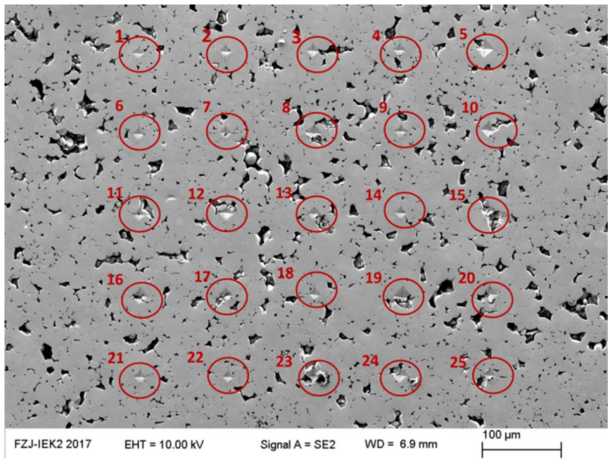

Figure 4.17- SEM micrographs of indented surface of 40Ta:LLZ-16h after test.

The mechanical properties presented in Table 4.10 are the average from the 25 indentations, including the ones that were done on defects, pores and denser areas. The obtained values are highly influenced by the local microstructure; which led to a high uncertainty. That is the reason why the deviation is rather high, about 10 to 15 % for elastic modulus and 20 to 35 % for hardness, which in the case of the higher deviation of the hardness values is due to the smaller plastic region being stronger affected by the undulations.

Table 4.10- Elastic modulus, hardness and penetration depth of 40Ta:LLZ obtained for Vickers indentation at 1 N.

	Effective Properties at 1 N		
	E (GPa)	H (GPa)	h_m (nm)
40Ta:LLZ-4h	67.7 ± 10.9	3.7 ± 1.3	3855 ± 538
40Ta:LLZ-8h	80.6 ± 7.9	5.3 ± 1.2	3281 ± 338
40Ta:LLZ-16h	85.2 ± 9.1	5.4 ± 1.4	3125 ± 299

Comparing the effective properties shown in Table 4.9 obtained at ~ 2000 nm depths and values from Table 4.10 obtained at depths from 3120 nm to 3855 nm, the elastic properties seems to be in good agreement also with the materials properties reported in section 4.1.2, except for

40Ta:LLZ-4h, which has revealed a reduction of approximately 20% with increasing penetration depth, confirming the pronounced porosity effect for this sample.

The local microstructure has a strong influence on the mechanical properties obtained from indentation. As expected, the sample 40Ta:LLZ-4h with 13.8 ± 1.1% of closed porosity showed the lowest elastic modulus and hardness. Whereas 40Ta:LLZ-16h revealed higher values of the mechanical properties. Figure 4.18 illustrates the mechanical properties versus porosity for 40Ta:LLZ sintered for different dwell times.

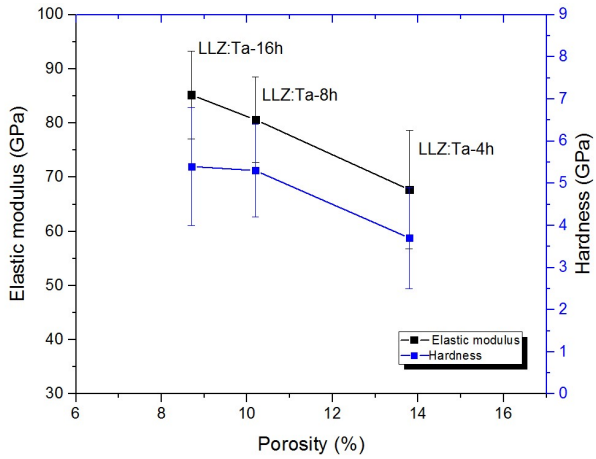

Figure 4.18-Influence of porosity on mechanical properties of 40Ta:LLZ.

Indentations performed close to pores or affected by them revealed reduced mechanical properties. Figure 4.19 illustrates as an example Vickers indentations on 40Ta:LLZ-16h that were highly affected by local defects and pores in the case of denser areas, obviously less affected by defects and porous. The values obtained for each imprint are given in the images. In the case of the ones with the highest mechanical properties, the imprints were located in single grains, although the cracks generate in the corner propagate into other grains. The highest elastic modulus and hardness for a grain at this load was E = 99.0 GPa and H = 7.4 GPa (hence still being much lower than the materials property in Table 4.9 due to the effect of pores still contacting the elastic zone in the surface and below), whereas for an area affected by porosity it was E = 71.2 GPa and H = 3.4 GPa.

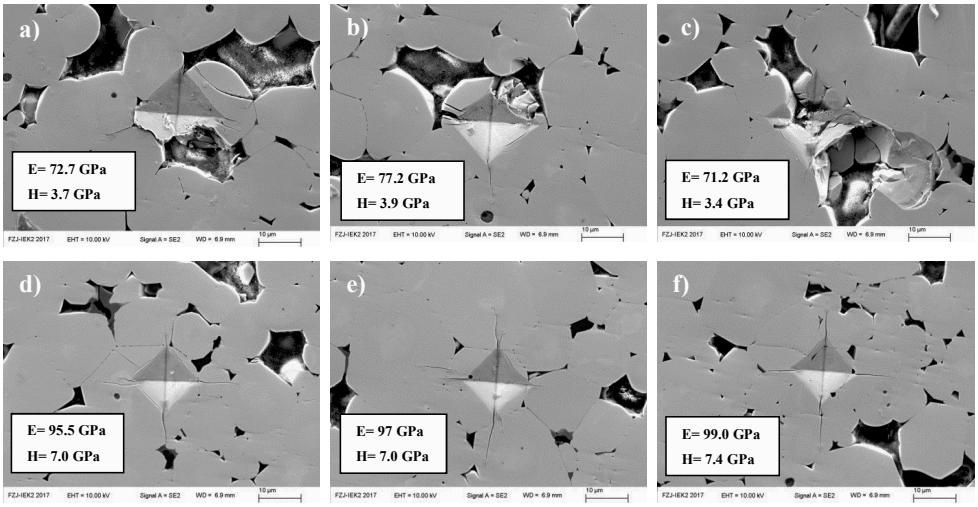

Figure 4.19- SEM micrographs of indentation marks of 40Ta:LLZ-16h on pores, load of 1N: a) b) and c) indentations highly affected by pores; d) e) and f) indentations marks on denser areas.

As result of the high load applied in these tests, it is possible to observe clearly the four cracks emanating from the corner of the indentation impression. The cracks can be used also to derive the fracture toughness of LLZ, however, looking carefully, some cracks appear to be affected by the local microstructure. Therefore, the cracks length can only be used to have a rough estimative of the specimens fracture toughness. Although many factors can affect the cracks path, the cracks that propagate from the corners are mainly straight and they will be carefully discussed in the next sub-section.

Figure 4.20 shows an investigation of the crack shape beneath the indentation, to identify the affected area beneath the indentation, analogous to the one performed for 20Al:LLZO. Similarly to the previous material, this method was unsuitable to determine the specific crack shape due to the complex microstructural features, and again the analysis was based purely on the criteria $0.25 \leq l/a \leq 2.5$ for Palmqvist crack shape. To determine the indentation fracture toughness the relationship of Niihara, Eq. 6 in section 2.2.3.1, was used [114]. E and H obtained at 300 nm were used in the calculation. Table 4.11 summarizes the results.

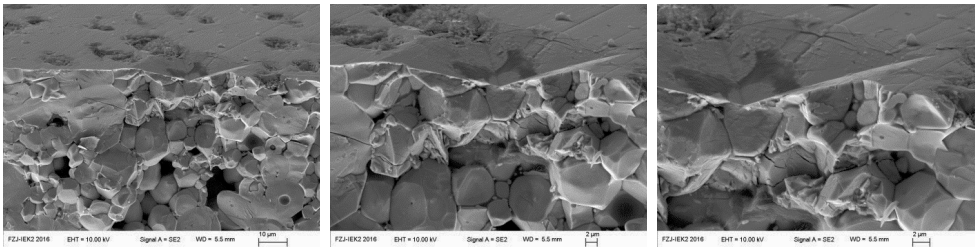

Figure 4.20- SEM micrographs of indented cross-section of 40Ta:LLZO-16h.

Table 4.11- Summary of 40Ta:LLZ specimens, average crack length, *l*/*a* ratio and K_{IC}.

Specimen	Average crack length l (µm)	l/a	K_{IC} (MPa·m$^{0.5}$)
40Ta:LLZ-4h	13.9 ± 5.0	1.6	1.13 ± 0.2
40Ta:LLZ-8h	8.6 ± 0.6	1.1	1.30 ± 0.05
40Ta:LLZ-16h	10.8 ± 2.4	1.1	1.35 ± 0.04

Looking in detail at Table 4.11, the crack length measurement for 40Ta:LLZ sintered for 4 h is highly affected by porosity leading to an uncertainty of ~35%. The ratios of l/a ranged from 1.6 to 1.1 and the fracture toughness slightly decreases with increasing porosity. Considering the grain size, the K_{IC} calculated here can be considered as global properties and therefore strongly affected by the local microstructure and porosity.

Crack paths

Figure 4.21 illustrates two different crack patterns, the image a) shows a cracks emanating from the corner and growing trough the grain with different chemical composition in the center, confirmed by EDX in Figure 4.22. Some grains showed a tantalum concentration in the center. Such effects were not observed for the Al doped materials variation. Even though the crack shapes are influenced by the local chemical composition, no systematically influence was observed for crack length or K_{IC}. Figure 4.21 b) reveals a different crack pattern; crack grows evenly from the corner trough another grain.

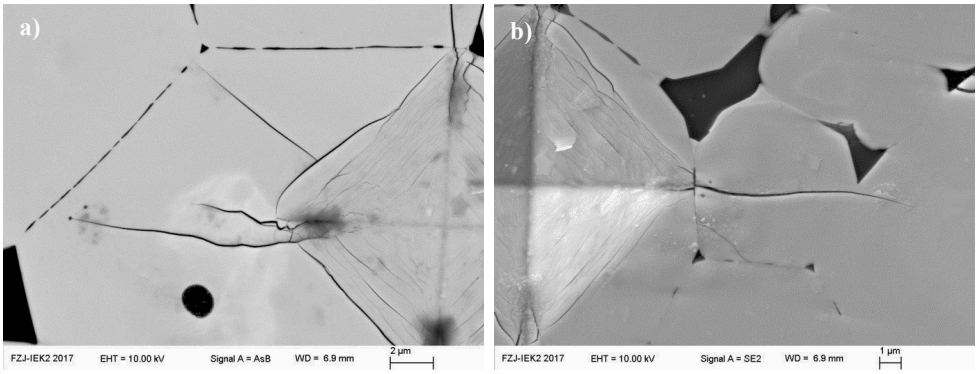

Figure 4.21- Cracks on 40Ta:LLZ-16h, indentation load of 1 N a) affected by local chemical composition, b) not affected by chemical composition.

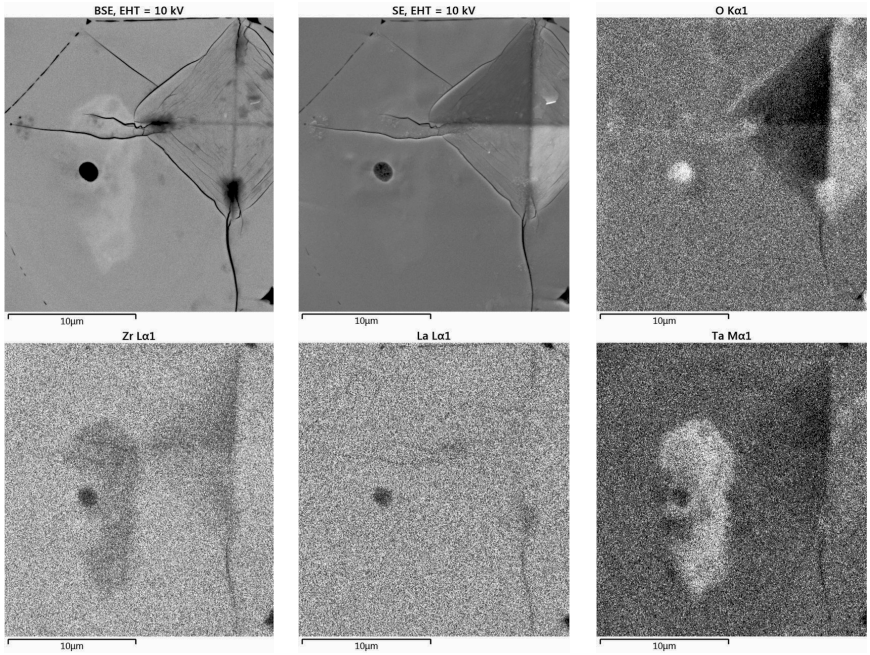

Figure 4.22- EDX mappings of the previous indentation affected by two indentations presented in previous figure.

The cracks path was also studied in more detail near the grain boundaries. Mostly, the cracks propagate along the grain, but also along the grain boundaries, revealing the presence of both failure modes, transgranular and intergranular. Overall, transgranular crack mode was predominant, indicating that the material may be weaker than the grain boundaries. Figure 4.23 shows a crack growing through a grain, very close to a grain boundary. In fact, the propagating crack also changed direction due grain boundaries, crack deflection, indicating that regarding the crack path also the angle of the grain boundary with respect to the growing crack plays a role. All these effects will potentially gain enhanced importance in the case of operated materials, that should be the aim of forthcoming studies.

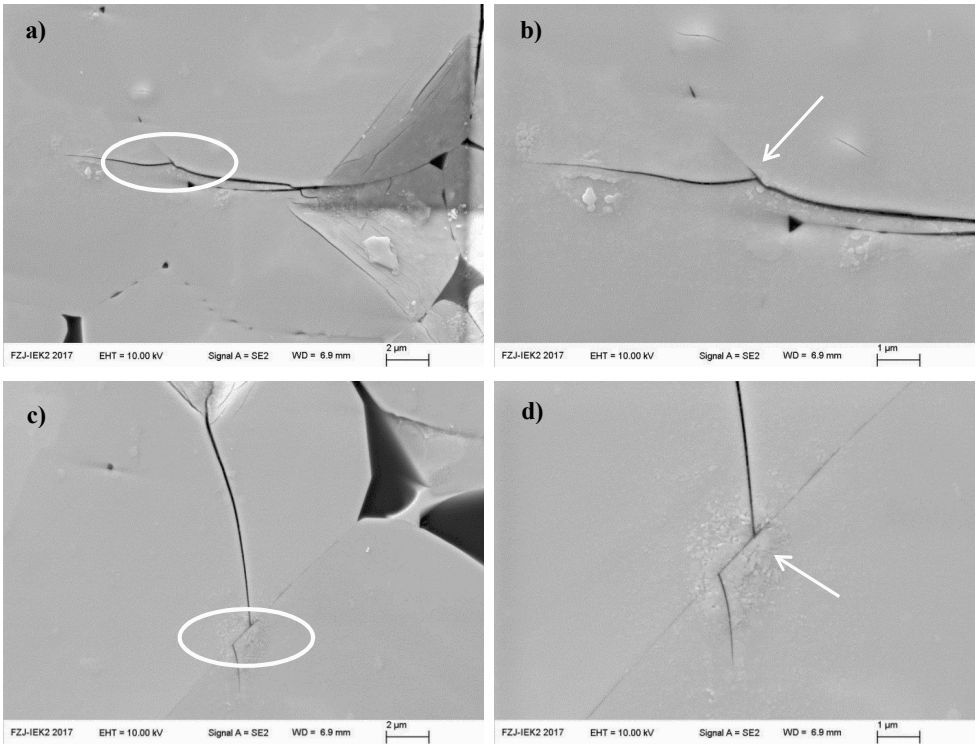

Figure 4.23- Cracks paths after Vickers indentation at 1 N of 40Ta:LLZ-16h.

4.1.5. Moisture associated degradation

Understanding the stability of LLZO is crucial for the development of next generation solid-state batteries, especially the morphology and surface chemistry related changes when exposed to air. Recent works demonstrate that LLZO certainly reacts with species in ambient air, which can affect directly the interface resistance [155, 158, 169]. Sharafi et al. investigated theoretical and experimentally the impact of air exposure on the Li-LLZO interface [155]. First, LLZO reacts with humidity in the air and via LLZO protonation, LiOH is formed as intermediate compound. Subsequently, LiOH reacts with CO_2 in air and converts to Li_2CO_3. Such compounds can result in topography changes and non-uniform contamination layer on the surface of LLZO, which depends on the exposure time [155]. Figure 4.24 and Figure 4.25 are microcopy images of Ta and Al-substituted LLZO surfaces exposed to air.

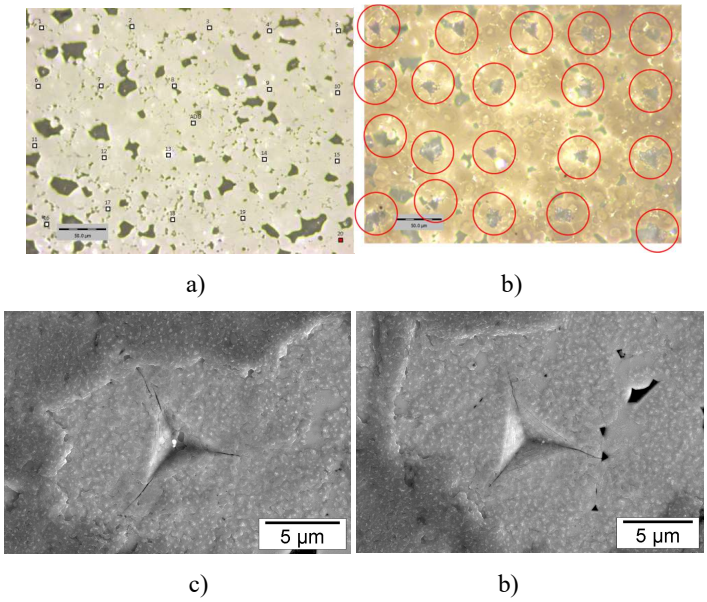

Figure 4.24- Microscopy images of 40Ta:LLZO a) and b) optical images of surface before and after testing in air, respectively; c) and d) higher magnification SEM micrographs of Berkovich imprint at 100 mN, immediately transferred to SEM after mechanical testing.

To ensure that the surface is free of contamination before mechanical testing, the samples were polished with water-free polishing suspension and immediately moved to the vacuum chamber for indentation testing (CSM; Anton Paar with a Berkovich tip). In Figure 4.24 a) and b) it is possible to note the position of indentations marks on surface before and after testing in air. Due to the contamination layer and rather porous microstructure, it is challenging to identify and evaluate the indentations marks after testing. Therefore, the tests were performed in vacuum. However, even though the tests were performed in vacuum, the transfer from the mechanical device to SEM with sample being exposed very shortly to air was enough to form a thin layer of probably Li_2CO_3 on the surface.

Figure 4.25 presents an image of an indentation mark immediately after test and after 2 weeks exposure to ambient atmosphere, to exemplify the materials behavior. Figure 4.25 a) shows an indentation image at 10 N with spallation, where the sample was immediately transferred from the mechanical testing device to the SEM vacuum chamber. Figure 4.25 b) and c) show indentation marks at 10 N after 2 weeks exposed in ambient atmosphere. In b) the lower magnification image shows the sample surface where the indentation marks are highlighted with red circles. Figure 4.25 c) shows an indentation at higher magnification, where the presence of a layer is clearly visible. According to literature, Li_2CO_3 on the surface can influence the interfacial impedance, decrease the ionic conductivity and have important implications for the operation of solid-state batteries [158].

In order to elucidate the influence of air exposure on the mechanical properties, testing using the nano-indentation system was carried out on exposed surfaces in this work. In order to address the layer effect on the mechanical properties, very low loads were applied at very shallow depths (0-100 nm), however, due to the softness of the layer the first contact of the indenter to surface was not recognized by the software and no load-displacement curve could be properly achieved. Hence, overall the results are inconclusive and therefore not discussed here in detail. Therefore, the specific effect on the mechanical properties remains currently unknown and can be a topic for future investigations.

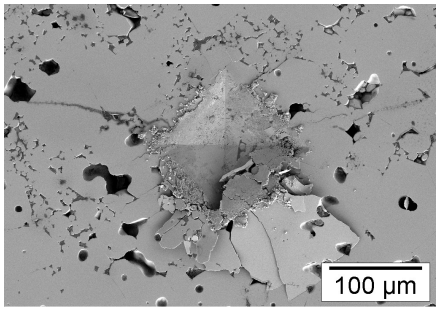

a)

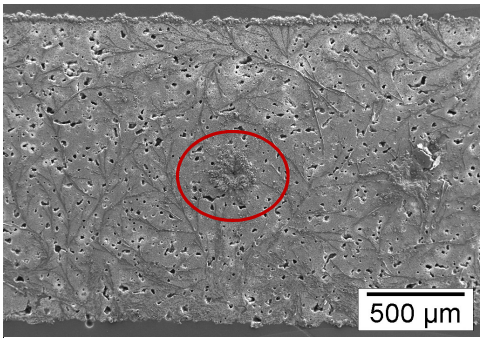

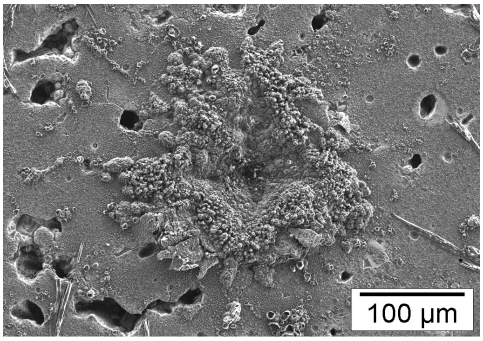

b) c)

Figure 4.25- SEM micrographs of Vickers indentation imprints at 10 N on 20Al:LLZO a) immediately after testing; b) and c) after 2 weeks exposed in ambient atmosphere, low and high magnification, respectively.

4.2. Fracture toughness Al-substituted $Li_7La_3Zr_2O_{12}$ (Al:LLZO) by utilizing micro-pillar indentation splitting test

In this section, the presented investigations focus particularly on the acquisition of knowledge of local and global mechanical properties exemplified for the high conductivity Al-substituted LLZO electrolyte material. A novel method based on micro-pillar indentation splitting is introduced and applied for the first time on this material to assess the microscopic fracture toughness within individual Al-doped LLZO grains and compare it with data derived from the conventional VIF method as measure of the macroscopic fracture toughness. Results on the material investigated in the present section were already reported in section 4.1 and its properties were generally discussed and compared in terms of dopant effect. In this section, the properties are discussed in more details based on the improved approach with main focus on the fracture toughness.

4.2.1. Conductivity, phase composition and microstructure

The composition chosen in this particular substudy was Al-substituted $Li_7La_3Zr_2O_{12}$ (Al:LLZO). It was characterized using the techniques given in the experimental section to assess some microstructure and conductivity related reference properties to aid concice interpretation of subsequent mechanical testing results. The respective reference data are summarized in Table 4.12. The composition was characterized using ICP-OES, and the crystalline structure was obtained from XRD (Figure 4.26). Table 4.12 shows that the Li concentration after the sintering process is still larger than expected (Li = 6.61), which is probably due to the incomplete removal of the 15% excess of $LiOH{\cdot}H_2O$ and precipitation of LiOH and Li_2CO_3 at the grain boundaries as determined previously in another study [144]. The effect of Al doping, where a Li site is occupied by Al, results in a stabilized cubic structure of LLZO with an increasing degree of vacancy disorder within the Li sub-lattice [170, 171]. The XRD pattern in Figure 4.26 reveals a mixture of cubic and tetragonal phases for this Al:LLZO, as was observed from the overlapping peaks concerning the ICDD standards, and around 50 wt% of tetragonal phase, which was estimated via Rietveld refinement method.

Table 4.12- Summary of composition, structure, relative density and conductivity.

Sample	Compositions [ratio]				Structure [Cubic to tetragonal ratio]	Grain Size [µm]	Relative Density [%]	Conductivity [S/cm]
	Li	La	Zr	Al				
Al:LLZO	6.91	3.00	1.98	0.13	~ 1:1	~100	93	2.08×10^{-5}

Because of the close similarity of the structures and atomic densities of each element, the phase ratio is only provided as an indication to illustrate that the cubic stabilization is warranted by adding Al. Associated with this, the reported conductivity of 2.08×10^{-5} S/cm is in between the experimental results of conductivity of tetragonal LLZO (~ 1×10^{-6} S/cm [84, 171-173]) and those of cubic LLZO (~10^{-4} to 10^{-5} S/cm) [144, 168, 170, 171, 174], which can be attributed to the existence of the cubic LLZO structure. The microstructure obtained via SEM is illustrated in Figure 4.27 (a) and (b), which shows a typical micro-pillar before testing. The average grain size was approximately 100 µm, and the relative density of 93% permitted by careful choice of testing position, mechanical tests to be performed for apparently dense areas, permitting hence a basis for comparison of obtained results.

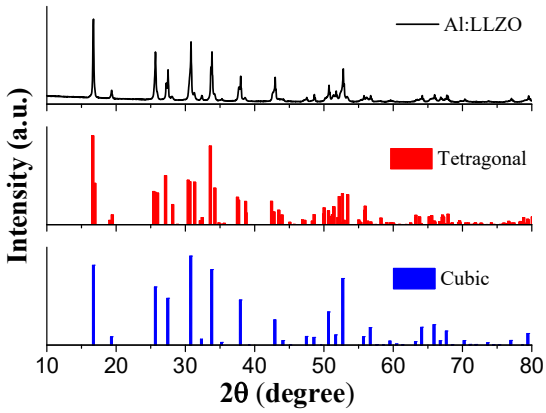

Figure 4.26- XRD pattern of specimen Al:LLZO. The cubic and tetragonal LLZO structures were identified with respect to the ICDD JCPDS card number 99-000-0032 and 99-000-0020, respectively.

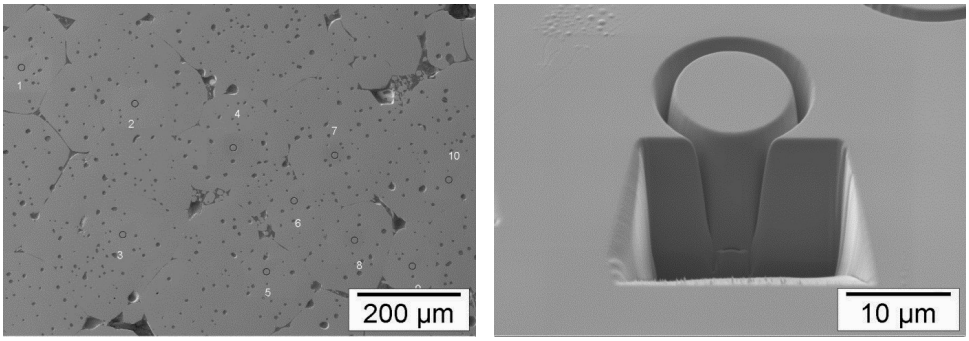

a) b)

Figure 4.27 - SEM topographies: (a) specimen surface and the selected areas for micro-pillar testing, and (b) micro-pillar.

4.2.2. Mechanical testing results

Table 4.13 and Figure 4.28 present Young's modulus (*E*) and hardness (*H*) obtained from the depth-sensitive indentation on the polished cross-section. The elastic modulus is rather constant, whereas the hardness reveals a reproducible decrease with increasing load. The scatter in the individual depth-resolved profiles indicates that via the selection of an appropriate position, the potential influence of grain boundaries, structural defect and inhomogeneity or indentation size effects can be avoided or included, similar as discussed above. The individual continuous multi-cycle indentation tests are illustrated in Figure 4.28 (a) and (b), corresponding to Young's modulus and hardness as a function of the indentation depth, from which the average values were calculated and plotted in Figure 4.28 (c).

As mentioned, the Young's modulus is rather stable, whereas the hardness decreases already above 0.8 µm probably associated porosity or even with an indentation size effect. Although an extent of an indentation size effect to a depth of more than 2 µm appears to be unusually, the rather large grain size has to be considered, i.e. grain size effects onto the extend of the indentation size effect have also been reported in literature [108, 175, 176]. The data were verified by single load-unload cycle indentations at depths of ~ 1900 nm yielded an elastic modulus of 140 ± 9 GPa and hardness of 7.6 ± 0.8 GPa, hence, agreeing with the CMC values within the limits of experimental uncertainty.

Table 4.13- Comparison of mechanical properties, hardness, Young's modulus and fracture toughness.

Sample	Young's modulus[GPa]	Hardness [GPa]	Fracture toughness [MPa·m$^{0.5}$]			
			1 N	3 N	5 N	Micro-pillar Splitting
Al:LLZO	145.6 ± 7.3	8.5 ± 0.4	1.19 ± 0.13	1.19 ± 0.22	N.A.	0.99 ± 0.05

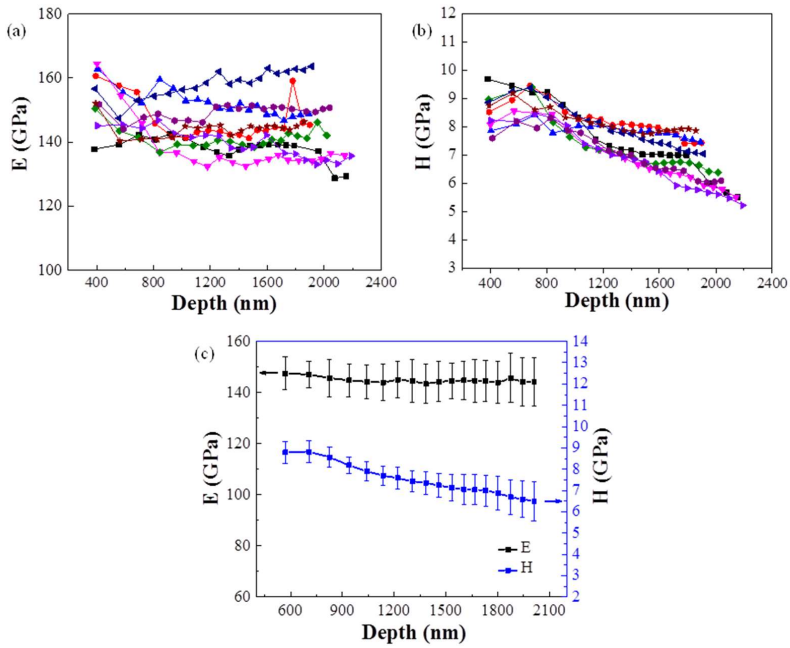

Figure 4.28- (a) Young's modulus (*E*) and (b) hardness (*H*) obtained from 9 individual CMC tests, and (c) the average *E* and *H* values as a function of the indentation depth.

Note that, due to the rather large grain size compared to the elastic zone and especially also plastic zone, Young's modulus and hardness should not be affected by changes in properties that might be associated with different properties of grain boundaries. Taken from a stable region of the average elastic properties vs. depth plots (Figure 4.28 (c)), the material properties were determined, which is a similar procedure as has been used to analyze properties of for example thermal barrier coatings [177]. As materials properties, the average Young's modulus and hardness up to 0.8 µm

were considered and values of 146 ± 7 GPa and 8.5 ± 0.4 GPa were obtained, respectively. Both values agree with the experimental and ab-initio calculation results from literature and with the results given above in the section 4.1.2 where the effect of the sintering time and hence porosity was addressed.

Typical Vickers indentation imprints in the Al:LLZO specimen are shown Figure 4.29; loads of 1, 3 and 5 N were applied to generate radial crack pattern for K_{IC} determination, the corresponding K_{IC} results are presented in Table 4.13. In this case, in order to work with only one parameter variation at the time and having a single composition under investigation, the load was varied to investigate an apparent fracture toughness load dependency

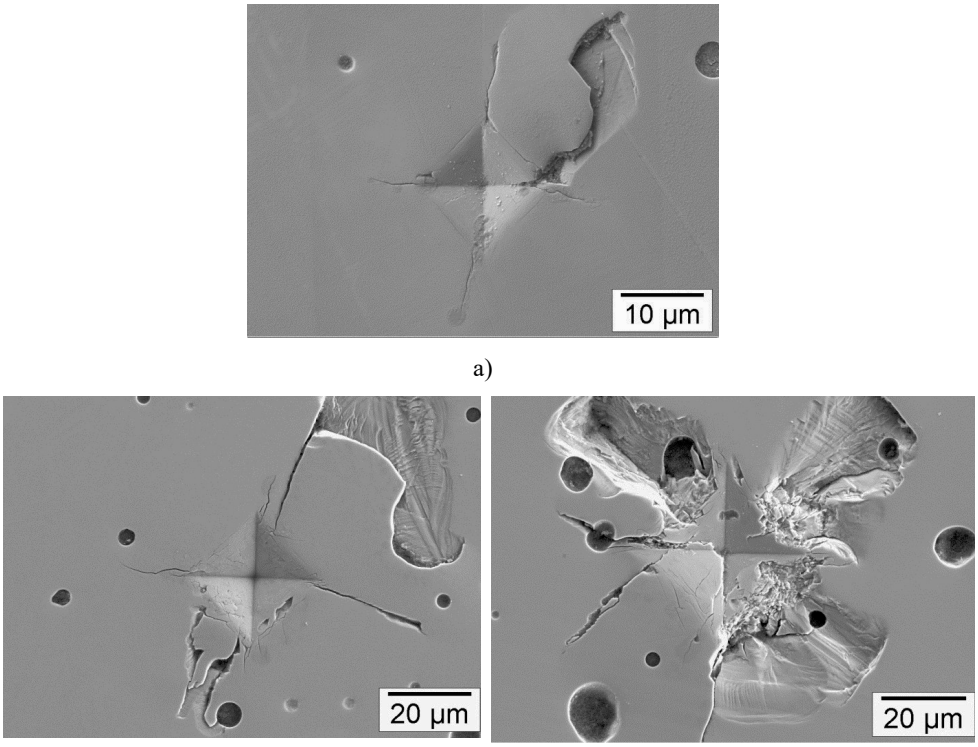

Figure 4.29- SEM micrographs after indentation imprints after applying loads of (a) 1 N, (b) 3 N and (c) 5 N, respectively.

l/*a* ratios of approximately 1.2 and 1.4 were obtained for the considered loads and complimentary FIB analyses endorsed the criteria of fracture toughness evaluation using Palmqvist crack model [114], similarly as in section 4.1.4.

Despite of selecting visibly pore-free regions, the resultant radial cracks exhibited asymmetrical lengths and spallation between some cracks for all three different loads. Especially at 5 N materials chipped off from the side of the impression. Hence, for this load it was not possible to evaluate the fracture toughness. Even for the lower loads (1 N and 3 N), the determination of crack lengths was difficult due to the chipping effects that appeared at least for one of the cracks and, even though the chipping probably only occurred on unloading, the toughness results can only be considered as estimate of the materials behaviour, that needed confirmation by an additional testing method. However, overall the calculated fracture toughness results revealed no significant dependence on the applied load, hence, indicating that the used relationship is appropriate for the considered crack type.

A clearer SEM image of the crack morphology after applying a load of 1 N is shown in Figure 4.30 (a), in order to investigate the effect of potential structural defects that might exist underneath the indentation imprint and verify the Palmqvist crack type for K_{IC} analysis. In this case FIB cuts were carried out for the longest radial crack observed for a particular indent along the positions where the crack began (P_1) and ended (P_2) as depicted in Figure 4.30 (a). The crack depth was measured and plotted vs. the distance from (P_2) to obtain the subsurface crack trajectory, from which the type of crack and the influence of pre-existing structural defects was envisaged to be assessed.

From location P1 to 1 µm before location P2, two different types of cracks, containing one main Palmqvist crack parallel to the sample surface and another spallation crack perpendicular to the surface (Figure 4.30 (b)), were found. A large closed pore of ~2 µm in radius appealed as the FIB cut reach 1 µm before location P_2 (Figure 4.30 (c)), where two additional spallation cracks were revealed, which are typical for crack types that are formed during unloading. However, it might also be concluded that the main apparent Palmqvist crack arrested locally by the pore in the vertical direction.

At higher loads, the influence of porosity and structural inhomogeneity could lead to more structual

damage that could affect the formation of radial cracks. Even though verified only for one example crack, the investigation shows that the pore might strongly affect the crack depth. Looking at Figure 4.30 (d), the pore location is highlighted by dash circles; apparently the crack continued below the pore just with a change of direction, i.e. the pore caused no crack deflection.

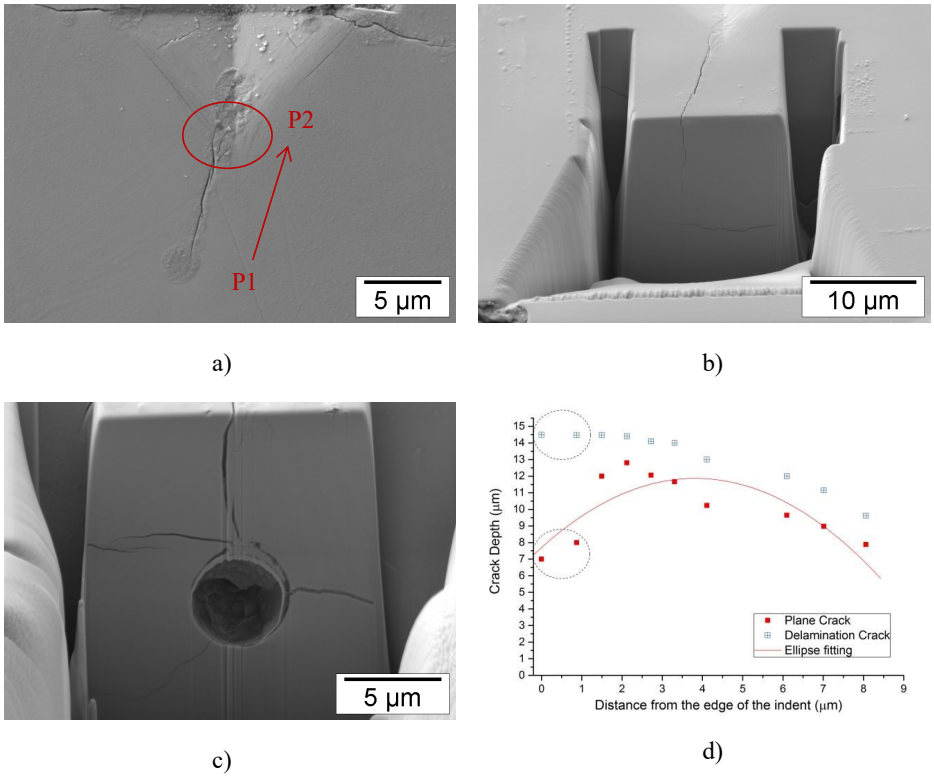

Figure 4.30- SEM micrographs of sample morphology after applying VIF test (a) selected crack for investigation: P_1 is the end of the imprinted, P_2 indicates 0 µm from the imprinted tip and red arrow indicate the direction of the FIB cutting (b-c) the extended cracks obtained from several SEM-FIB cross sectional, where the position P1 and P2 were located at the beginning and the end of the extended cracks. The crack depth vs. distance from the FIB cuts are plotted in (d), and the dash circle indicates the location of one large pore (radius ~ 2 µm).

As the load was increased from 1 to 3 N, the fracture toughness remained 1.19 MPa·m$^{0.5}$; while the standard deviation increased from 0.13 to 0.22 MPa·m$^{0.5}$, which could be a result of crack length measurement uncertainties. The relationship for median-radial crack system appears not to be appropriate, based on the crack length to imprint ratio of 1.2 and 1.4 for 1 and 3 N, respectively, and the complimentary FIB analyses that was discussed above. However, even though not being appropriate on the basis of the crack shape, using for example the relationship derived for the median-radial crack shape [115] results in values of 1.01 and 1.02 MPa·m$^{0.5}$ for the current material for the loads mentioned above, hence still being in rather good agreement with the data derived above and verifying that the derivation of values for the currently tested material is not very sensitive with respect to the indentation crack analysis procedure.

Comparing the VIF results at 1 N obtained here with VIF results in the previous section, where the porosity was the main aspect, the fracture toughness values for samples with similar densities and grain sizes are in general agreement, i.e. here 1.19 ± 0.13 MPa·m$^{0.5}$ and 1.40 ± 0.10 MPa·m$^{0.5}$ in the previous section.

Aiming at verification and advancement of fracture toughness testing procedures with particular emphasis on local testing of grain and optionally grain boundary, the micro-pillar test was implemented for the current material. Figure 4.31 (a) shows the load-displacement curve of five micro-pillar indentation splitting tests and Figure 4.31 (b, c, d, e) present as a representative selection the corresponding SEM-FIB images of pillars A and B after testing.

A clear pop-in effect due to cracks formation that led to sudden displacement jumps in the force-displacement curve is visible at the individual critical loads (P_c), in the range of 34 to 39 mN. Looking at two pillars in more detail, for pillar A only one pop-in associated kink was found, whereas several additional kinks were found for pillar B after the critical load was exceeded, indicating additional secondary crack formation as the load increased, as also verified in Figure 4.31 (c) and (e).

Since the pillar splitting method only considers the necessary energy and load to initiate / propagate cracking, additional secondary cracks forming as the critical load is exceeded will not influence the derived fracture toughness. Also, the trajectory of the crack did not encounter with any structural defects, such as grain boundaries or pores which might affect the results in terms of

already reducing the load to initiate the fracture, and hence the resultant toughness can be considered as the intrinsic materials value of single crystalline Al:LLZO.
It is also important to mention that the cracks don´t always initiate from the edge of the residual imprint, as can be observed in Figure 4.31 (b, d). This might be result of a possible anisotropy in the mechanical properties or surface effects, which, although not being possible to investigate within the framework of the current work, is the focus of a complementary study that is currently ongoing in the section.

Another relevant issue is that, different from other in-situ experiment set-ups [133], the precise position of the indenter at the centre of the pillar was manually corrected, which might lead to an indentation slightly off-centre, as observed in Figure 4.32 pillar C. Despite this fact, no significant influence on the critical load was observed considering that the indenter´s positioning accuracy was within the limit of be approximately 20% of the target pillar's diameter, which agrees with results presented in a recent literature study [132].

From all tests, see Table 4.14, fracture toughness values ranged from 0.94 to 1.07 $MPa \cdot m^{0.5}$, with an average of 0.99 ± 0.05 $MPa \cdot m^{0.5}$, that can considered to be representative for the single grain property. The single grain toughness is in good agreement with global toughness obtained via VIF method (~1.19 $MPa \cdot m^{0.5}$), even though they are based on effects at different scales.

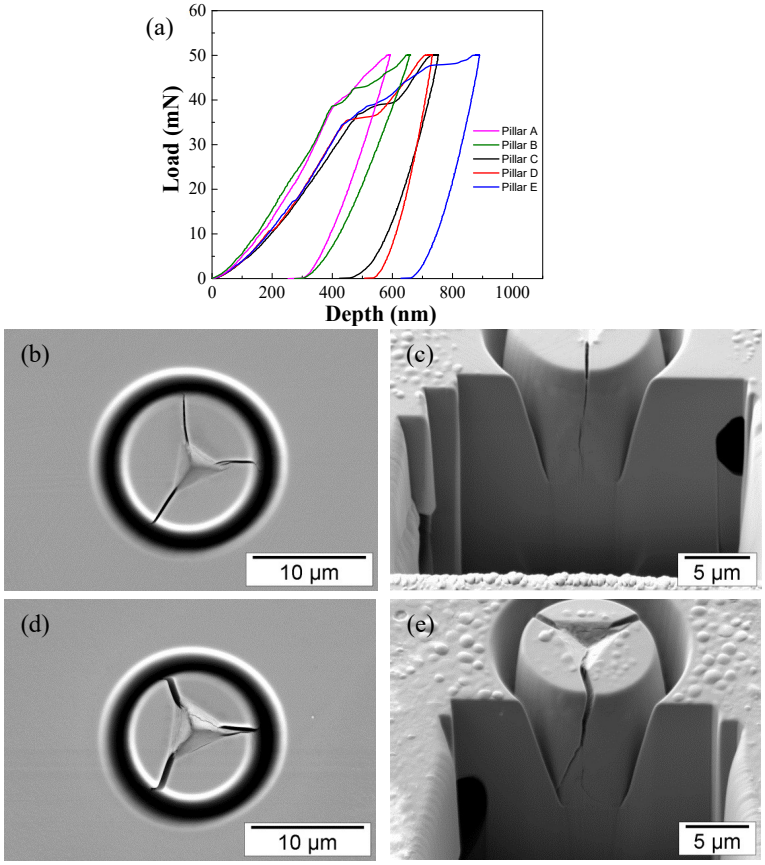

Figure 4.31- (a) Load-displacement curves of micro-pillar indentation splitting tests and some corresponding SEM-FIB images for (b), (c) front and side view of pillar A and (d), (e) front and side view of pillar B. It is worth notice that a blister-like surface morphology was only observed after further FIB milling for topological observation in (c, e). A featureless surface morphology was observed in (b, d) during and immediately after indentation.

In literature, large differences in derived fracture toughness values have been reported for the considered material (see Table 2.3), being in the range from 0.86 to 2.37 MPa·m$^{0.5}$. Although a dependency on the chosen relationships cannot be ruled out, microstructural features in particular changes in fracture mode appear to be the main reason for this large data range. Considering only transgranular fracture, similar as in the current study, the range reduces to 0.86 to 1.63 MPa·m$^{0.5}$.

In addition, although transgranular fracture was reported, the very large difference in grain size compared to our study, associated with different sintering conditions, does not permit a direct comparison with these literature data.

Table 4.14 - Summary of micro-pillar indentation splitting test results.

Pillar No.	Radius [µm]	Critical load [mN]	Fracture toughness [MPa·m$^{0.5}$]	Average Fracture toughness [MPa·m$^{0.5}$]
A	5.3	39.2	1.00	
B	5.0	38.6	1.07	
C	5.1	36.9	1.00	0.99 ± 0.05
D	5.2	35.5	0.94	
E	5.0	34.4	0.95	

To investigate any effects related to a potential influence of Ga-ion damage on the pillar splitting testing result, a qualitative compositional study was performed via EDX on one of the tested pillars, i.e. C in Figure 4.32. The resulting Ga concentration was less significant in the centre of the pillar compared to the boundaries as derived from the relative peak intensities of Ga $L\alpha_{1,2}$ peak and mostly localized at the FIB milled surfaces far away from the crack initiation / propagation region. Therefore, the Ga-ion damage is expected to be less significant than in the case of other micro-mechanical tests, in particular the micro-cantilever method, as also illustrated in [133, 179-181]. It is worth mentioning that the severe surface contamination was only observed after FIB milling for topological observation as shown in the Figure 4.32 (d, e). The blister-like surface morphology could be a result of extensive reaction between the Ga-ion leading possibly to formation of $Li_{6.43(2)}Ga_{0.52(3)}La_{2.67(4)}Zr_2O_{12}$ via Ga substitution [182], and a local volume / crystalline symmetry alteration could then be responsible for this surface damage.

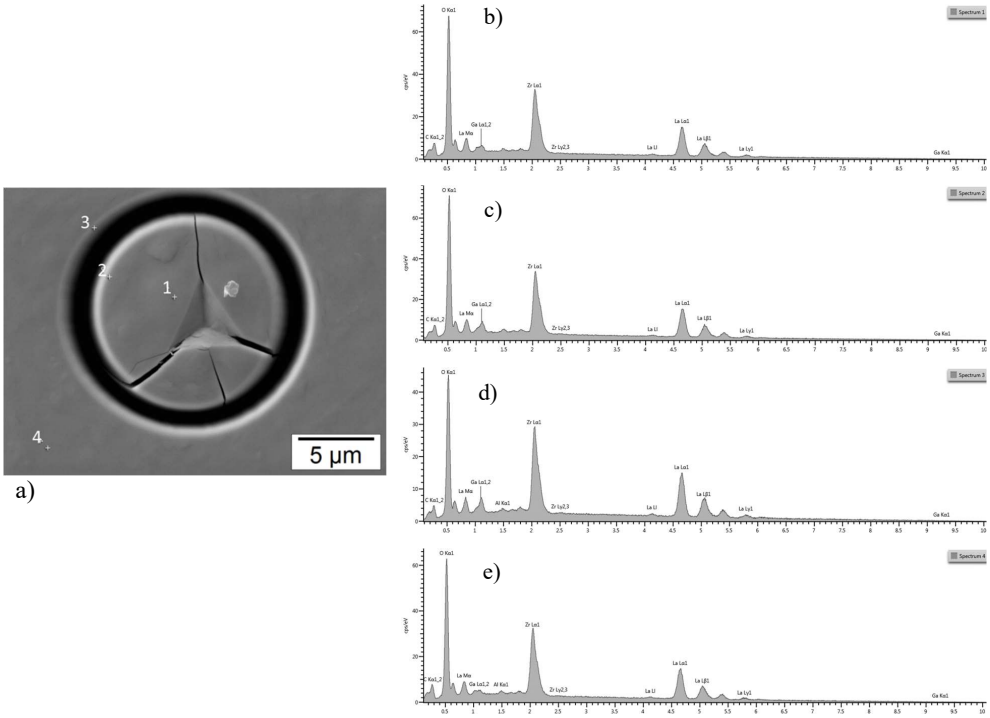

Figure 4.32- (a) SEM micrograph and EDX composition analyses at different location around pillar C, (b) location 1, (c) location 2, (d) location 3 and (e) location 4.

4.2.3. Conclusions and outlook

The last section presented, aiming towards an advancement of the fracture toughness derivation methodology, a mechanical property assessment of an Al doped LLZO garnet structured material by using indentation micro-pillar splitting tests with a comparison to conventional indentation testing results. In addition, elastic modulus and hardness were accessed as functions of penetration depth using indentation. Mechanical properties were evaluated at 800 nm depth, elastic modulus and hardness are 145 ± 7 GPa and 8.5 ± 0.4 GPa, decreasing at higher indentation loads to values that represent global properties. The single crystal representative fracture toughness value obtained via micro-pillar splitting tests is 0.99 ± 0.05 MPa·m$^{0.5}$, which is in good agreement with global VIF fracture toughness 1.19 MPa·m$^{0.5}$ obtained in the current section, a direct comparison with

literature results is not possible due to large grain size differences possibly associated with different sintering conditions. Compared with the fracture toughness with Al-doped LLZO sintered for 40 h with similar posority from the previous section, the VIF was 1.40 ± 0.10 MPa·$m^{0.5}$, the values agree in within the limits of uncertainty.

Although a slight bias at low loads cannot abolutely be ruled out, the results indicate that mainly at loads exceeding 3 N, a fracture toughness determination is not possible anymore for the current materials due to the excessive chipping. Furthermore, it reveals potential sensitivity of the VIF testing method to local effect such as pores and, hence, emphasizes the advantages of the pillar testing method.

Overall, the results indicate that the micro-pillar splitting method can be used to acquire the fracture toughness representing a basically pore-free material even on the basis of testing a slightly porous materials' variation (7% porosity in this study). Even though the envisaged fully dense form cannot be reached in an experimental preparation procedure, the micro-pillar splitting method permits locally resolved materials property analysis (see Figure 4.27) and shows significant benefits with respect to the accessibility on battery materials. The establishment of the Al:LLZO single crystalline fracture toughness can also be a basis for future development based on assessed local fracture toughness values for samples with compositonal variations, smaller grain size and samples after long-term operation, which are envisaged to be the focus of forthcoming studies.

4.3. Hot pressed LLZO

This section of the thesis is a contribution to an ongoing study performed in collaboration with Ms. Yulia Arinicheva at IEK-1. The contribution regarding the thesis work are an assessment of potential grain size dependencies of mechanical properties, in addition it concentrates on the complementary aspect of grain size dependencies of ionic conductivity. Hence, the current section focuses on the microstructural investigation and mechanical properties part of this joined study, where the main aim of this investigation is to elucidate the effect of Al doping and microstructural features of the $Li_{6.6}La_3Zr_{1.6}Ta_{0.4}O_{12}$ solid state electrolyte, aiming towards understanding and improvement its resistance to dendrite penetration. Al-doped and Al-free LLZO precursor powders with larger ~5 µm and nano-sized particles (larger grain size-LG and small grain size-SG) were synthesized via solid-state synthesis (SS) and solution-assisted solid-state synthesis (SASSR), respectively. An intrinsic improvement of LLZO solid-state electrolyte and lower interfacial resistance is expected for the specimens with smaller grains. SEM images in section 4.3.1 are given on the basis of the courtesy of partners in IEK-1. The outcome of this section permits, via consideration of the results presented in the previous sections, to gain also insight into effects related to the production process and dense materials sintered from hot pressed powders.

4.3.1. Conductivity, phase composition and microstructure

Figure 4.33 shows the SEM images of precursors powders obtained via conventional solid-state synthesis and solution-assisted solid-state synthesis, respectively. SS powder has particles size around 5 µm and SASSR powder possessed nano-particles size. Table 4.15 summarizes the microstructure information such as density, grain size and conductivity.

Figure 4.34 shows the microstructure of Al-doped LLZO synthetized via conventional solid-state synthesis (HP-Al:LLZO-LG) and solution-assisted solid-state synthesis (HP-Al:LLZO-SG). Figure 4.34 a) presents a microstructure with larger grains size in comparison to b), which shows rather smaller grain size and residual porosity.

Table 4.15 – Summary of specimen, density, grain size and conductivity.

Specimen	Density (%)	Grain size (µm)	Conductivity $\sigma_{25°C}$ ($S \cdot cm^{-1}$)
HP-Al:LLZO-LG	99.9	~ 5	$8.4 \cdot 10^{-4}$
HP-Al:LLZO-SG	99.1	~ 2	$7.8 \cdot 10^{-4}$
HP-Al free:LLZO-LG	99.8	~ 5	$7.8 \cdot 10^{-4}$
HP-Al free:LLZO-SG	99.5	~ 2	$7.0 \cdot 10^{-4}$

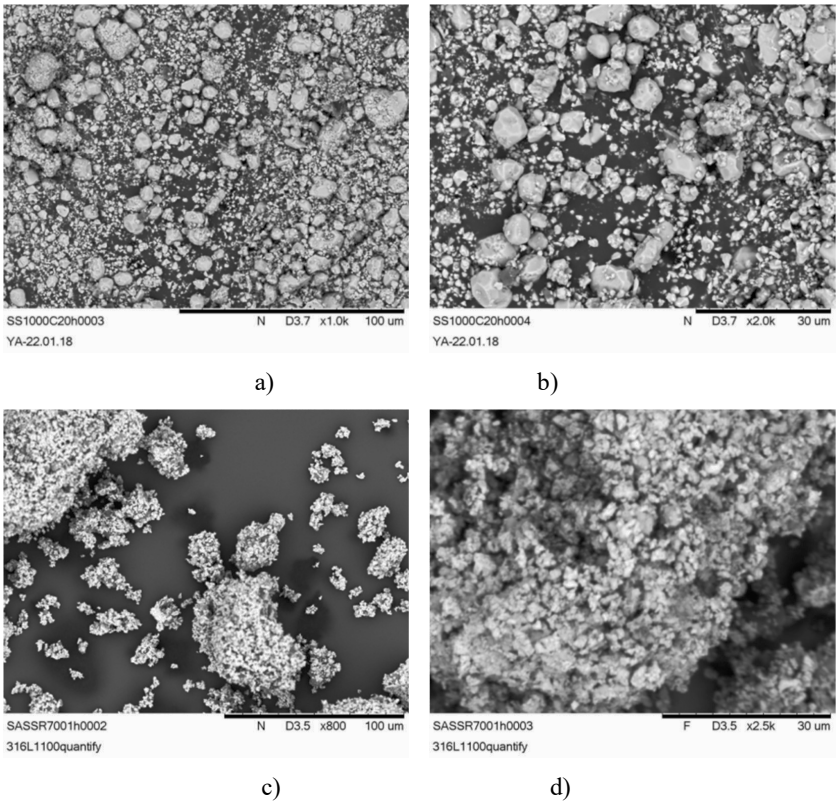

Figure 4.33- SEM micrographs of precursor powders a) and b) conventional solid-state synthesis (SS) and b) solution-assisted solid-state synthesis (SASSR).

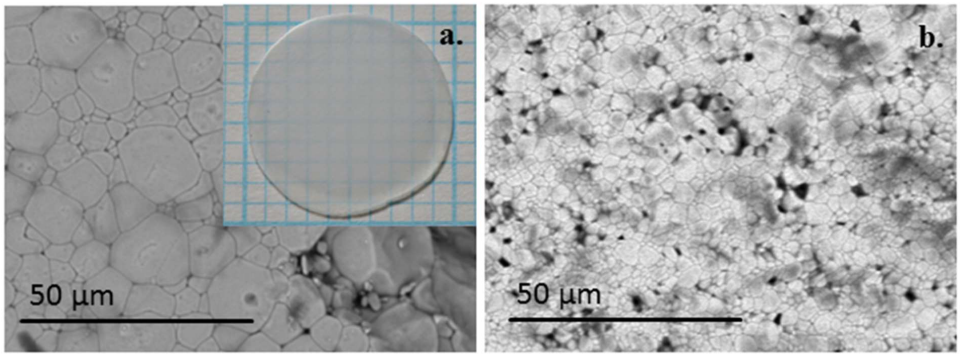

Figure 4.34 – SEM micrographs of hot-pressed Al-doped LLZO pellets a) Conventional solid-state synthesis HP-Al:LLZO-LG and b) Solution-assisted solid-state synthesis HP-Al:LLZO-SG.

Looking at the microstructure of HP-Al:LLZO-LG, it is possible to observe a range of grains sizes, varying from 2 to 25 µm with an average of ~ 5 µm, being a result of the powder production method. For HP-Al:LLZO-SG the grain sizes are rather homogeneous and range from 1 to 5 µm, with an average of 2 µm. Similar results are observed for Al-free samples processed via the same methods, hence, images are not given.

The XRD analysis of the sintered pellets revealed the formation of a pure cubic phase of the garnet type (space group Ia3d (230)), see Figure 4.35 a). The density of the sintered pellets is above 99% and the total conductivity of the sintered pellets, determined by means of electrochemical impedance spectroscopy (see Figure 4.35 b)), are in good agreement with literature values [143]. Conductivity values are summarized above in Table 4.15.

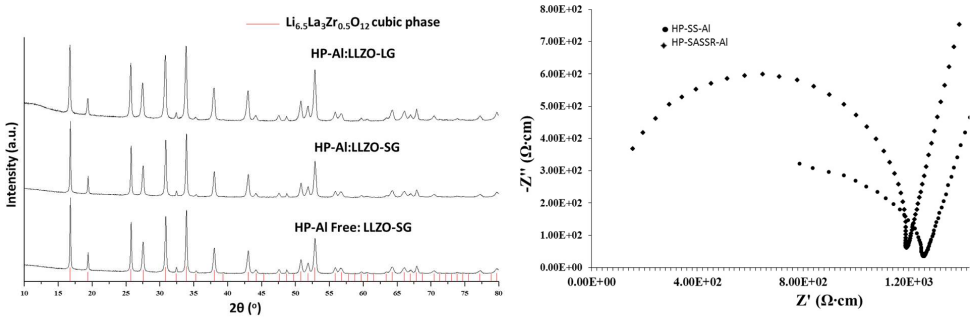

a) b)

Figure 4.35 – a) XRD patterns of HP:LLZO; b) Nyquist plot at 25 °C for HP-Al:LLZO-LG and HP-Al:LLZO-SG

4.3.2. Mechanical testing results

Figure 4.36 presents, as the average results of 25 indentations, the elastic modulus and hardness as a function of depth obtained from indentation testing for the different LLZO variations. Overall, the elastic modulus and hardness values are constant in the evaluated displacement range (0 to ~ 650 nm). It is assumed that a stable region of the average properties is around 500 nm, therefore the Table 4.16 summarizes the values at this penetration depth, which corresponds to the materials properties. No indentation size effect seems noticeable, since hardness values are constant for all samples. In some cases is noticed that hardness at shallow penetrations depths (0-200 nm) is slightly smaller than in other regions, this effect can be attributed to tip bluntness.

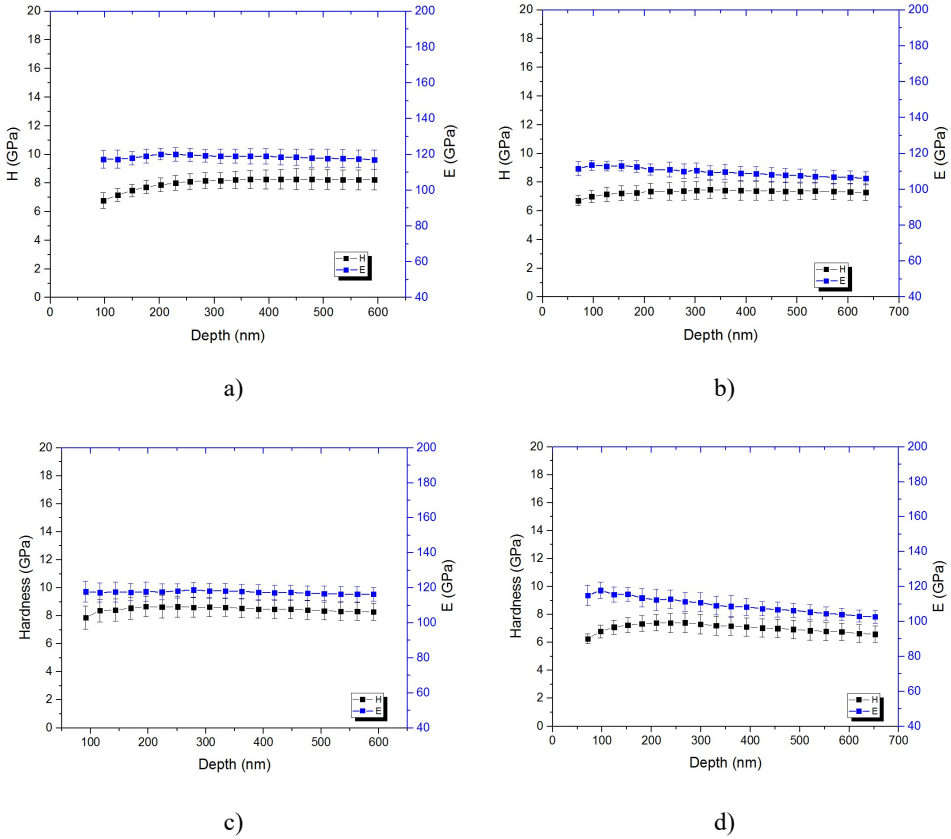

Figure 4.36 -Hardness and elastic modulus as function of penetration depth for a) HP-Al:LLZO-LG b) HP-Al:LLZO-SG c) HP-Al free:LLZO-LG d) HP-Al free:LLZO-SG.

Table 4.16 - Mechanical properties of HP-Al:LLZO at 500 nm depth.

Grains	Specimen	Elastic Modulus (GPa)	Hardness (GPa)
Larger grains	HP-Al:LLZO-LG	119 ± 5	8.2 ± 0.7
	HP-Al free:LLZO-LG	118 ± 4	8.4 ± 0.7
Small grains	HP-Al:LLZO-SG	108 ± 4	7.4 ± 0.6
	HP-Al free:LLZO-SG	106 ± 4	6.8 ± 0.7

Comparing the results for LLZO, larger grain sizes yield in both cases slightly higher values, for elastic modulus around ~20% and for hardness in both cases ~10 % and. Focusing on the aluminum doping, the results agree within the range of experimental uncertainty. Comparing the elastic properties with the ones from cold-uniaxial pressed material in the dopant effect section (section 4.1), similar composition 40Ta:LLZO with 9% porosity resulted in an elastic modulus of 124 ± 3 GPa, which is in good agreement with the results for the samples produced via hot-pressing. Hardness obtained previously is 9.8 ± 0.4 GPa, whereas hardness for specimens produced via hot-pressing is slightly lower.

Thus, the Al doping does not appear to have a pronounced effect on the mechanical properties. Comparing the elastic modulus obtained in this section with DFT (298 K) values from Table 2.3 in section 2.2.4.2 with similar composition $Li_{6.5}La_3Zr_{1.5}Ta_{0.5}O_{12}$ ~147 GPa, the values are ~ 20% smaller. Since the materials can be considered dense, such difference is unclear and it can be attributed to the processing method and intrinsic improvement of the material by the project partner.

4.3.2.1. Vickers indentation toughness

The fracture toughness was measured for all specimens using Vickers indentation applying loads of 0.5 N, 1 N and 3 N. Figure 4.37 shows SEM images of typical Vickers indentation imprints in the hot pressed LLZO after applying different loads.

For sample HP-Al:LLZO-LG the crack shape is straight, see Figure 4.37 a), and the fracture toughness is rather independent of the load in the range 0.5 to 1 N, within the limits of uncertainty. Similar behavior is observed for HP-Al free:LLZO-LG, Figure 4.37 c). At 3 N there are formations of various secondary micro-cracks, such an effect might be related to the high local stress field at 3 N, which led to formation of secondary cracks, is observed for all four specimens and does not permit accurate fracture toughness calculation at this load, since elastic energy is dissipated in the formation of secondary cracks. For HP-Al:LLZO-SG, the cracks are deflected along grain boundaries and stop at residual pores, see Figure 4.37 b) and Figure 4.38. HP-Al free:LLZO-SG, the cracks are more affected by residual porosity, especially at low loads, as can be been in Figure 4.37 d).

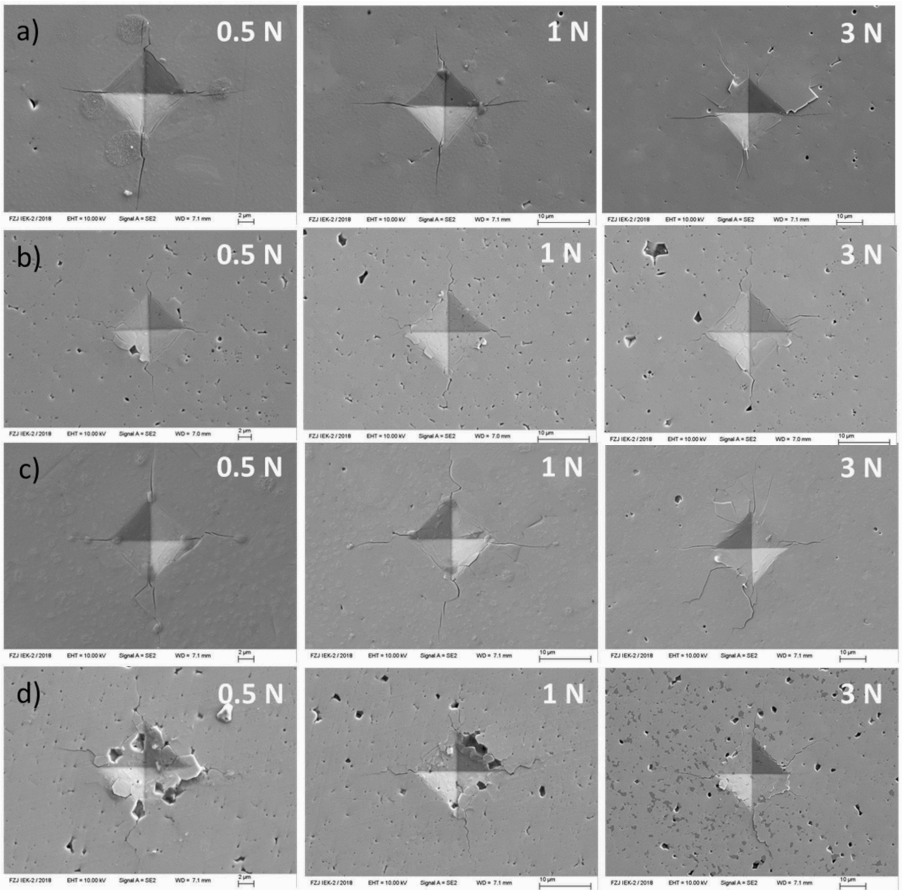

Figure 4.37- SEM micrographs of Vickers indentation imprints after loading to 0.5 N, 1 N and 3 N a) HP-Al:LLZO-LG b) HP-Al:LLZO-SG c) HP-Al free:LLZO-LG d) HP-Al free:LLZO-SG.

The average crack lengths (l), the ratio l/a from the SEM images and calculated K_{IC} are compiled in Table 4.17. Based on the crack length (l) and half diagonal (a) ratio, the Palmqvist crack system was selected for calculation (criterion $0.25 \leq l/a \leq 2.5$), similar as for the materials produced via cold pressed in the previous chapters.

Table 4.17- Vickers indentation toughness results for HP-Al:LLZO specimens.

Specimen	Load (N)	Average crack length l (μm)	l/a	K_{IC} (MPa·m$^{0.5}$)
HP-Al:LLZO-LG	0.5	6.4 ± 0.5	1.2	0.93 ± 0.05
	1	10.0 ± 0.7	1.3	1.07 ± 0.05
	3	20.0 ± 1.5	1.5	-
HP-Al:LLZO-SG	0.5	5.0 ± 0.5	0.9	0.95 ± 0.05
	1	7.4 ± 0.5	0.1	1.10 ± 0.05
	3	14.5 ± 0.5	1.3	-
HP-Al free:LLZO-LG	0.5	7.3 ± 0.9	1.3	0.86 ± 0.05
	1	10.2 ± 1.0	1.3	1.04 ± 0.08
	3	21.6 ± 1.7	1.5	-
HP-Al free:LLZO-SG	0.5	5.7 ± 0.6	1.1	0.83 ± 0.05
	1	12.4 ± 2.3	1.6	0.83 ± 0.10
	3	22 ± 2.5	1.5	-

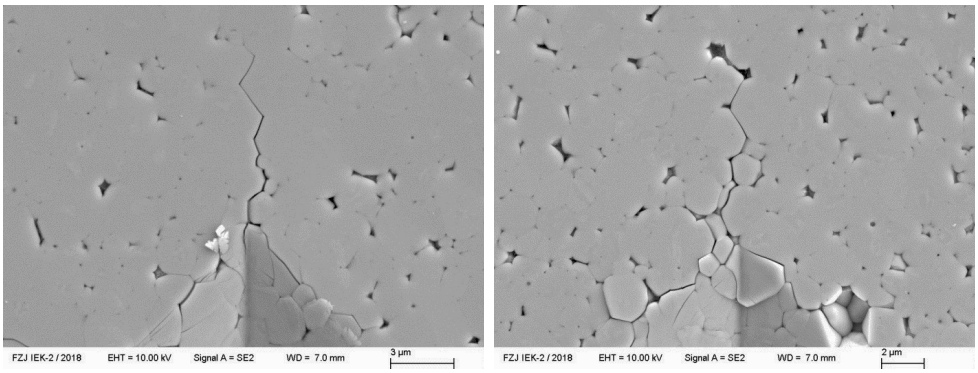

Figure 4.38- Crack deflection along the grain boundary sample HP-Al:LLZO-SG indentation load 1 N.

For sample HP-Al free:LLZO-LG, the crack is rather even when propagates through the grains, but at some point the propagating crack changed direction when encounter a grain boundary or is stopped and a new crack is generated, crack bridging, which leads to an increasing fracture toughness with load (an apparent R-curve behavior).

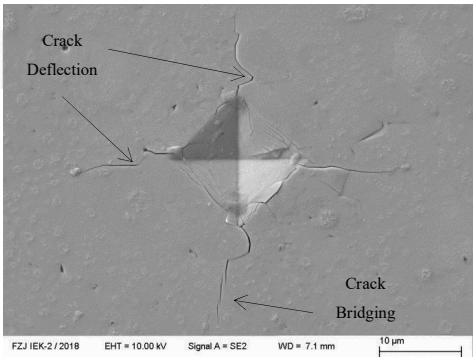

Figure 4.39- SEM micrographs of 1 N indentation highlighting crack deflection and crack bridging mechanisms in sample HP-Al free:LLZO-LG.

4.3.2.2. Micro-pillar splitting test

For the dense material micro-pillar testing was carried out as complementary technique, concentrating on one particular material for the small and large grain size variant. Figure 4.40 presents the load-displacement curve of five micro-pillars and respective SEM images of pillars with ~5 µm and ~10 µm diameter after indentation splitting test for sample HP-Al:LLZO-LG. The pillar diameter was varied in this advancement of the pillar testing methodology since a recent work investigated pillars size effects and their results indicated that a significant increase can occur in the apparent toughness at smaller pillars sizes due to influence of FIB damage and that the influence diminishes for pillar diameters ≥ 10 µm [132].

For the current experiments, the pop-in effect related to crack formation can be clearly observed in the load-displacement curve in Figure 4.40 a) and c) at critical loads ranging from 30.1 to 36.4 mN for pillar with ~ 10 µm diameters and 10.8 to 14.5 mN for pillar with ~ 5 µm diameters. Figure 4.40 b) and d) show the top view of micro-pillars after testing. The Young's modulus and hardness reported in Table 4.16 (ratio E/H ~ 14.5) were used to derive the dimensionless coefficient β (~0.27) for micro-pillar splitting fracture toughness calculations. The micro-pillar splitting test results of sample HP-Al:LLZO-LG are compiled in Table 4.18 and discussed below.

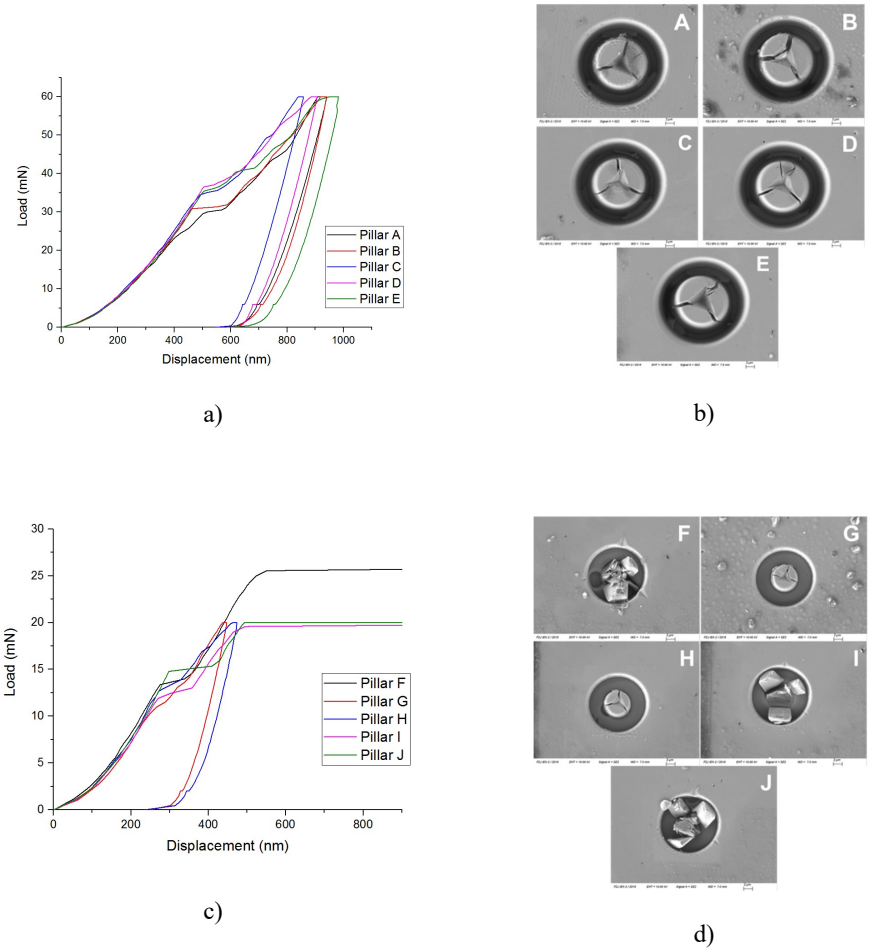

Figure 4.40- Load-displacement curves of micro-pillar indentation splitting tests and SEM front view of pillars after testing in sample HP-Al:LLZO-LG, a) load-displacement curves of pillar with ~10 µm diameter; b) SEM micrographs of pillars A to I after testing; c) load-displacement curves of pillar with ~5 µm diameter; d) SEM micrographs of pillars F to J after testing.

Table 4.18- Summary of micro-pillar indentation splitting test results for sample HP-Al:LLZO-LG, $\beta \approx 0.27$.

Pillar	Diameter (μm)	Radius (μm)	Critical load (mN)	K_{IC} (MPa·m$^{0.5}$)	Average K_{IC} (MPa·m$^{0.5}$)
A	9.85	4.93	30.1	0.74	
B	10.20	5.10	30.8	0.72	
C	10.10	5.05	34.5	0.82	0.80 ± 0.05
D	10.02	5.01	36.4	0.88	
E	10.15	5.08	35.3	0.83	
F	4.93	2.47	13.5	0.94	
G	4.81	2.41	12.7	0.92	
H	5.02	2.51	10.8	0.73	0.91 ± 0.09
I	4.90	2.45	13.0	0.92	
J	4.85	2.43	14.5	1.04	

The fracture toughness for pillars ~10 μm diameter ranged from 0.72 to 0.88 MPa·m$^{0.5}$ and for pillar with ~5 μm diameter it appeared to be higher ranging from 0.73 to 1.04 MPa·m$^{0.5}$. Looking at the final average, the fracture toughness of larger pillars is 0.80 ± 0.05 MPa·m$^{0.5}$ and for smaller pillars it is 0.91 ± 0.09 MPa·m$^{0.5}$. Even though the results agree within the limits of uncertainty, pillars with smaller size show a tendency towards higher fracture toughness values when compared to pillars with larger diameter, which is a similar effect as reported in literature for silicon [132]. This can be a result of gallium ion damage from FIB milling, which has been investigated via EDX for Al:LLZO-SG. As mentioned above, it was very recently reported that K_{IC} significant increased with decreasing diameter due to FIB damage on Si pillars, even though it has been suggested that this geometry is insensitive to FIB damage since the crack nucleates inside the pillar, far from the damaged free surface [132].

Since the grain size is the ranged 2 to 25 μm, pillars with 5 and 10 μm diameters were fabricated preferentially within single grains; therefore the obtained values can be associated with the intrinsic fracture toughness of Al- and Ta- doped LLZO single crystal. Comparing the with single crystal fracture toughness obtained at the previous section, where the VIF of 20Al:LLZO was 1.19 MPa·m$^{0.5}$ and from micro-pillar tests 0.99 ± 0.05 MPa·m$^{0.5}$, the calculated fracture toughness values for the current sample are in the same range.

In order to investigate the pillars after testing in more details, the pillar H (~5 μm diameter) was submitted to a cross-section FIB cut, see Figure 4.41, although the micro-pillar splitting test evaluation does not require any crack measurement. Looking at Figure 4.41, the crack trajectory was rather even and did not encounter any structural defects.

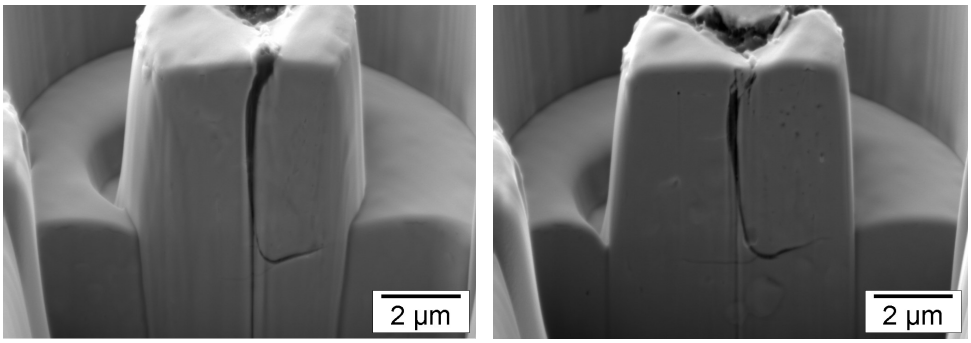

Figure 4.41- SEM micrographs of cross-sectional FIB cut of pillar H (~ 5 µm diameter) after indentation splitting.

The results for the second selected sample for micro-pillar testing concentrated on sample HP-Al:LLZO-SG with average grains size of 2-3 µm, which was used to fabricated pillar with 5 and 10 µm diameter, therefore the fracture toughness results are considered to be representative for polycrystalline material. Figure 4.42 a) and c) show the load-displacement curves for pillar with 5 and 10 µm and Figure 4.42 b) and d) SEM images of pillar after testing, in addition, Table 4.19 compiles the obtained results.

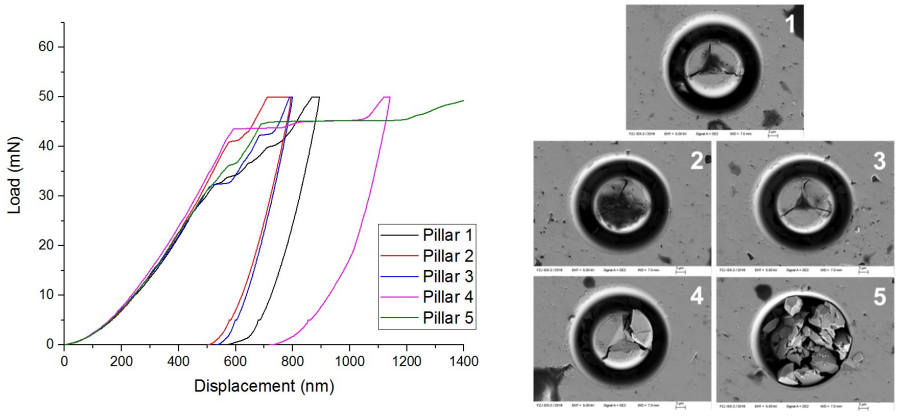

a) b)

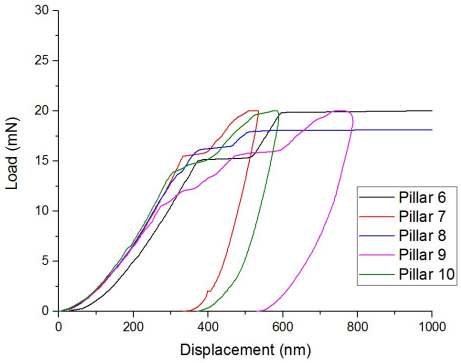

c)

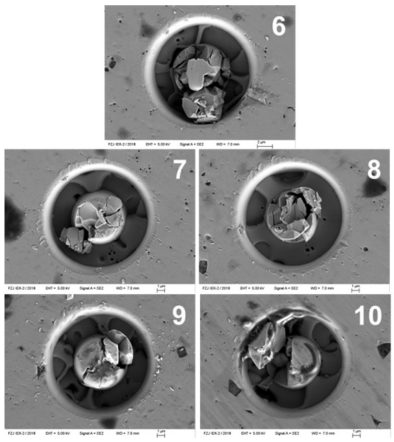

d)

Figure 4.42- Load-displacement curves of micro-pillar indentation splitting tests and SEM front view of pillars after testing in sample HP-Al:LLZO-SG a) load-displacement curves of pillar with ~10 µm diameter; b) SEM micrographs of pillars 1 to 5 after testing; c) load-displacement curves of pillar with ~5 µm diameter; d) SEM micrographs of pillars 6 to 10 after testing.

Table 4.19- Summary of micro-pillar indentation splitting test results for sample HP-Al:LLZO-SG, $\beta \approx 0.27$.

Pillar	Diameter (µm)	Radius (µm)	Critical load (mN)	K_{IC} (MPa·m$^{0.5}$)	Average K_{IC} (MPa·m$^{0.5}$)
1	9.25	4.63	32.3	0.88	
2	9.50	4.75	40.8	1.06	
3	9.80	4.90	32.2	0.80	0.96 ± 0.12
4	9.52	4.76	43.5	1.13	
5	9.71	4.86	36.2	0.91	
6	4.72	2.36	15.1	1.12	
7	4.50	2.25	15.4	1.23	
8	4.65	2.33	13.8	1.05	1.06 ± 0.15
9	4.70	2.35	10.6	0.79	
10	4.50	2.25	13.9	1.11	

In the same way as in the case of HP-Al:LLZO-LG, the samples with smaller grain size HP-Al:LLZO-SG showed an tendency of K_{IC} decrease with increasing pillar diameter, for the 10 and 5 µm pillars 1.06 ± 0.15 MPa·m$^{0.5}$ and 0.96 ± 0.12 MPa·m$^{0.5}$, respectively, were obtained, however, again the values differ only within the limits of uncertainty. Nevertheless the decrease might indicate that the gallium damage can influence the fracture toughness, particularly for pillars with smaller diameters. In order to investigate the influence of Ga-ion damage on the pillar, an EDX was performed on one of the pillars with 5 µm diameter; the results are shown in Figure 4.43 and discussed next.

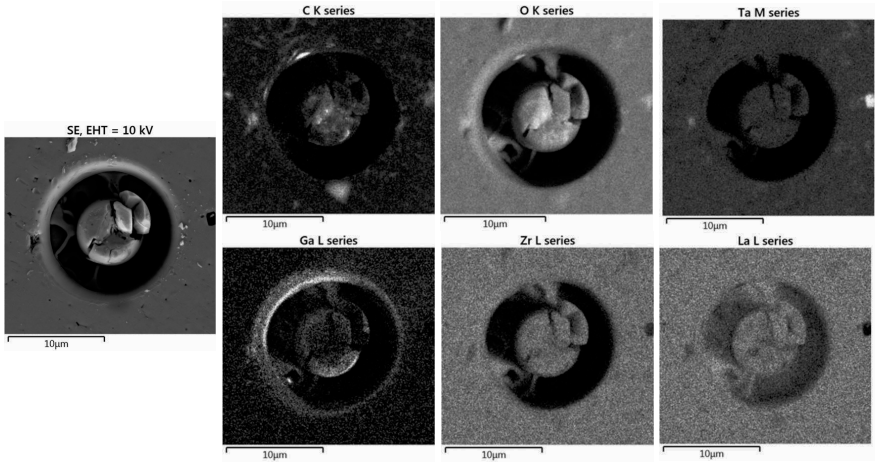

Figure 4.43- EDX of pillar 9 (5 µm diameter) after testing sample HP-Al:LLZO-SG.

It is possible to see that, similar as in the pillar analysis in section 4.2.2, the Ga is concentrated on the edges of the pillar (brighter area), which might influence pillars with smaller diameter to some extent, since the distance between the center, where the indentation is imprinted, and the edges are shorter. According to Lauener et al., the influence of FIB damage diminishes to negligibility for pillar diameters of around 10 µm and larger [132], where the small difference obtained for the results of the 5 and 10 µm pillars indicates that the values obtained for the 10 µm pillars are already representative for the materials property. Nevertheless, to verify this fact more studies in forthcoming works with different pillar diameters would be an asset.
Furthermore, it is important to mention that due to the transfer of the sample in ambient atmosphere from the nano-indenter device to SEM, the materials reacts with air/moisture and a degradation layer is formed at the surface, as possible to see in the carbon detection in Figure 4.43, which however, did not affect the pillar testing.

Comparing the fracture toughness of single crystal and polycrystalline material, the values are in the same range; however, for the polycrystalline case the scatter in the critical loads is larger. For pillars of 10 µm diameter the critical load ranges from 32.2 to 43.5 mN and for 5 µm diameter it varies from 10.6 to 15.4 mN. These variations affect directly the K_{IC} final average, leading to a scatter of more than 10%. In this respect, it appears that the micro-pillar test can be highly affected by the local microstructure. The local area where the tip has the first contact to surface might be affected by local inhomogeneities or flaws, i.e. grain boundary (considering grain size of ~2 µm) can influence directly the critical failure load. Such an effect can be illustrated in Figure 4.42 b) and d), where in the pillar top view crack propagation and in some cases destruction of the pillar (i.e. pillar 5 to 10) can be observed and confirmed by Figure 4.44, which shows the typical crack trajectories on HP-Al:LLZO-SG after testing for pillars with approximately 10 and 5 µm diameter, respectively. It is possible to see that the cracks have a tortuous path and grow mostly along grain boundaries.

Overall, the fracture toughness values obtained via micro-pillar testing for larger pillars are slightly lower when compared to that of smaller pillars, however due to the range of uncertainties no final conclusion can be derived. In the same way, comparing the average of VIF values to micro-pillar splitting of large grains sample, are in agreement.

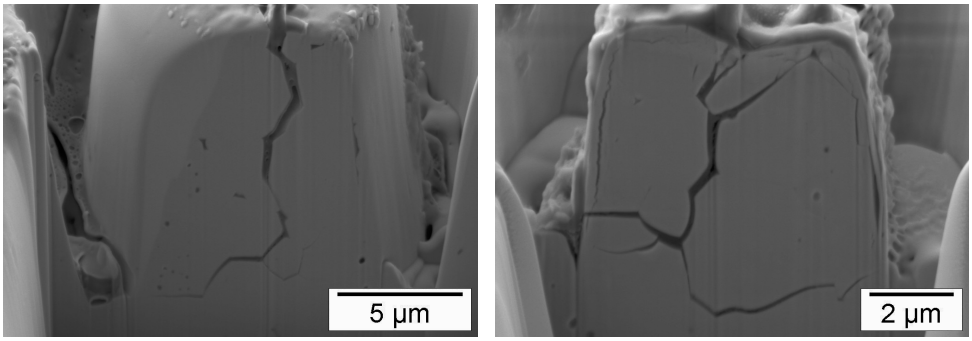

a) b)

Figure 4.44 –SEM micrographs of cross-sectional FIB cut on HP-Al:LLZO-SG of a) pillar 5 (~10 µm diameter) b) pillar 9 (~5 µm diameter).

Focusing on small grains size sample, the average fracture toughness of polycrystalline LLZO obtained via the micro-pillar is ~1.02 MPa·m$^{0.5}$ and VIF average is 0.98 MPa·m$^{0.5}$, which are in very good agreement. Besides, fracture toughness values obtained at this work are in the same range as those in literature, which reports values of 0.86-1.63 MPa·m$^{0.5}$ for cubic dense LLZO with mean grain size of ~ 5 µm [14]. For similar material, Al-substituted cubic garnet $Li_{6.19}Al_{0.27}La_3Zr_2O_{12}$ (LLZO) produced by cold pressing with 98% density and grain size of ~3 µm the fracture toughness reported in the previous section by indentation is 0.97 ± 0.1 MPa·m$^{0.5}$, which is also in good agreement with values reported here.

Furthermore, the value is also in agreement with the single crystal representative fracture toughness of Al-doped LLZO obtained in the section 4.2 via micro-pillar splitting test, 0.99 ± 0.05 MPa·m$^{0.5}$, with grain size of 100 µm. In addition, it has been reported that the K_{IC} is independent of grain size for cubic oxides at room temperature over the grain size range from 10 to 150 µm [183, 184]. Considering the fracture toughness values obtained in the previous section for the similar material (see section 4.1.4) produced via cold-pressing, with grain size ~10 µm and porosities from 8.7 to 13.8%, the VIF toughness ranged from 1.35 to 1.13 MPa·m$^{0.5}$, which is also in good agreement with micro-pillar values in this work. Therefore, within the grain size range investigated in the present work, the fracture toughness obtained via micro-pillar splitting test is constant.

5. Conclusions and Outlook

In order to supply the increasing demand of energy in stationary and especially also mobile applications and satisfy requirements related to the stabilization of national and global energy networks largely based on renewable resources, it is necessary to develop batteries with higher capacities that have to be mechanically reliable. The importance of the mechanical properties has received increasing interest and led to discussion on the fast intercalation of ions into the electrodes creating internal stresses, which can eventually lead to formation of micro-cracks and fracture, Li-dendrites and disintegration that reduces the cycle life of the battery. Toward this goal, the present study has investigated the important mechanical parameters elastic modulus, hardness and fracture toughness along with an in-depth study of microstructural features related to these mechanical aspects.

Hence, in the present work, depth-sensitive indentation has been extensively used to characterize garnet $Li_7La_3Zr_2O_{12}$ solid electrolyte. Elastic modulus and hardness were obtained for non-, Al- and Ta- substituted LLZO and the fracture toughness was estimated from the size of cracks induced by indentation test and correlated with microstructure features. In addition, the novel micro-pillar splitting test was employed to determine the fracture toughness and compared to conventional indentation testing results.

In the first part of the current work, preparation conditions were correlated to microstructure, electrochemical and mechanical properties. Intrinsic material properties were determined at shallow depths and effective properties related more to macroscopic scales at higher depths. Microstructural features such as porosity, dopant amount and phase ratio (tetragonal/cubic) influence the experimental modulus. With respect to the mechanical properties, the elastic modulus of Al-doped materials increased at low dopant levels and decreased at higher substitutional levels, ranging from 163 ± 4 GPa to 142 ± 1 GPa, compared to the un-substituted LLZ, possessing a value of 156 ± 9 GPa. For Ta:LLZ the values are always lower than for un-substituted LLZ, however, slowly approaching this value at higher dopant levels. Global, effective specimens' mechanical properties obtained at higher indentation depths/loads are affected by both the properties of the material itself (including grain size effects) and the porosity, varying from 124 ± 3 GPa to 149 ± 7 GPa. For Ta:LLZ the rather low values even for high density samples need to be kept in mind

when considering component design and manufacturing, since often elastic moduli behaviors are also reflected in materials fracture strengths.

In the second part, the micro-pillar splitting method was successful introduced and used for the first time on the solid electrolyte material Al-substituted $Li_7La_3Zr_2O_{12}$ produced via cold-pressing. The single crystal representative fracture toughness value obtained via micro-pillar splitting tests was 0.99 ± 0.05 MPa $m^{0.5}$, which is in good agreement with the global VIF fracture toughness 1.19 MPa $m^{0.5}$ obtained in the current work, using a Palmqvist crack model. A direct comparison with literature has to be carried out carefully, since grain sizes and composition have to be taken into consideration.

In the third and last part, the mechanical properties were measured as function of grain size for dense hot-pressed Al-doped and Al-free $Li_{6.6}La_3Zr_{1.6}Ta_{0.4}O_{12}$ with precursor powder processed via synthesized via solid-state synthesis and solution-assisted solid-state synthesis. Elastic modulus and hardness as function of penetration depth were evaluated, and are constant in the depth range evaluated. Fracture toughness was measured via VIF and micro-pillar splitting test, in addition pillar size effect was investigated at pillar diameter of 5 and 10 µm. For VIF toughness, the results indicate that loads exceeding 3 N are not appropriate due to secondary cracks. A straight crack shape was observed for samples with larger grain size and a path along grain boundaries for samples with smaller grains (see Figure 4.37). Besides the crack pattern, grain size has no influence on the fracture toughness. Single crystal and polycrystalline toughness of hot pressed materials are ~1 MPa $m^{0.5}$. For micro-pillars with 5 µm diameter an apparent increase in the fracture toughness is noted and this was attributed to Ga-ion damage, however, for pillars with 10 µm diameter this effect is considered to be negligible since the damage is concentrated at the edges of the pillar and far from the location of crack initiation. Further investigation with different pillar diameter and in similar direction can be made for materials after operation.

Conclusively, the LLZO materials would attend the criteria proposed by Monroe et al. [96] to avoid dendrite formation, however, additional necessary selection criteria based not only on the elastic behavior cannot be ruled out for this material. In addition the fracture toughness values of LLZO is in general around 1.1 MPa $m^{0.5}$ and suggests that improvements are advantageous without causing detrimental effect on ionic conductivity. The provided mechanical properties of this work could form the fundamental basis for rather advanced databases and simulation work, in order to

design novel and optimized materials and architectures. The successfully establishment of fracture toughness via micro-pillar splitting test can be a basis for future works on solid electrolytes, assessing local fracture toughness values on samples with compositional variations, different grain orientations, samples after long-term operation and also tests at adverse temperatures.

6. References

[1] B. Lin, W. Wu, Economic viability of battery energy storage and grid strategy: A special case of China electricity market, Energy 124 (2017) 423-434.

[2] K. Bradbury, L. Pratson, D. Patiño-Echeverri, Economic viability of energy storage systems based on price arbitrage potential in real-time U.S. electricity markets, Applied Energy 114 (2014) 512-519.

[3] S.J. Kazempour, M.P. Moghaddam, Economic viability of NaS battery plant in a competitive electricity market, 2009 International Conference on Clean Electrical Power, 2009, pp. 453-459.

[4] M. Skyllas-Kazacos, M.H. Chakrabarti, S.A. Hajimolana, F.S. Mjalli, M. Saleem, Progress in Flow Battery Research and Development, J. Electrochem. Soc. 158(8) (2011) R55-R79.

[5] H. Li, Z. Wang, L. Chen, X. Huang, Research on advanced materials for Li-ion batteries, Adv. Mater. 21(45) (2009) 4593-4607.

[6] B. Dunn, H. Kamath, J.-M. Tarascon, Electrical Energy Storage for the Grid: A Battery of Choices, Science 334(6058) (2011) 928-935.

[7] D.L. Wood, J. Li, C. Daniel, Prospects for reducing the processing cost of lithium ion batteries, J. Power Sources 275 (2015) 234-242.

[8] J.G. Kim, B. Son, S. Mukherjee, N. Schuppert, A. Bates, O. Kwon, M.J. Choi, H.Y. Chung, S. Park, A review of lithium and non-lithium based solid state batteries, J. Power Sources 282 (2015) 299-322.

[9] B. Scrosati, J. Garche, Lithium batteries: Status, prospects and future, J. Power Sources 195(9) (2010) 2419-2430.

[10] P. Knauth, Inorganic solid Li ion conductors: An overview, Solid State Ionics 180(14) (2009) 911-916.

[11] S. Teng, J. Tan, A. Tiwari, Recent developments in garnet based solid state electrolytes for thin film batteries, Curr. Opin. Solid State Mater. Sci. 18(1) (2014) 29-38.

[12] M. Guin, F. Tietz, Survey of the transport properties of sodium superionic conductor materials for use in sodium batteries, J. of Power Sources 273 (2015) 1056-1064.

[13] S. Yu, R.D. Schmidt, R. Garcia-Mendez, E. Herbert, N.J. Dudney, J.B. Wolfenstine, J. Sakamoto, D.J. Siegel, Elastic Properties of the Solid Electrolyte $Li_7La_3Zr_2O_{12}$ (LLZO), Chem. Mater. 28(1) (2016) 197-206.

[14] J. Wolfenstine, H. Jo, Y.-H. Cho, I.N. David, P. Askeland, E.D. Case, H. Kim, H. Choe, J. Sakamoto, A preliminary investigation of fracture toughness of $Li_7La_3Zr_2O_{12}$ and its comparison to other solid Li-ionconductors, Mater. Lett. 96 (2013) 117-120.

[15] J.E. Ni, E.D. Case, J.S. Sakamoto, E. Rangasamy, J.B. Wolfenstine, Room temperature elastic moduli and Vickers hardness of hot-pressed LLZO cubic garnet, J Mater SCI, 47(23) (2012) 7978-7985.

[16] M. Winter, R.J. Brodd, What Are Batteries, Fuel Cells, and Supercapacitors?, Chem. Rev. 104(10) (2004) 4245-4270.

[17] M.M. Thackeray, C. Wolverton, E.D. Isaacs, Electrical energy storage for transportation-approaching the limits of, and going beyond, lithium-ion batteries, Energy & Environmental Science 5(7) (2012) 7854-7863.

[18] V. Etacheri, R. Marom, R. Elazari, G. Salitra, D. Aurbach, Challenges in the development of advanced Li-ion batteries: a review, Energy & Environmental Science 4(9) (2011) 3243-3262.

[19] J.M. Tarascon, M. Armand, Issues and challenges facing rechargeable lithium batteries, Nature 414 (2001) 359.

[20] M.S. Whittingham, Lithium Batteries and Cathode Materials, Chem. Rev. 104(10) (2004) 4271-4302.

[21] N. Nitta, F. Wu, J.T. Lee, G. Yushin, Li-ion battery materials: present and future, Mater. Today 18(5) (2015) 252-264.

[22] H.J. Bergveld, W.S. Kruijt, P.H. Notten, Battery management systems, Springer2002, pp. 9-30.

[23] S. Dhameja, Electric vehicle battery systems, Elsevier 2001.

[24] G. Bucci, T. Swamy, S. Bishop, B.W. Sheldon, Y.-M. Chiang, W.C. Carter, The Effect of Stress on Battery-Electrode Capacity, J. Electrochem. Soc. 164(4) (2017) A645-A654.

[25] J. Banerjee, K. Dutta, Materials for Electrodes of Li-Ion Batteries: Issues Related to Stress Development, Crit. Rev. Solid State Mater. Sci. 42(3) (2017) 218-238.

[26] A. Mukhopadhyay, B.W. Sheldon, Deformation and stress in electrode materials for Li-ion batteries, Prog. Mater Sci. 63 (2014) 58-116.

[27] H. Tavassol, E.M. Jones, N.R. Sottos, A.A. Gewirth, Electrochemical stiffness in lithium-ion batteries, Nat. Mater. 15(11) (2016) 1182-1187.

[28] L. de Biasi, G. Lieser, J. Rana, S. Indris, C. Drager, S. Glatthaar, R. Monig, H. Ehrenberg, G. Schumacher, J.R. Binder, Ge, Unravelling the mechanism of lithium insertion into and extraction from trirutile-type $LiNiFeF_6$ cathode material for Li-ion batteries, Cryst Eng Comm 17(32) (2015) 6163-6174.

[29] Y. Qi, H. Guo, L.G. Hector, A. Timmons, Threefold Increase in the Young's Modulus of Graphite Negative Electrode during Lithium Intercalation, J. Electrochem. Soc. 157(5) (2010) A558-A566.

[30] A. Timmons, J.R. Dahn, Isotropic Volume Expansion of Particles of Amorphous Metallic Alloys in Composite Negative Electrodes for Li-Ion Batteries, J. Electrochem. Soc. 154(5) (2007) A444-A448.

[31] L.Y. Beaulieu, K.W. Eberman, R.L. Turner, L.J. Krause, J.R. Dahn, Colossal Reversible Volume Changes in Lithium Alloys, Electrochem. Solid-State Lett. 4(9) (2001) A137-A140.

[32] E. Markervich, G. Salitra, M.D. Levi, D. Aurbach, Capacity fading of lithiated graphite electrodes studied by a combination of electroanalytical methods, Raman spectroscopy and SEM, J. Power Sources 146(1) (2005) 146-150.

[33] D. Aurbach, E. Zinigrad, Y. Cohen, H. Teller, A short review of failure mechanisms of lithium metal and lithiated graphite anodes in liquid electrolyte solutions, Solid State Ionics 148(3) (2002) 405-416.

[34] M.S. Whittingham, Electrical energy storage and intercalation chemistry, Science 192(4244) (1976) 1126-1127.

[35] X. Feng, M. Ouyang, X. Liu, L. Lu, Y. Xia, X. He, Thermal runaway mechanism of lithium ion battery for electric vehicles: A review, Energy Storage Materials 10 (2018) 246-267.

[36] H.U. Escobar-Hernandez, R.M. Gustafson, M.I. Papadaki, S. Sachdeva, M.S. Mannan, Thermal Runaway in Lithium-Ion Batteries: Incidents, Kinetics of the Runaway and Assessment of Factors Affecting Its Initiation, J. Electrochem. Soc. 163(13) (2016) A2691-A2701.

[37] R.C. Agrawal, G.P. Pandey, Solid polymer electrolytes: materials designing and all-solid-state battery applications: an overview, J. Phys. D: Appl. Phys. 41(22) (2008) 223001.

[38] J. Chen, Recent Progress in Advanced Materials for Lithium Ion Batteries, Materials 6(1) (2013).

[39] J.F. Oudenhoven, L. Baggetto, P.H. Notten, All-Solid-State Lithium-Ion Microbatteries: A Review of Various Three-Dimensional Concepts, Advanced Energy Materials 1(1) (2011) 10-33.

[40] K. Kerman, A. Luntz, V. Viswanathan, Y.-M. Chiang, Z. Chen, Review—Practical Challenges Hindering the Development of Solid State Li Ion Batteries, J. Electrochem. Soc. 164(7) (2017) A1731-A1744.

[41] G.G. Amatucci, J.M. Tarascon, L.C. Klein, Cobalt dissolution in $LiCoO_2$-based non-aqueous rechargeable batteries, Solid State Ionics 83(1) (1996) 167-173.

[42] E. Rossen, J. Reimers, J.R. Dahn, Synthesis and Electrochemistry of Spinel LT-$LiCoO_2$, Solid State Ionics 1993.

[43] D.W. Murphy, P.A. Christian, F.J. DiSalvo, J.N. Carides, Vanadium Oxide Cathode Materials for Secondary Lithium Cells, J. Electrochem. Soc. 126(3) (1979) 497-499.

[44] Y.P. Wu, E. Rahm, R. Holze, Carbon anode materials for lithium ion batteries, J. Power Sources 114(2) (2003) 228-236.

[45] J.-K. Ahn, S.-G. Yoon, Characteristics of Amorphous Lithium Lanthanum Titanate Electrolyte Thin Films Grown by PLD for Use in Rechargeable Lithium Microbatteries, Electrochem. Solid-State Lett. 8(2) (2005) A75-A78.

[46] X. Sun, P.V. Radovanovic, B. Cui, Advances in spinel $Li_4Ti_5O_{12}$ anode materials for lithium-ion batteries, New J. Chem. 39(1) (2015) 38-63.

[47] C. Chen, R. Agrawal, C. Wang, High Performance $Li_4Ti_5O_{12}$/Si Composite Anodes for Li-Ion Batteries, Nanomaterials 5(3) (2015) 1469-1480.

[48] K. Mukai, Y. Kato, H. Nakano, Understanding the Zero-Strain Lithium Insertion Scheme of $Li[Li_{1/3}Ti_{5/3}]O_4$: Structural Changes at Atomic Scale Clarified by Raman Spectroscopy, The J Phys Chem C 118(6) (2014) 2992-2999.

[49] R. Dash, S. Pannala, Theoretical Limits of Energy Density in Silicon-Carbon Composite Anode Based Lithium Ion Batteries, Sci. Rep. 6 (2016) 27449.

[50] M. Ko, S. Chae, J. Cho, Challenges in Accommodating Volume Change of Si Anodes for Li-Ion Batteries, Chem Electro Chem 2(11) (2015) 1645-1651.

[51] E. Quartarone, P. Mustarelli, Electrolytes for solid-state lithium rechargeable batteries: recent advances and perspectives, Chem. Soc. Rev. 40(5) (2011) 2525-2540.

[52] J.W. Fergus, Ceramic and polymeric solid electrolytes for lithium-ion batteries, J. Power Sources 195(15) (2010) 4554-4569.

[53] J. Janek, W.G. Zeier, A solid future for battery development, Nature Energy 1 (2016) 16141.

[54] A. Unemoto, H. Ogawa, Y. Gambe, I. Honma, Development of lithium-sulfur batteries using room temperature ionic liquid-based quasi-solid-state electrolytes, Electrochim. Acta 125 (2014) 386-394.

[55] F. Aguesse, W. Manalastas, L. Buannic, J.M. Lopez del Amo, G. Singh, A. Llordés, J. Kilner, Investigating the Dendritic Growth during Full Cell Cycling of Garnet Electrolyte in Direct Contact with Li Metal, ACS Applied Materials & Interfaces 9(4) (2017) 3808-3816.

[56] Y. Xiayin, H. Bingxin, Y. Jingyun, P. Gang, H. Zhen, G. Chao, L. Deng, X. Xiaoxiong, All-solid-state lithium batteries with inorganic solid electrolytes: Review of fundamental science, Chinese Physics B 25(1) (2016) 018802.

[57] V. Thangadurai, W. Weppner, Recent progress in solid oxide and lithium ion conducting electrolytes research, Ionics 12(1) (2006) 81-92.

[58] A. Manthiram, X. Yu, S. Wang, Lithium battery chemistries enabled by solid-state electrolytes, Nature Reviews Materials 2(4) (2017) 16103.

[59] S.B. Aziz, T.J. Woo, M.F.Z. Kadir, H.M. Ahmed, A conceptual review on polymer electrolytes and ion transport models, Journal of Science: Advanced Materials and Devices 3(1) (2018) 1-17.

[60] V. Di Noto, S. Lavina, G.A. Giffin, E. Negro, B. Scrosati, Polymer electrolytes: Present, past and future, Electrochim. Acta 57 (2011) 4-13.

[61] S.S. Zhang, M.H. Ervin, K. Xu, T.R. Jow, Microporous poly(acrylonitrile-methyl methacrylate) membrane as a separator of rechargeable lithium battery, Electrochim. Acta 49(20) (2004) 3339-3345.

[62] M. Alamgir, K. Abraham, Li ion conductive electrolytes based on poly (vinyl chloride), J. Electrochem. Soc. 140(6) (1993) L96-L97.

[63] G. Feuillade, P. Perche, Ion-conductive macromolecular gels and membranes for solid lithium cells, J. Appl. Electrochem. 5(1) (1975) 63-69.

[64] B.K. Money, J. Swenson, Dynamics of Poly(ethylene oxide) around Its Melting Temperature, Macromolecules 46(17) (2013) 6949-6954.

[65] M. Armand, Polymer solid electrolytes - an overview, Solid State Ionics 9-10 (1983) 745-754.

[66] H.M.J.C. Pitawala, M.A.K.L. Dissanayake, V.A. Seneviratne, B.-E. Mellander, I. Albinson, Effect of plasticizers (EC or PC) on the ionic conductivity and thermal properties of the $(PEO)_9LiTf$: Al_2O_3 nanocomposite polymer electrolyte system, J. Solid State Electrochem. 12(7) (2008) 783-789.

[67] C. Shen, J. Wang, Z. Tang, H. Wang, H. Lian, J. Zhang, C.-n. Cao, Physicochemical properties of poly(ethylene oxide)-based composite polymer electrolytes with a silane-modified mesoporous silica SBA-15, Electrochim. Acta 54(12) (2009) 3490-3494.

[68] G. Appetecchi, F. Croce, L. Persi, F. Ronci, B. Scrosati, Transport and interfacial properties of composite polymer electrolytes, Electrochim. Acta 45(8-9) (2000) 1481-1490.

[69] B.T. Ahn, R.A. Huggins, Phase behavior and conductivity of Li_2SiS_3 composition, Solid State Ionics 46(3-4) (1991) 237-242.

[70] S. Kondo, K. Takada, Y. Yamamura, New lithium ion conductors based on Li_2S-SiS_2 system, Solid State Ionics 53 (1992) 1183-1186.

[71] R. Kanno, M. Murayama, Lithium Ionic Conductor Thio-LISICON: The $Li_2SGeS_2P_2S_5$ System, J. Electrochem. Soc. 148(7) (2001) A742-A746.

[72] N. Kamaya, K. Homma, Y. Yamakawa, M. Hirayama, R. Kanno, M. Yonemura, T. Kamiyama, Y. Kato, S. Hama, K. Kawamoto, A. Mitsui, A lithium superionic conductor, Nature Materials 10 (2011) 682.

[73] H. Muramatsu, A. Hayashi, T. Ohtomo, S. Hama, M. Tatsumisago, Structural change of Li_2S–P_2S_5 sulfide solid electrolytes in the atmosphere, Solid State Ionics 182(1) (2011) 116-119.

[74] A. Hayashi, H. Muramatsu, T. Ohtomo, S. Hama, M. Tatsumisago, Improved chemical stability and cyclability in Li_2S–P_2S_5–P_2O_5–ZnO composite electrolytes for all-solid-state rechargeable lithium batteries, J. Alloys Compd. 591 (2014) 247-250.

[75] Y. Inaguma, C. Liquan, M. Itoh, T. Nakamura, T. Uchida, H. Ikuta, M. Wakihara, High ionic conductivity in lithium lanthanum titanate, Solid State Commun. 86(10) (1993) 689-693.

[76] X. Xu, Z. Wen, X. Yang, L. Chen, Dense nanostructured solid electrolyte with high Li-ion conductivity by spark plasma sintering technique, Mater. Res. Bull. 43(8) (2008) 2334-2341.

[77] H. Aono, E. Sugimoto, Y. Sadaoka, N. Imanaka, G.-y. Adachi, Ionic conductivity and sinterability of lithium titanium phosphate system, Solid State Ionics 40-41 (1990) 38-42.

[78] J.S. Thokchom, N. Gupta, B. Kumar, Superionic Conductivity in a Lithium Aluminum Germanium Phosphate Glass–Ceramic, J. Electrochem. Soc. 155(12) (2008) A915-A920.

[79] Q. Guo, Y. Han, H. Wang, S. Xiong, Y. Li, S. Liu, K. Xie, New Class of LAGP-Based Solid Polymer Composite Electrolyte for Efficient and Safe Solid-State Lithium Batteries, ACS Applied Materials & Interfaces 9(48) (2017) 41837-41844.

[80] V. Thangadurai, S. Narayanan, D. Pinzaru, Garnet-type solid-state fast Li ion conductors for Li batteries: critical review, Chem. Soc. Rev. 43(13) (2014) 4714-27.

[81] M. Kotobuki, H. Munakata, K. Kanamura, Y. Sato, T. Yoshida, Compatibility of $Li_7La_3Zr_2O_{12}$ Solid Electrolyte to All-Solid-State Battery Using Li Metal Anode, J. Electrochem. Soc. 157(10) (2010) A1076-A1079.

[82] A. Kuhn, S. Narayanan, L. Spencer, G. Goward, V. Thangadurai, M. Wilkening, Li self-diffusion in garnet-type $Li_7La_3Zr_2O_{12}$ as probed directly by diffusion-induced ^7Li spin-lattice relaxation NMR spectroscopy, Physical Review B 83(9) (2011) 094302.

[83] R. Murugan, V. Thangadurai, W. Weppner, Fast lithium ion conduction in garnet-type $Li_7La_3Zr_2O_{12}$, Angew. Chem. Int. Ed. 46(41) (2007) 7778-7781.

[84] J. Awaka, N. Kijima, H. Hayakawa, J. Akimoto, Synthesis and structure analysis of tetragonal $Li_7La_3Zr_2O_{12}$ with the garnet-related type structure, J. Solid State Chem. 182(8) (2009) 2046-2052.

[85] A. Logéat, T. Köhler, U. Eisele, B. Stiaszny, A. Harzer, M. Tovar, A. Senyshyn, H. Ehrenberg, B. Kozinsky, From order to disorder: The structure of lithium-conducting garnets $Li_{7-x}La_3Ta_xZr_{2-x}O_{12}$ (x=0–2), Solid State Ionics 206 (2012) 33-38.

[86] E. Rangasamy, J. Wolfenstine, J. Sakamoto, The role of Al and Li concentration on the formation of cubic garnet solid electrolyte of nominal composition $Li_7La_3Zr_2O_{12}$, Solid State Ionics 206 (2012) 28-32.

[87] J.-F. Wu, E.-Y. Chen, Y. Yu, L. Liu, Y. Wu, W.K. Pang, V.K. Peterson, X. Guo, Gallium-doped $Li_7La_3Zr_2O_{12}$ garnet-type electrolytes with high lithium-ion conductivity, ACS applied materials & interfaces 9(2) (2017) 1542-1552.

[88] M. Bitzer, T. Van Gestel, S. Uhlenbruck, H. Buchkremer, Sol-gel synthesis of thin solid $Li_7La_3Zr_2O_{12}$ electrolyte films for Li-ion batteries, 2016.

[89] H. El Shinawi, J. Janek, Stabilization of cubic lithium-stuffed garnets of the type "$Li_7La_3Zr_3O_{12}$" by addition of gallium, J. Power Sources 225 (2013) 13-19.

[90] G. Larraz, A. Orera, M. Sanjuan, Cubic phases of garnet-type $Li_7La_3Zr_2O_{12}$: the role of hydration, J Mater Chem A 1(37) (2013) 11419-11428.

[91] M. Matsui, K. Takahashi, K. Sakamoto, A. Hirano, Y. Takeda, O. Yamamoto, N. Imanishi, Phase stability of a garnet-type lithium ion conductor $Li_7La_3Zr_2O_{12}$, Dalton Transactions 43(3) (2014) 1019-1024.

[92] L. Truong, V. Thangadurai, Soft-Chemistry of Garnet-Type $Li_{5+x}Ba_xLa_{3-x}Nb_2O_{12}$ (x = 0, 0.5, 1): Reversible $H^+ \leftrightarrow Li^+$ Ion-Exchange Reaction and Their X-ray, ^{7}Li MAS NMR, IR, and AC Impedance Spectroscopy Characterization, Chem. Mater. 23(17) (2011) 3970-3977.

[93] C. Galven, J.-L. Fourquet, M.-P. Crosnier-Lopez, F. Le Berre, Instability of the Lithium Garnet $Li_7La_3Sn_2O_{12}$: Li^+/H^+ Exchange and Structural Study, Chem. Mater. 23(7) (2011) 1892-1900.

[94] Y. Jin, P.J. McGinn, $Li_7La_3Zr_2O_{12}$ electrolyte stability in air and fabrication of a $Li/Li_7La_3Zr_2O_{12}/Cu_{0.1}V_2O_5$ solid-state battery, J. Power Sources 239 (2013) 326-331.

[95] J. Wolfenstine, J.L. Allen, J. Sakamoto, D.J. Siegel, H. Choe, Mechanical behavior of Li-ion-conducting crystalline oxide-based solid electrolytes: a brief review, Ionics 24(5) (2018) 1271-1276.

[96] C. Monroe, J. Newman, The Impact of Elastic Deformation on Deposition Kinetics at Lithium/Polymer Interfaces, J. Electrochem. Soc. 152(2) (2005) A396.

[97] Y. Chiang, D. Birnie III, W. Kingery, Physical Ceramics: Principles for Ceramic Science and Engineering New York, John Wiley & Sons (1997) 351-513.

[98] M. Barsoum, M. Barsoum, Fundamentals of ceramics, CRC press 2002.

[99] W. CALLISTER Jr, Fundamentals of Materials Science and Engineering: An Integrated Approach. New York: John Wiley&Sons, Inc, 2005.

[100] G. Bucci, T. Swamy, Y.-M. Chiang, W.C. Carter, Modeling of internal mechanical failure of all-solid-state batteries during electrochemical cycling, and implications for battery design, J. Mater. Chem. A (2017).

[101] S.D. Jackman, R.A. Cutler, Effect of microcracking on ionic conductivity in LATP, J. Power Sources 218 (2012) 65-72.

[102] E.G. Herbert, W.E. Tenhaeff, N.J. Dudney, G.M. Pharr, Mechanical characterization of LiPON films using nanoindentation, Thin Solid Films 520(1) (2011) 413-418.

[103] Y.-H. Cho, J. Wolfenstine, E. Rangasamy, H. Kim, H. Choe, J. Sakamoto, Mechanical properties of the solid Li-ion conducting electrolyte: $Li_{0.33}La_{0.57}TiO_3$, Journal of Materials Science 47(16) (2012) 5970-5977.

[104] A. Sakuda, A. Hayashi, Y. Takigawa, K. Higashi, M. Tatsumisago, Evaluation of elastic modulus of Li_2S-P_2S_5 glassy solid electrolyte by ultrasonic sound velocity measurement and compression test, J. Ceram. Soc. Jpn. 121(1419) (2013) 946-949.

[105] W.C. Oliver, G.M. Pharr, An improved technique for determining hardness and elastic modulus using load and displacement sensing indentation experiments, J. Mater. Res. 7(6) (1992) 1564-1583.

[106] J. Wei, G. Pećanac, J. Malzbender, Review of mechanical characterization methods for ceramics used in energy technologies, Ceram. Int. 40(10) (2014) 15371-15380.

[107] C.B. Carter, M.G. Norton, Ceramic materials: science and engineering, Springer Science & Business Media 2007.

[108] Z. Peng, J. Gong, H. Miao, On the description of indentation size effect in hardness testing for ceramics: Analysis of the nanoindentation data, J. Eur. Ceram. Soc. 24(8) (2004) 2193-2201.

[109] D. Munz, T. Fett, Ceramics: mechanical properties, failure behaviour, materials selection, Springer Science & Business Media2013.

[110] M. Sebastiani, K.E. Johanns, E.G. Herbert, F. Carassiti, G.M. Pharr, A novel pillar indentation splitting test for measuring fracture toughness of thin ceramic coatings, Philos. Mag. 95(16-18) (2014) 1928-1944.

[111] S. Palmqvist, Occurrence of crack formation during Vickers indentation as a measure of the toughness of hard materials, Arch Eisenhuettenwes 33 (1962) 629-333.

[112] A.G. Evans, E.A. Charles, Fracture Toughness Determinations by Indentation, J. Am. Ceram. Soc. 59(7-8) (1976) 371-372.

[113] G.D. Quinn, R.C. Bradt, On the Vickers Indentation Fracture Toughness Test, J. Am. Ceram. Soc. 90(3) (2007) 673-680.

[114] K. Niihara, A fracture mechanics analysis of indentation-induced Palmqvist crack in ceramics, J. Mater. Sci. Lett. 2(5) (1983) 221-223.

[115] G.R. Anstis, P. Chantikul, B.R. Lawn, D.B. Marshall, A Critical Evaluation of Indentation Techniques for Measuring Fracture Toughness: I, Direct Crack Measurements, J. Am. Ceram. Soc. 64(9) (1981) 533-538.

[116] P. Chantikul, G.R. Anstis, B.R. Lawn, D.B. Marshall, A Critical Evaluation of Indentation Techniques for Measuring Fracture Toughness: II, Strength Method, J Am Ceram Soc 64(9) (1981) 539-543.

[117] K. Niihara, R. Morena, D. Hasselman, Evaluation ofK Ic of brittle solids by the indentation method with low crack-to-indent ratios, J. Mater. Sci. Lett. 1(1) (1982) 13-16.

[118] F. Sergejev, M. Antonov, Comparative study on indentation fracture toughness measurements of cemented carbides, Proc. Estonian Acad. Sci. Eng 12(4) (2006) 388-398.

[119] B.R. Lawn, E.R. Fuller, Equilibrium penny-like cracks in indentation fracture, J Mater Sci 10(12) (1975) 2016-2024.

[120] A.G. Evans, T.R. Wilshaw, Quasi-static solid particle damage in brittle solids—I. Observations analysis and implications, Acta Metall. 24(10) (1976) 939-956.

[121] A.G. EVans, E.A. Charles, Fracture toughness determinations by indentation, J Am Ceram Soc 59(7-8) (1976) 371-372.

[122] K. Niihara, R. Morena, D.P.H. Hasselman, Evaluation of K_{IC} of brittle solids by the indentation method with low crack-to-indent ratios, J Mater Sci Lett 1(1) (1982) 13-16.

[123] B.R. Lawn, A. Evans, D. Marshall, Elastic/plastic indentation damage in ceramics: the median/radial crack system, J Am Ceram Soc 63(9-10) (1980) 574-581.

[124] K. Tanaka, Elastic/plastic indentation hardness and indentation fracture toughness: The inclusion core model, J Mater Sci 22(4) (1987) 1501-1508.

[125] M. Sebastiani, K.E. Johanns, E.G. Herbert, G.M. Pharr, Measurement of fracture toughness by nanoindentation methods: Recent advances and future challenges, Curr. Opin. Solid State Mater. Sci. 19(6) (2015) 324-333.

[126] M.Z. Mughal, R. Moscatelli, H.-Y. Amanieu, M. Sebastiani, Effect of lithiation on micro-scale fracture toughness of $Li_xMn_2O_4$ cathode, Scripta Mater. 116 (2016) 62-66.

[127] M. Sebastiani, M. Renzelli, Focused Ion Beam and Nanomechanical Tests for High Resolution Characterisation: New Resources for Platinum Group Metals Testing, Platinum Met. Rev. 58(1) (2014) 3-19.

[128] B.J. Eggleton, S. Palomba, A.J.G. Lunt, G. Mohanty, T.K. Neo, J. Michler, A.M. Korsunsky, Microscale resolution fracture toughness profiling at the zirconia-porcelain interface in dental prostheses, Proceedings of the SPIE 9668 (2015) 96685S.

[129] A. Davydok, B.N. Jaya, O. Robach, O. Ulrich, J.-S. Micha, C. Kirchlechner, Analysis of the full stress tensor in a micropillar: Ability of and difficulties arising during synchrotron based μLaue diffraction, Materials & Design 108 (2016) 68-75.

[130] Q. Liu, A. Roy, V.V. Silberschmidt, Size-dependent crystal plasticity: From micro-pillar compression to bending, Mech. Mater. 100 (2016) 31-40.

[131] A.-N. Wang, J.F. Nonemacher, G. Yan, M. Finsterbusch, J. Malzbender, M. Krüger, Mechanical properties of the solid electrolyte Al-substituted $Li_7La_3Zr_2O_{12}$ (LLZO) by utilizing micro-pillar indentation splitting test, J. Eur. Ceram. Soc. 38(9) (2018) 3201-3209.

[132] C.M. Lauener, L. Petho, M. Chen, Y. Xiao, J. Michler, J.M. Wheeler, Fracture of Silicon: Influence of rate, positioning accuracy, FIB machining, and elevated temperatures on toughness measured by pillar indentation splitting, Materials & Design 142 (2018) 340-349.

[133] J.P. Best, J. Zechner, J.M. Wheeler, R. Schoeppner, M. Morstein, J. Michler, Small-scale fracture toughness of ceramic thin films: the effects of specimen geometry, ion beam notching and high temperature on chromium nitride toughness evaluation, Philos. Mag. 96(32-34) (2016) 3552-3569.

[134] Y.-c. Wang, D.-g. Xie, X.-h. Ning, Z.-w. Shan, Thermal treatment-induced ductile-to-brittle transition of submicron-sized Si pillars fabricated by focused ion beam, Appl. Phys. Lett. 106(8) (2015) 081905.

[135] K. Kerman, A. Luntz, V. Viswanathan, Y.-M. Chiang, Z. Chen, Practical Challenges Hindering the Development of Solid State Li Ion Batteries, J. Electrochem. Soc. 164(7) (2017) A1731-A1744.

[136] P. Verma, P. Maire, P. Novák, A review of the features and analyses of the solid electrolyte interphase in Li-ion batteries, Electrochim. Acta 55(22) (2010) 6332-6341.

[137] P.G. Balakrishnan, R. Ramesh, T. Prem Kumar, Safety mechanisms in lithium-ion batteries, J. Power Sources 155(2) (2006) 401-414.

[138] A. Sakuda, A. Hayashi, M. Tatsumisago, Sulfide Solid Electrolyte with Favorable Mechanical Property for All-Solid-State Lithium Battery, Sci. Rep. 3 (2013) 2261.

[139] L. Porz, T. Swamy, B.W. Sheldon, D. Rettenwander, T. Frömling, H.L. Thaman, S. Berendts, R. Uecker, W.C. Carter, Y.-M. Chiang, Mechanism of Lithium Metal Penetration through Inorganic Solid Electrolytes, Advanced Energy Materials (2017) 1701003.

[140] R.D. Armstrong, T. Dickinson, J. Turner, The breakdown of β-alumina ceramic electrolyte, Electrochim. Acta 19(5) (1974) 187-192.

[141] R.R. H., T.G. J., A Model for Degradation of Ceramic Electrolytes in Na-S Batteries, J. Am. Ceram. Soc. 58(1-2) (1975) 63-67.

[142] R. Sudo, Y. Nakata, K. Ishiguro, M. Matsui, A. Hirano, Y. Takeda, O. Yamamoto, N. Imanishi, Interface behavior between garnet-type lithium-conducting solid electrolyte and lithium metal, Solid State Ionics 262 (2014) 151-154.

[143] Y. Ren, Y. Shen, Y. Lin, C.-W. Nan, Direct observation of lithium dendrites inside garnet-type lithium-ion solid electrolyte, Electrochem. Commun. 57 (2015) 27-30.

[144] C.L. Tsai, V. Roddatis, C.V. Chandran, Q. Ma, S. Uhlenbruck, M. Bram, P. Heitjans, O. Guillon, $Li_7La_3Zr_2O_{12}$ Interface Modification for Li Dendrite Prevention, ACS Appl Mater Interfaces 8(16) (2016) 10617-26.

[145] Y. Li, X. Chen, A. Dolocan, Z. Cui, S. Xin, L. Xue, H. Xu, K. Park, J.B. Goodenough, Garnet electrolyte with an ultra-low interfacial resistance for Li-metal batteries, J. Am. Chem. Soc. (2018).

[146] K. Fu, Y. Gong, B. Liu, Y. Zhu, S. Xu, Y. Yao, W. Luo, C. Wang, S.D. Lacey, J. Dai, Y. Chen, Y. Mo, E. Wachsman, L. Hu, Toward garnet electrolyte–based Li metal batteries: An

ultrathin, highly effective, artificial solid-state electrolyte/metallic Li interface, Science Advances 3(4) (2017).

[147] C. Monroe, J. Newman, Dendrite Growth in Lithium/Polymer Systems, J. Electrochem. Soc. 150(10) (2003) A1377.

[148] A.K. Pannikkat, R. Raj, Measurement of an electrical potential induced by normal stress applied to the interface of an ionic material at elevated temperatures, Acta Mater. 47(12) (1999) 3423-3431.

[149] R. Raj, J. Wolfenstine, Current limit diagrams for dendrite formation in solid-state electrolytes for Li-ion batteries, J. Power Sources 343 (2017) 119-126.

[150] X. Xiao, P. Liu, M.W. Verbrugge, H. Haftbaradaran, H. Gao, Improved cycling stability of silicon thin film electrodes through patterning for high energy density lithium batteries, J. Power Sources 196(3) (2011) 1409-1416.

[151] C. Wang, Y. Gong, B. Liu, K. Fu, Y. Yao, E. Hitz, Y. Li, J. Dai, S. Xu, W. Luo, E.D. Wachsman, L. Hu, Conformal, Nanoscale ZnO Surface Modification of Garnet-Based Solid-State Electrolyte for Lithium Metal Anodes, Nano Lett. 17(1) (2017) 565-571.

[152] A. Sharafi, E. Kazyak, A.L. Davis, S. Yu, T. Thompson, D.J. Siegel, N.P. Dasgupta, J. Sakamoto, Surface Chemistry Mechanism of Ultra-Low Interfacial Resistance in the Solid-State Electrolyte $Li_7La_3Zr_2O_{12}$, Chem. Mater. 29(18) (2017) 7961-7968.

[153] R.H. Basappa, T. Ito, H. Yamada, Contact between Garnet-Type Solid Electrolyte and Lithium Metal Anode: Influence on Charge Transfer Resistance and Short Circuit Prevention, J. Electrochem. Soc. 164(4) (2017) A666-A671.

[154] L. Cheng, E.J. Crumlin, W. Chen, R. Qiao, H. Hou, S. Franz Lux, V. Zorba, R. Russo, R. Kostecki, Z. Liu, K. Persson, W. Yang, J. Cabana, T. Richardson, G. Chen, M. Doeff, The origin of high electrolyte-electrode interfacial resistances in lithium cells containing garnet type solid electrolytes, PCCP 16(34) (2014) 18294-18300.

[155] A. Sharafi, S. Yu, M. Naguib, M. Lee, C. Ma, H.M. Meyer, J. Nanda, M. Chi, D.J. Siegel, J. Sakamoto, Impact of air exposure and surface chemistry on Li–$Li_7La_3Zr_2O_{12}$ interfacial resistance, J. Mater. Chem. A 5(26) (2017) 13475-13487.

[156] Y. Kim, H. Jo, J.L. Allen, H. Choe, J. Wolfenstine, J. Sakamoto, G. Pharr, The Effect of Relative Density on the Mechanical Properties of Hot-Pressed Cubic $Li_7La_3Zr_2O_{12}$, J. Am. Ceram. Soc. 99(4) (2016) 1367-1374.

[157] A. Sharafi, C.G. Haslam, R.D. Kerns, J. Wolfenstine, J. Sakamoto, Controlling and correlating the effect of grain size with the mechanical and electrochemical properties of $Li_7La_3Zr_2O_{12}$ solid-state electrolyte, J Mater Chem A 5(40) (2017) 21491-21504.

[158] W. Xia, B. Xu, H. Duan, X. Tang, Y. Guo, H. Kang, H. Li, H. Liu, Reaction mechanisms of lithium garnet pellets in ambient air: The effect of humidity and CO2, J. Am. Ceram. Soc. (2017).

[159] A. Orera, G. Larraz, J.A. Rodriguez-Velamazan, J. Campo, M.L. Sanjuan, Influence of Li^+ and H^+ Distribution on the Crystal Structure of $Li_{(7-x)}H_{(x)}La_3Zr_2O_{12}$ ($0 \leq x \leq 5$) Garnets, Inorg. Chem. 55(3) (2016) 1324-32.

[160] B. Merle, V. Maier-Kiener, G.M. Pharr, Influence of modulus-to-hardness ratio and harmonic parameters on continuous stiffness measurement during nanoindentation, Acta Mater. 134(Supplement C) (2017) 167-176.

[161] A. Leitner, V. Maier-Kiener, D. Kiener, Dynamic nanoindentation testing: is there an influence on a material's hardness?, Materials Research Letters 5(7) (2017) 486-493.

[162] J.F. Nonemacher, C. Hüter, H. Zheng, J. Malzbender, M. Krüger, R. Spatschek, M. Finsterbusch, Microstructure and properties investigation of garnet structured $Li_7La_3Zr_2O_{12}$ as electrolyte for all-solid-state batteries, Solid State Ionics 321 (2018) 126-134.

[163] H. Buschmann, S. Berendts, B. Mogwitz, J. Janek, Lithium metal electrode kinetics and ionic conductivity of the solid lithium ion conductors "$Li_7La_3Zr_2O_{12}$" and $Li_{7-x}La_3Zr_{2-x}Ta_xO_{12}$ with garnet-type structure, Journal of Power Sources 206 (2012) 236-244.

[164] C.L. Tsai, E. Dashjav, E.M. Hammer, M. Finsterbusch, F. Tietz, S. Uhlenbruck, H.P. Buchkremer, High conductivity of mixed phase Al-substituted $Li_7La_3Zr_2O_{12}$, J Electroceramics 35(1-4) (2015) 25-32.

[165] M. Kotobuki, K. Kanamura, Y. Sato, K. Yamamoto, T. Yoshida, Electrochemical properties of $Li_7La_3Zr_2O_{12}$ solid electrolyte prepared in argon atmosphere, J Power Sources 199 (2012) 346-349.

[166] C.A. Geiger, E. Alekseev, B. Lazic, M. Fisch, T. Armbruster, R. Langner, M. Fechtelkord, N. Kim, T. Pettke, W. Weppner, Crystal chemistry and stability of " $Li_7La_3Zr_2O_{12}$" garnet: a fast lithium-ion conductor, Inorganic chemistry 50(3) (2011) 1089-97.

[167] M.W. Barsoum, FUNDAMENTALS OF CERAMICS, CRC Press 2002.

[168] C.-L. Tsai, E. Dashjav, E.-M. Hammer, M. Finsterbusch, F. Tietz, S. Uhlenbruck, H.P. Buchkremer, High conductivity of mixed phase Al-substituted $Li_7La_3Zr_2O_{12}$ J. Electroceram. 35(1-4) (2015) 25-32.

[169] Y. Shimonishi, A. Toda, T. Zhang, A. Hirano, N. Imanishi, O. Yamamoto, Y. Takeda, Synthesis of garnet-type $Li_{7-x}La_3Zr_2O_{12-1/2x}$ and its stability in aqueous solutions, Solid State Ionics 183(1) (2011) 48-53.

[170] D.O. Shin, K. Oh, K.M. Kim, K.Y. Park, B. Lee, Y.G. Lee, K. Kang, Synergistic multi-doping effects on the $Li_7La_3Zr_2O_{12}$ solid electrolyte for fast lithium ion conduction, Sci. Rep. 5 (2015) 18053.

[171] T. Thompson, J. Wolfenstine, J.L. Allen, M. Johannes, A. Huq, I.N. David, J. Sakamoto, Tetragonal vs. cubic phase stability in Al – free Ta doped $Li_7La_3Zr_2O_{12}$ (LLZO), J. Mater. Chem. A 2(33) (2014) 13431-13436.

[172] J. Wolfenstine, E. Rangasamy, J.L. Allen, J. Sakamoto, High conductivity of dense tetragonal $Li_7La_3Zr_2O_{12}$, J. Power Sources 208 (2012) 193-196.

[173] K. Meier, T. Laino, A. Curioni, Solid-State Electrolytes: Revealing the Mechanisms of Li-Ion Conduction in Tetragonal and Cubic LLZO by First-Principles Calculations, The Journal of Physical Chemistry C 118(13) (2014) 6668-6679.

[174] P.J. Kumar, K. Nishimura, M. Senna, A. Düvel, P. Heitjans, T. Kawaguchi, N. Sakamoto, N. Wakiya, H. Suzuki, A novel low-temperature solid-state route for nanostructured cubic garnet $Li_7La_3Zr_2O_{12}$ and its application to Li-ion battery, RSC Adv. 6(67) (2016) 62656-62667.

[175] I. Manika, J. Maniks, Size effects in micro- and nanoscale indentation, Acta Mater. 54(8) (2006) 2049-2056.

[176] S.J. Bull, T.F. Page, E.H. Yoffe, An explanation of the indentation size effect in ceramics, Philos. Mag. Lett. 59(6) (1989) 281-288.

[177] J. Malzbender, R.W. Steinbrech, Determination of the stress-dependent stiffness of plasma-sprayed thermal barrier coatings using depth-sensitive indentation, J. Mater. Res. 18(8) (2011) 1975-1984.

[178] N.N. Bramnik, K. Nikolowski, D.M. Trots, H. Ehrenberg, Electrochem. Solid-State Lett. 11(null) (2008) A89.

[179] D. Di Maio, S.G. Roberts, Measuring fracture toughness of coatings using focused-ion-beam-machined microbeams, J. Mater. Res. 20(02) (2011) 299-302.

[180] G. Žagar, V. Pejchal, M.G. Mueller, L. Michelet, A. Mortensen, Fracture toughness measurement in fused quartz using triangular chevron-notched micro-cantilevers, Scripta Mater. 112 (2016) 132-135.

[181] B.N. Jaya, S. Bhowmick, S.A.S. Asif, O.L. Warren, V. Jayaram, Optimization of clamped beam geometry for fracture toughness testing of micron-scale samples, Philos. Mag. 95(16-18) (2015) 1945-1966.

[182] L. Robben, E. Merzlyakova, P. Heitjans, T.M. Gesing, Symmetry reduction due to gallium substitution in the garnet $Li_{6.43(2)}Ga_{0.52(3)}La_{2.67(4)}Zr_2O_{12}$, Acta Crys Section E Crystallographic Communications 72(3) (2016) 287-289.

[183] R.W. Rice, S.W. Freiman, P.F. Becher, Grain-Size Dependence of Fracture Energy in Ceramics: I, Experiment, J. Am. Ceram. Soc. 64(6) (1981) 345-350.

[184] R. Rice, Grain size and porosity dependence of ceramic fracture energy and toughness at 22 C, J Mater Sci 31(8) (1996) 1969-1983.

Appendix

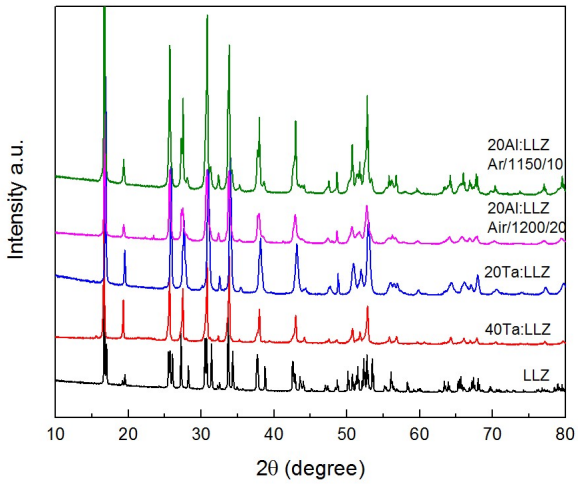

Figure A.1- XRD patterns of pure LLZ, Al and Ta dopants.

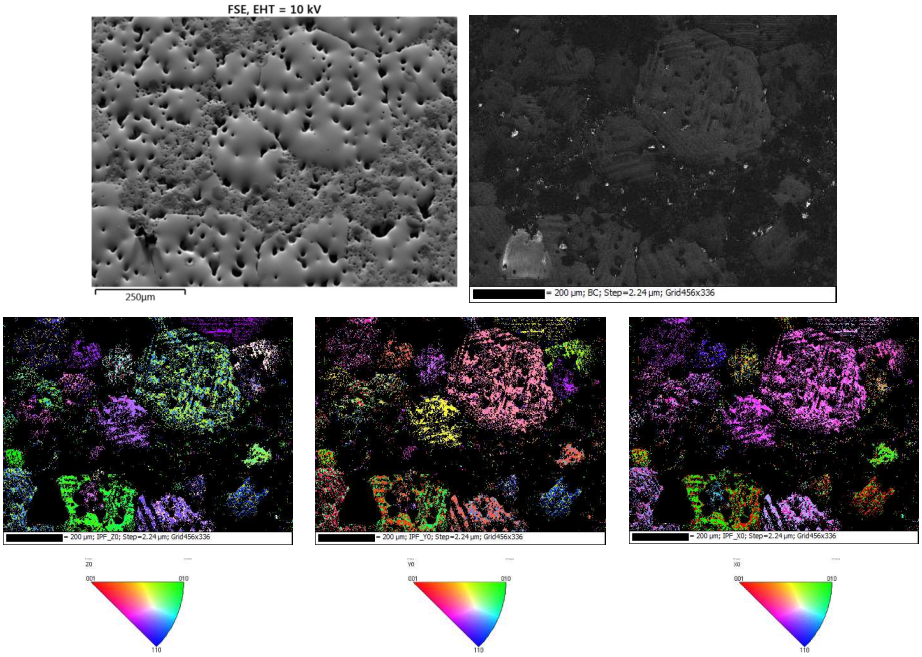

a) b) c)

Figure A.2- EBSD orientation map of 20Al:LLZO-2h a) Z - direction (sample normal direction), b) Y - direction; c) X-direction.

a)

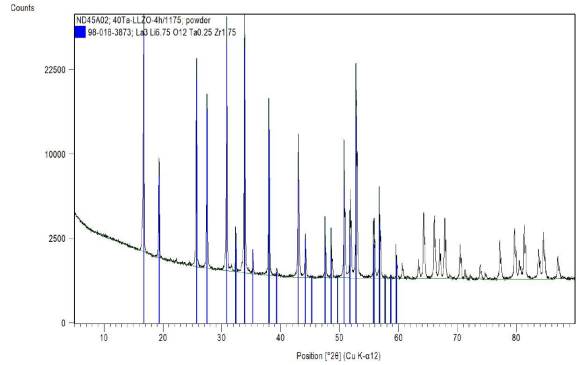

b)

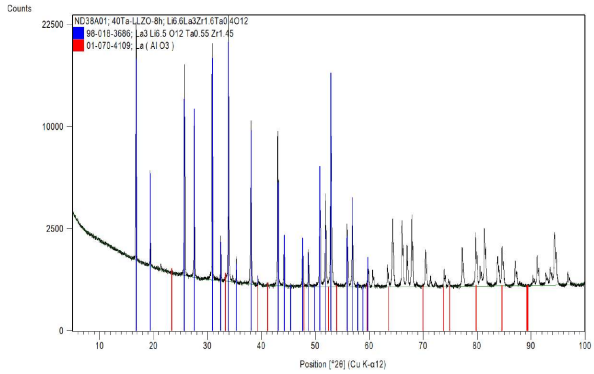

Figure A.3- XRD patterns a) 40Ta:LLZO-4h b) 40Ta:LLZO-8h.

Publications & Conferences

J. F. Nonemacher, J. Malzbender, Micro-mechanical characterization of solid state electrolytes using indentation testing (Poster). Junior Euromat, Lausanne, Switzerland, 2016.

J. F. Nonemacher, C-L.Tsai, S. Uhlenbruck J. Malzbender, Mechanical characterization of Ta-substituted $Li_7La_3Zr_2O_{12}$ using nano- and micro-indentation (Poster). 15th Conference and Exhibition of the European Ceramic Society, Budapest, Hungary, 2017.

J. F. Nonemacher, M. Finsterbusch, J. Malzbender Micro-mechanical characterization of $Li_7La_3Zr_2O_{12}$ for solid state batteries (Oral presentation). 42nd International Conference on Advanced Ceramics and Composites, Daytona Beach, USA, 2018.

A. Wang, **J. F. Nonemacher**, G.Yan, M. Finsterbusch, J. Malzbender, M. Krüger, Mechanical properties of the solid electrolyte Al-substituted $Li_7La_3Zr_2O_{12}$ (LLZO) by utilizing micro-pillar indentation splitting test, Journal of European Ceramic Society 38 (2018) 3201-3209.

J. F. Nonemacher, C. Hüter, H. Zheng, J. Malzbender, M. Krüger, R. Spatschek, M. Finsterbusch, Microstructure and properties investigation of garnet structured $Li_7La_3Zr_2O_{12}$ as electrolyte for all-solid-state batteries, Solid State Ionics 321 (2018) 126-134.

G. Yan, **J. F. Nonemacher,** H. Zheng, M. Finsterbusch, J. Malzbender, M. Krüger, An investigation on strength distribution, subcritical crack growth and lifetime of the lithium-ion conductor $Li_7La_3Zr_2O_{12}$. Journal of Materials Science (2019) 54:5671.

J. F. Nonemacher, G. Yang, C.-L. Tsai, S. Uhlenbruck, M. Finsterbusch, J. Malzbender, M. Krüger, Measuring the fracture toughness of solid electrolytes for batteries using micro-pillar indentation splitting test. Indentation Conference, Liège, Belgium, 2018.

G. Yang, S. Yu, **J. F. Nonemacher**, H. Tempel, H. Kungl, J. Malzbender, R.-A. Eichel, M. Krüger, Influence of Influence of sintering temperature on conductivity and mechanical behavior of the solid electrolyte LATP, Ceramics International, Vol 45 Issue 12 (2019) 14697-14703.

J. F. Nonemacher, S. Naqash, F. Tietz, J. Malzbender, Micromechanical assessment of Al/Y-substituted NASICON solid electrolytes, Ceramics International, Vol 45 Issue 17 Part A (2019) 21308-21314.

Acknowledgements

A doctoral thesis can be a lonely journey and a truly life-changing experience and at this point, it is a great pleasure for me to have so many people who kept me company over these intense three years. Therefore, I would like to express my gratitude to everyone who have supported me or contributed to the completion of this work.

Firstly, I want to appreciate the National Council for Scientific and Technological Development - CNPq, Brazil and the German Academic Exchange Service (DAAD) for the financial support and for giving me the opportunity to pursue my doctoral degree in Germany.

My sincere thanks to my head of Institute Prof. Dr. Lorenz Singheiser who was also partially my doctoral supervisor for giving me the opportunity to apply for the doctor degree in Forschungszentrum Jülich, also for Prof. Dr. Robert Spatschek and Prof. Dr. Ing.- Manja Krüger for supervising and all the scientific support of my work over the years and ensuring that I met the requirements for obtaining the Doctor of Engineering.

Special thanks, to my scientific supervisor Dr. Jürgen Malzbender for his dedication and support. I appreciate the guidance and sharing of scientific skills. My sincere thanks to Dr. An-Ni Wang for her short but intense collaboration, insightful comments and encouragement.

Furthermore, I thank Univ.-Prof. Dr.-Ing. Ulrich Krupp for accepting to be my second examiner and for his timely correction of this work and Univ.-Prof. Dr. Sandra Korte-Kerzel for accepting the chairmanship of the Examination Committee.

Many thanks to IEK-2 team, Dr. Egbert Wessel, Mirko Ziegner, Mrs. Daniela Eßer, Marita Offerman, Katrin Leipertz, Jörg Bartsch, Volker Gutzeit, Marcel Turiaux and specially Tatjana Osipova for technical support and the contribution towards the successful completion of this work.

I also thank the colleagues from IEK-1 Dr. Sven Uhlenbruck for all the support, Dr. Chih-Long Tsai, Dr. Martin Finsterbusch, Dr. Qianli Ma, Dr. Yulia Arinicheva, Dr. Frank Tietz, Dr. Sahir Naqash for the working collaboration and providing samples for my work.

I want to thank my friends and office mates Dr. Rafael Silva, Gang Yan, Dr. Jianping Wei, Sebastian von Helden, Dr. Vahid Ebrahimzade, Fanlin Zeng and others for the stimulating discussions, for all the fun and pleasant working atmosphere. So many other friends I made on the journey, Dr. Unoaku Unije, Samia Dolmans-Nadi, Jeerawan Brent, Florisa Martins, Douglas Weber, Eugen Kaganovich and so many others. Thank you all.

I would also like to say a heartfelt thank you to all my friends from DAAD - Tayana, Ligia, Analice, Bernardo, Pastl, Pacheco, Thamires, Moussalem, Gustavo. Muito obrigada.

Very special thanks to my family, specially my parents Benvinda Nonemacher and José Romildo Nonemacher for their warm love, guidance, endless support and for always respecting my decisions. I would not be who I am and where I am, without you.

Band / Volume 476
Partitioning of carbon dioxide exchange in rapidly and slowly changing ecosystems
P. Ney (2019), xvi, 95 pp
ISBN: 978-3-95806-431-7

Band / Volume 477
Massentransportphänomene in Schichtsystemen eines Elektrolyseurs
U. Panchenko (2019), 107 pp
ISBN: 978-3-95806-433-1

Band / Volume 478
Mechanische Eigenschaften von Polymer-Elektrolyt-Membran-Brennstoffzellen
P. Irmscher (2019), vii, 177 pp
ISBN: 978-3-95806-435-5

Band / Volume 479
Morphology and Degradation of High Temperature Polymer Electrolyte Fuel Cell Electrodes
S. Liu (2019), III, 162 pp
ISBN: 978-3-95806-436-2

Band / Volume 480
Structural uptake and retention of safety relevant radionuclides by cementitious materials
S. Lange (2019), 133 pp
ISBN: 978-3-95806-437-9

Band / Volume 481
Quantifying the Impact of Inhomogeneity, Transport and Recombination in Emerging Thin-Film Solar Cells
P. Kaienburg (2019), vii, 258 pp
ISBN: 978-3-95806-440-9

Band / Volume 482
Studies of oxidation resistant tungsten alloys at temperatures of 1100K to 1475K
F. Klein (2019), 158 pp
ISBN: 978-3-95806-444-7

Band / Volume 483
Impact Assessment of Land-Use Change and Agricultural Treatments on Greenhouse Gas Emissions from Wetlands of Uganda and Tanzania
K. X. X. Wagner (2019), 144 pp
ISBN: 978-3-95806-447-8

Band / Volume 484
IEK-3 Report 2019
Tailor-Made Energy Conversion for Sustainable Fuels
D. Stolten, B. Emonts (Eds.) (2020), 162 pp
ISBN: 978-3-95806-451-5

Band / Volume 485
Multiskalare Modellierung integrierter Energie- und Elektrizitätssysteme
T. C. Pesch (2019), XXV, 384 pp
ISBN: 978-3-95806-452-2

Band / Volume 486
Quantitative Untersuchung des Laserablationsprozesses mittels Kombination von optischer Spektroskopie und Massenspektrometrie
J. Oelmann (2020), vii, 141 pp
ISBN: 978-3-95806-453-9

Band / Volume 487
Leistungssteigerung metallgestützter Festelektrolyt-Brennstoffzellen (MSCs) durch gezielte Optimierungen des Anoden/Elektrolytverbunds
C. Bischof (2020), X, 176 pp
ISBN: 978-3-95806-455-3

Band / Volume 488
Aluminiumoxiddispersionsverstärkte Haftvermittlermaterialien in Wärmedämmschichtsystemen
C. Vorkötter (2020), VIII, 99, XXXIII pp
ISBN: 978-3-95806-457-7

Band / Volume 489
The Balmer lines emission of fast hydrogen atoms at the plasma-solid interface in a low density plasma: challenges and applications
S. O. Dickheuer (2020), 117 pp
ISBN: 978-3-95806-458-4

Band / Volume 490
Micromechanical Characterization of Ceramic Solid Electrolytes for Electrochemical Storage Devices
J. F. Nonemacher (2020), xv, 131 pp
ISBN: 978-3-95806-461-4

Weitere ***Schriften des Verlags im Forschungszentrum Jülich*** unter
http://wwwzb1.fz-juelich.de/verlagextern1/index.asp

Energie & Umwelt / Energy & Environment
Band / Volume 490
ISBN 978-3-95806-461-4

Mitglied der Helmholtz-Gemeinschaft

JÜLICH
Forschungszentrum